

# A 10 mK Scanning Probe Microscopy Facility

Young Jae Song,<sup>1,2</sup> Alexander F. Otte,<sup>1,2</sup> Vladimir Shvarts,<sup>3</sup> Zuyu Zhao,<sup>3</sup> Young Kuk,<sup>4</sup> Steven R. Blankenship,<sup>1</sup> Alan Band,<sup>1</sup> Frank M. Hess,<sup>1</sup> and Joseph A. Stroscio\*<sup>1</sup>

<sup>1</sup>Center for Nanoscale Science and Technology, NIST, Gaithersburg, MD 20899

<sup>2</sup>Maryland NanoCenter, University of Maryland, College Park, Maryland 20742

<sup>3</sup>Janis Research Company Inc., Wilmington, MA 01887

<sup>4</sup>Department of Physics, Seoul National University, Seoul, South Korea

(Dated: 29 October 2010)

We describe the design, development and performance of a scanning probe microscopy (SPM) facility operating at a base temperature of 10 mK in magnetic fields up to 15 T. The microscope is cooled by a custom designed, fully ultra-high vacuum (UHV) compatible dilution refrigerator (DR) and is capable of *in-situ* tip and sample exchange. Sub-picometer stability at the tip-sample junction is achieved through three independent vibration isolation stages and careful design of the dilution refrigerator. The system can be connected to, or disconnected from, a network of interconnected auxiliary UHV chambers, which include growth chambers for metal and semiconductor samples, a field ion microscope for tip characterization, and a fully independent additional quick access low temperature STM/AFM system. To characterize the system, we present the cooling performance of the DR, vibrational, tunneling current, and tip-sample displacement noise measurements. In addition, we show the spectral resolution capabilities with tunneling spectroscopy results obtained on an epitaxial graphene sample resolving the quantum Landau levels in a magnetic field, including the sub-levels corresponding to the lifting of the electron spin and valley degeneracies.

## CONTENTS

<b>I. Introduction</b>	2	<b>V. Vibration Isolation</b>	24
A. Brief History of SPM Instrumentation	2	A. Overview	24
<b>II. NIST Ultra-Low Temperature SPM Facility</b>	4	B. Vibration Isolation in the NIST ULTSPM system	24
A. Overview	4	C. Vibration Isolation System Performance	26
B. The Processing Lab	4	<b>VI. Electronics</b>	27
1. MBE Growth Systems	4	A. Overview	27
2. RF Induction Furnace	4	B. Control Electronics	29
3. Field-Ion Microscopy System	5	C. Cabling and Cryogenic Preamplifier	30
4. Quick Access Low Temperature SPM System	6	<b>VII. Performance</b>	31
5. Two-stage Load Lock System	6	A. Overview	31
C. Tip and Sample Transport through the UHV Systems	6	B. Effects of Piezo Walker Motion and Magnetic Field Ramps	32
D. Cryostat Assembly and transfer of Tip, Sample, and SPM Module	8	C. Amplifier Noise Measurements	32
<b>III. SPM Module</b>	9	D. Tunneling Noise Measurements: Comparing the Joule-Thomson and 1 K pot Condensing Modes	33
A. Overview	9	E. STM and STS Measurements	34
B. SPM Module for mK Applications	10	1. Cu <sub>2</sub> N on Cu(100)	34
<b>IV. A Dilution Refrigerator for SPM</b>	13	2. Epitaxial Graphene	35
A. Cryogenic Techniques for $T < 4$ K	13	<b>VIII. Summary</b>	37
B. DR System Overview	16	<b>IX. References</b>	37
C. Helium Cryostat	16	<b>Acknowledgments</b>	39
D. UHV Compatible DR Insert	17		
E. SPM Module Transfer and Radiation Shielding	18		
F. Temperature Measurement	19		
G. DR Performance	20		
1. Cooling Power Measurements	20		
2. Vibration Measurements	23		

---

\*To whom correspondence should be addressed: joseph.stroscio@nist.gov (J.A.S)

## I. INTRODUCTION

Since the beginning of the last century new frontiers in physics have emerged when advances in instrumentation achieved lower experimental operating temperatures,  $T$ . Notable examples include the discovery of superconductivity,<sup>1</sup> the integer quantum Hall effect,<sup>2</sup> and fractional quantum Hall effect.<sup>3</sup> The ongoing improvement of cryogenic instrumentation has produced a range of quite remarkable equipment for both fundamental and applied research. This process is driven by the notion that what is seen today as ‘up-to-date cryogenic techniques’ needs to be continuously modified or adapted in order to meet the needs of new experimental challenges.

A case in point is scanning probe microscopy, which has seen a wealth of new measurements emerge as cryogenic SPM instruments have been developed in the last two decades<sup>4–42</sup> allowing detailed spectroscopic studies with atomic spatial resolution and often under applied magnetic field,  $B$ . Most of these instruments<sup>5–18</sup> operate near liquid helium temperatures (4.2 K) with some <sup>3</sup>He instruments attaining temperatures of 300 mK to 500 mK.<sup>19–31</sup> Very recently a number of instruments have reached tens of mK operating temperatures.<sup>24,32–42</sup> While mK-scale operation has been demonstrated for these SPM instruments, routine operation for high resolution tunneling spectroscopy is rare. Sorely needed are instruments that are ultra-high vacuum (UHV) compatible with ultra-low base temperature, highest possible  $B/T$  ratios, and special features to reduce external and intrinsic vibrations to the levels demanded by atomic level SPM resolution.

In this article we present an extensive description of the development of an UHV SPM system that achieves a base operating temperature of 10 mK with a high magnetic field capability of 15 T, while achieving a high signal-to-noise ratio and maintaining atomic resolution in both topographic and spectroscopic modes. This article is written to give the reader sufficient detail to understand the various elements of cryogenics, vibration isolation, SPM instrumentation, and electronics needed to achieve this level of performance. The article is divided into 8 sections. The first section describes a brief history of SPM instrumentation. Section II gives an overview of the NIST facility and the functionality of the various component systems. Section III describes the SPM module, compatible with mK temperatures and high magnetic fields. Section IV introduces cryogenic cooling techniques, and describes a custom designed low-noise UHV compatible dilution refrigerator that is used for cooling the SPM instrument to 10 mK. Section V describes the design of a three-stage vibration isolation system, including the NIST A-1 inertial mass concept used in the NIST Advanced Measurement Laboratory (AML).<sup>43</sup> The electronics in this system are described in section VI. Finally, the performance of the instrument is detailed in section VII, and we present a brief summary and future outlook in section VIII.

Certain commercial equipments, instruments, or materials are identified in this paper in order to specify the experimental procedure adequately. Such identification is not intended to imply recommendation or endorsement by the National Institute of Standards and Technology, nor is it intended to imply that the materials or equipment identified are necessarily the best available for the purpose.

### A. Brief History of SPM Instrumentation

A scanning probe microscope in its simplest form uses a fine probe tip in close proximity to a sample surface to measure a particular physical property. SPMs achieve atomic or nanometer scale resolution using probe tips which have dimensions in this range, and typically measure physical properties by scanning the sample with tip-sample separations of one to a few nanometers using piezoelectric actuators. The advent of scanning probe microscopy led to the birth of the current nanoscale science and technology disciplines, which focus on measurements in physics and materials science at nanometer length scales. Along its development path SPM greatly impacted many fields of science, such as surface science, materials science, tribology, biology, semiconductor metrology, superconductivity, and physics of low dimensional systems, to name a few. Surface science was one of the fields first impacted by SPM. Until the celebrated 1981 IBM Zurich invention by Binnig and Rohrer of the scanning tunneling microscope (STM),<sup>44–47</sup> researchers relied on surface analysis techniques that displayed the atomic structure of a surface mainly in momentum space. An exception to this is field-ion-microscopy (FIM),<sup>48–50</sup> which can image atoms at the end of a sharp tip, but is limited in its application. STM enabled, for the first time, direct observation of atomic-scale surface phenomena of any conducting surface in real space. In addition, with the advent of atomic force microscopy (AFM) in 1986, insulating surfaces can be probed on the atomic scale as well. These discoveries triggered the development of a wide range of imaging techniques each relying on a local scanning probe that measures some physical property. These became known collectively as Scanning Probe Microscopy. Examples of SPM are atomic force microscopy (AFM), electrostatic force microscopy (EFM), near-field scanning optical microscopy (NSOM), scanning capacitance microscopy (SCM), scanning gate microscopy (SGM), and many others.<sup>51–58</sup>

The invention of the STM was preceded by the independent development of the ‘Topografiner’ by R. Young at the National Bureau of Standards (NBS, now the National Institute of Standards and Technology, or NIST).<sup>59</sup> In the topografiner, a tip was held at a constant distance from a sample surface by piezoelectric elements using the field-emission current from the probe tip for feedback control. The topografiner achieved a lateral (i.e. in the plane of the surface) resolution of 400 nm and a

vertical resolution of 3 nm. The STM differed from this concept only in that it used the quantum mechanical tunnel current rather than the field-emission current for its feedback. The ability to use tunnel current feedback was enabled by the implementation of better vibration isolation designs. A measurable tunnel current between a tip and sample electrode occurs at a much smaller tip-sample separation and depends exponentially on the tip-sample distance, giving the STM its spectacular, truly atomic resolution, both laterally and vertically.

Shortly after the STMs successful debut, efforts in the development of STM's operating at cryogenic temperatures were initiated, mostly driven by the interest in applications to superconductivity. The first low temperature STM ( $\approx 18$  K) measured the spatial variation of superconductivity on  $\text{Nb}_3\text{Sn}$ .<sup>60</sup> The ability to locally study the physics of superconductivity by STM has greatly helped the understanding of superconductors and it remains a central investigative technique in the field to this day.<sup>61</sup>

The problems associated with STMs operating at cryogenic temperatures were associated with piezoelectric positioning systems failing to work when cooled to low temperatures, and difficulty in combining vibration isolation techniques with cryogenics and vacuum requirements. Learning from the problems in early attempts to construct cryogenic STMs, a number of laboratories were successful in the development of 4 K STMs from the 1990s using different designs that incorporate exchange gas decoupling,<sup>7-9,11-13,16,17,62</sup> flow through designs,<sup>14</sup> and bottom loading cryostats in UHV.<sup>10,15</sup> The stability of these low temperature systems ushered in new experiments for the study of single atoms with unprecedented precision and delivered a range of new results; for example, in atomic manipulation,<sup>7,63</sup> single atom vibrational and spin excitation spectroscopy,<sup>64,65</sup> spin polarized tunneling,<sup>66</sup> and 2-dimensional electron systems.<sup>26,67-69</sup>

The development of instruments operating below 4 K was more challenging, with early instruments based initially on very specific designs. Although there were a few of attempts at below 4 K operation in the late 1980s, early 1990s, using  $^3\text{He}$ ,<sup>19,20</sup> and dilution refrigerator systems,<sup>32</sup> successfully operating systems were not developed until late 1990s and thereafter using  $^3\text{He}$  systems.<sup>21-25</sup> Initial attempts at using dilution refrigerator technology were fraught with technical barriers largely due to significant vibrations coming from the refrigerator itself. A number of groups have succeeded in adapting dilution refrigerator technology to AFM instruments starting in 1999,<sup>33</sup> and continuing to the present.<sup>36,38,39</sup> The application of dilution refrigerator technology to STM measurements is limited to a few groups,<sup>24,32,34,35,40</sup> presumably due to the greater stability demands at the smaller tip-sample separations in STM compared to AFM, and routine operation of instruments at temperatures of tens of mK has remained challenging.

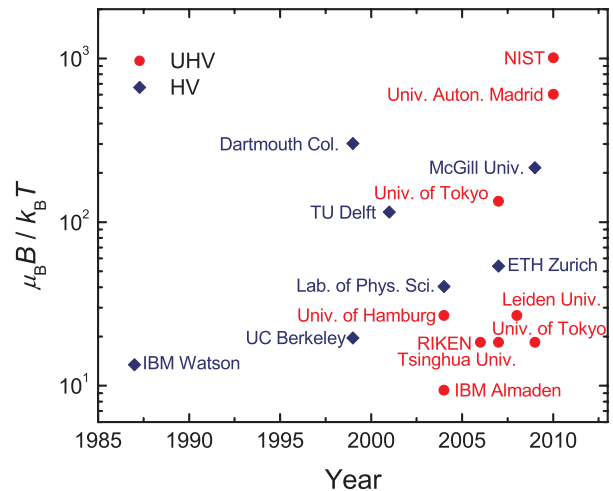


FIG. 1. Plot of the figure of merit for cryogenic SPM systems,  $\mu_B B / k_B T$ , vs. year. Various sub-K SPM systems reported over the last 30 years are listed along with their locations. Red dots refer to UHV compatible systems, while systems represented by blue dots have low vacuum (often cryo-vacuum) only. References: IBM Watson, 1987<sup>19</sup>; UC Berkeley, 1999<sup>21</sup>; Dartmouth College, 1999<sup>33</sup>; TU Delft, 2001<sup>35</sup>; IBM Almaden, 2004<sup>65</sup>; Universitat Hamburg, 2004<sup>25</sup>; Laboratory for Physical Sciences, 2004<sup>38</sup>; RIKEN, 2006<sup>27</sup>; ETH Zurich, 2007<sup>39</sup>; University of Tokyo, 2007<sup>40</sup>; Tsinghua University, 2007<sup>28</sup>; Leiden University, 2008<sup>30</sup>; McGill University, 2008<sup>41</sup>; University of Tokyo, 2009<sup>31</sup>; Universidad Autónoma de Madrid, 2010<sup>42</sup>. The dot labeled NIST refers to the system described in this paper.

In scanning tunneling spectroscopy (STS) measurements, the measured differential conductance,  $dI/dV$ , is proportional to the sample density of states, and is widely used in spectroscopic mapping studies with the great success in many applications.<sup>51,55,56</sup> The main driving factor for the development of low temperature STMs, besides increased stability, was the need for higher energy resolution in STS measurements. By reducing the width of the Fermi-Dirac distribution of the electrons in the tip, there is less variation in the energies of electrons tunneling into the sample at a certain value of the bias voltage. At a temperature  $T$ , the energy resolution  $\Delta E$  of a tunneling spectroscopy measurement using a lock-in technique with a modulation voltage of  $V_{mod}$  can be expressed approximately as,<sup>70</sup>

$$\Delta E \simeq \sqrt{(3.3k_B T)^2 + (2.5eV_{mod})^2}, \quad (1)$$

where  $k_B$  is Boltzmann's constant and  $e$  the elementary charge. Assuming the contribution from the modulation voltage is adjusted to be negligible, an energy resolution of about 85 meV is obtained at room temperature. At 4.2 K, the temperature of liquid helium, this is reduced to 1.2 meV, and if one were to lower the temperature to 10 mK (which is the base temperature of the system described in this paper) the energy resolution

could be made as low as  $3 \mu\text{eV}$ . Improving the energy resolution enables fine structure in the density of states to be clearly resolved, such as quantum states relating to single electron spins.<sup>65,69</sup> The advent of high resolution tunneling spectroscopy by cryogenic instrumentation has impacted many fields and created new spectroscopic techniques in areas such as superconductivity,<sup>61</sup> quantum Hall physics,<sup>67</sup> spin-polarized spectroscopy,<sup>66</sup> vibrational spectroscopy,<sup>64</sup> and spin-excitation spectroscopy.<sup>65</sup>

In the application of tunneling spectroscopy to electron spin phenomena, not only the temperature but also the magnitude of an externally applied magnetic field  $B$  plays an important role. In general, for studying magnetic properties the dimensionless quantity  $\mu_B B/k_B T$ , with  $\mu_B$  being the Bohr magneton, is a good measure of an STM instrument's spectral capabilities, as the Zeeman energy,  $\mu_B B$ , sets the energy scale to be resolved at the temperature  $T$ . Figure 1 shows values for the figure of merit,  $\mu_B B/k_B T$ , for various sub-one-Kelvin SPM systems reported over the last 25 years, classified by vacuum compatibility. Notice that even though the STM was invented in 1981, it took nearly two decades to achieve good working instruments with high resolving power. This time lag is due to the difficulty in combining the extreme environments of UHV, cryogenics, and high magnetic fields, with the stability needed for SPM measurements. The data point near the top right, labeled 'NIST', represents the system described in this paper and offers the highest resolving power to date.

## II. NIST ULTRA-LOW TEMPERATURE SPM FACILITY

### A. Overview

Here we describe the major components of an Ultra-Low Temperature SPM (ULTSPM) facility that has recently been completed at NIST. The system attains a base temperature of 10 mK with magnetic fields up to 15 T, and is designed for achieving  $\approx 100$  fm stability for microscopy and  $\approx 10 \mu\text{eV}$  energy resolution for spectroscopy measurements. All components are compatible with UHV conditions for ultra-clean *in-situ* tip/sample preparation, transfer and exchange.

The facility is located in an underground building that is part of the Advanced Measurement Laboratory at NIST.<sup>43</sup> It spans three adjacent rooms: a control room, a shielded measurement laboratory containing the ULTSPM instrument and UHV chamber, and a processing laboratory for tip and sample preparation. The ULTSPM lab is shielded by two acoustic enclosures with the inner enclosure also acting as an electrical shield against electronic radio-frequency (RF) interference. The inner shielded room is situated on an isolated concrete slab (inertial mass) with active vibration isolation, which is one of three vibration reduction stages (see Section V). The cryostat is suspended in a 3 m deep hole in the inertial mass.

Above the cryostat is mounted a UHV chamber into which the SPM module can be lifted from the bottom of the cryostat for tip- and sample-exchange. Tips and samples, prepared and characterized in the processing lab, are transferred under UHV to the ULTSPM lab through a DN 203 (8 inch outside diameter (OD)) UHV transfer line; referred to as the 'interlab' transfer line. One section of this transfer line is removable and portable so that the UHV chamber in the ULTSPM lab can be disconnected from the UHV chambers in the processing lab prior to starting SPM measurements.

### B. The Processing Lab

The SPM facility can be used for studying a wide variety of physical systems. In the processing lab, shown in Fig. 2, various growth and preparation chambers branch off from the interlab central vacuum line. Each chamber, equipped with a turbomolecular, ion, and titanium sublimation pump, can be valved off from the interlab central vacuum line and operated as a stand-alone vacuum system. This is different from most other SPM systems, where the preparation chambers are often an integral part of the SPM measurement system and cannot be used while the microscope is in operation. All chambers, including the interlab central vacuum line, can also be baked independently. For this purpose we use custom designed flexible bakeout blankets that attach together with Velcro fasteners.<sup>71</sup> The various UHV systems and their capabilities are described below.

#### 1. MBE Growth Systems

Two custom designed MBE chambers enable preparation and analysis of crystalline surfaces: one for metal samples ((1) in Fig. 2) and the other for III-V semiconductor samples ((2) in Fig. 2). Both chambers are equipped with sample heating stages, up to six evaporators, a flux monitor, and reflection-high-energy-electron diffraction (RHEED) surface analysis capabilities. In addition, the metal MBE chamber has a differentially pumped ion gun and an cylindrical-mirror-analyzer electron spectrometer used for Auger spectroscopy. The metal MBE chamber can be used to process most metal systems usually studied by SPM. The metal MBE chamber is configured to grow BiSe topological insulator materials and the semiconductor MBE chamber is configured to grow GaAs, GaAlAs, and InAs samples.

#### 2. RF Induction Furnace

The RF induction furnace ((3) in Fig. 2) allows samples to be heated up to 2000 °C. The furnace uses a graphite susceptor, insulated with graphite foam, mounted inside an alumina tube. The graphite susceptor is heated by

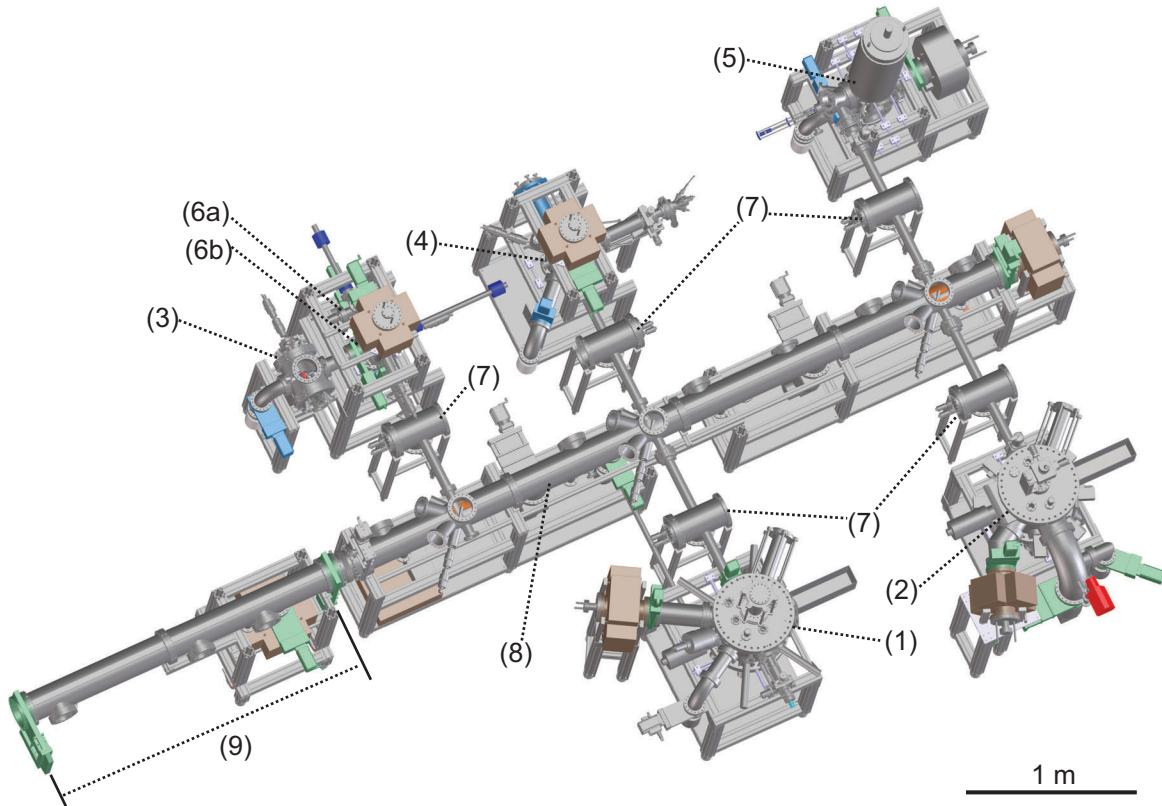


FIG. 2. 3D computer aided design (CAD) model overview of the processing lab in the ULTSPM facility at NIST. The lab hosts MBE growth chambers for metal (1) and for III-V semiconductor samples (2), an RF furnace (3), an FIM chamber for tip preparation and analysis (4), a stand-alone quick access cryogenic STM/AFM (5) and a two-stage load lock chamber (6a,b). Horizontal transfer chambers called 'bidirectional translator stations' (7) connect each chamber to the central interlab vacuum line (8). Part of this line (9) is portable and can be disconnected from the main system to decouple from the processing lab. This section (which has its own ion pump) can be moved to connect with the UHV chamber in the ULTSPM lab (Fig. 4). The portable part reaches through two hatches in the walls of the double shielded room to make the connection.

a water cooled RF coil surrounding the alumina tube. A gas handling system is attached to the furnace chamber allowing samples to be grown in various gas atmospheres. The furnace is used to grow epitaxial graphene on SiC substrates and is connected to the load lock system ((6b) in Fig. 2), so that samples, in principle, can be transferred through the facility. Currently, the graphene samples are grown without sample holders to avoid any contamination, and are taken out of the furnace system to mount on metal sample holders.

### 3. Field-Ion Microscopy System

The field-ion microscopy (FIM) system ((4) in Fig. 2) is designed for probe tip preparation and analysis. FIM enables the crystalline structure of a metal tip apex to be imaged with atomic resolution.<sup>48-50</sup> In operation we

apply a positive voltage (up to 20 kV) to the tip in the presence of He imaging gas (typically  $2 \times 10^{-3}$  Pa). The strong electric field close to the tip apex ionizes He atoms and the resulting ions are accelerated along diverging electric field lines to a nearby phosphor screen. Ionization of He atoms will be stronger in the regions of increased curvature (such as at step edges), and as a result these regions will be emphasized in the atomically-resolved image projected on the screen. Using the microscope with a negative tip potential (and without an imaging gas) enables Field Emission Microscopy (FEM), in which case regions of high electron emission are visualized on the imaging screen.

The FIM was constructed using a 25 mm chevron micro channel plate with integral phosphor screen,<sup>72</sup> which allows FIM at room temperature with He gas pressures in the range of  $2 \times 10^{-3}$  Pa. UHV high voltage feedthroughs are used for the screen and channel plate potentials. A

custom-designed linear motion manipulator with 360° rotation capability using a differentially pumped rotation stage is used to apply up to 20 keV to the probe tip.<sup>73</sup>

For tip cleaning and preparation, a tungsten filament electron-beam heater mounted on a linear translator is used. An integral resistive heater is also incorporated into the tip manipulator. In the FIM mode of operation the tip is cleaned further by field evaporation of its outer layers while watching the FIM pattern evolve. For the preparation of tips used in spin-polarized tunneling measurements, the chamber has four evaporators, which allow tips to be coated with various transition metals (Fe, Co, Cr, and Mn).

#### 4. Quick Access Low Temperature SPM System

An independent quick access low temperature STM/AFM ((5) in Fig. 2), fully separate from the main microscope, allows us to analyze samples relatively easily before inserting them into the interlab transfer line for transfer to the mK SPM system. The SPM is cooled by a liquid nitrogen shielded bottom loading cryostat<sup>74</sup> with visual access to the 4 K plate and the sample/tip region. A 12 L liquid helium volume allows approximately 4 days of measurement with this low loss cryostat. Vibration isolation is provided by an integral pneumatic system supporting the cryostat at its top, as well as a spring suspension system hanging from the cryostat 4 K plate. The design of the SPM module is nearly identical to that of the mK SPM, which is described in Section III in detail. Using the same tip and sample holder receptacles as the mK SPM allows samples and tip to be transferred from this instrument to the ULTSPM. All electronics are identical to those of the main ULTSPM system.

#### 5. Two-stage Load Lock System

Two separate chambers, connected in series, allow tips and samples to be transferred in and out of the UHV environments without venting a large volume of vacuum to atmosphere. The primary load lock ((6a) in Fig. 2) opens to air to load/unload tips and samples; up to 6 tips or samples can be stored in the linear translator. After the introduction of tips/samples, the primary load lock chamber is pumped and baked at 100 °C for  $\approx 12$  h before it is opened to the secondary load lock ((6b) in Fig. 2). In the secondary load lock chamber, which remains under vacuum always, up to 24 tips or samples can be stored on a motorized, 4-tier carousel. The secondary load lock is isolated from the interlab central vacuum line by a gate valve. The main purpose of the secondary load lock is to ensure that the interlab central vacuum line does not come in direct contact with the relatively poorer vacuum in the primary load lock and to maintain a clean vessel for storing of tips and samples.

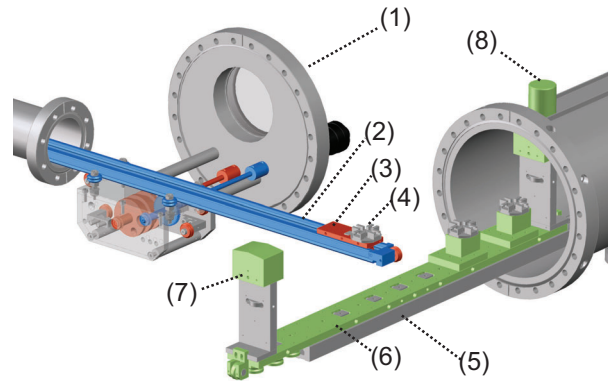


FIG. 3. 3D CAD model of a bidirectional translator station. Two rotational feedthroughs (blue and red) on the main 254 mm flange (1) control respectively the two-way motion of the rail (2) and the sled (3) on top of the rail. A 4-slot tip/sample holder carousel (4) is mounted on top of the sled. In the interlab vacuum line a fixed rail (5) supports a 0.61 m (24 inch) long sled (6). The sled has two posts with magnetic blocks (7) so it can be dragged along by a handheld magnet (8) on the outside of the vacuum system. This sled has two 4-slot carousels.

#### C. Tip and Sample Transport through the UHV Systems

All processing chambers are connected to the interlab central vacuum line through the sections called bidirectional translator stations ((7) in Fig. 2).<sup>75</sup> The central part of the bidirectional translator, shown in Fig. 3, is a 254 mm (10 inch) conflat-flange (CF) flange with two rotational feedthroughs. One feedthrough operates a rack and pinion system that controls the movement of the rail section ((2) in Fig. 3), which can be moved in two directions either into the interlab central vacuum line on one side, or into the processing chamber on the other. The second feedthrough is connected to a steel cable assembly that moves a sled ((3) in Fig. 3) back and forth on the rail, holding a 4-slot carousel for tips or samples ((4) in Fig. 3). The ability to move the rail itself is important, as it allows the gate valve to the processing chamber to be closed if the rail is retracted from the processing chamber, and it allows the main sled in the interlab central vacuum line to pass if the rail is retracted from the interlab vacuum line.

The interlab central vacuum line ((8) in Fig. 2) consists of a 203 mm (8 inch) OD tube at the bottom of which a fixed rail ((5) in Fig. 3) is mounted. The rail supports a 610 mm long sled ((6) in Fig. 3) which rides on a set of both horizontal and vertical ball-bearing wheels. The sled holds two more 4-slot tip/sample carousels, and has a vertical post with a magnetic block (electroless nickel plated 4130 steel) on top at each end ((7) in Fig. 3). The top of the magnets are in close proximity to the inner wall

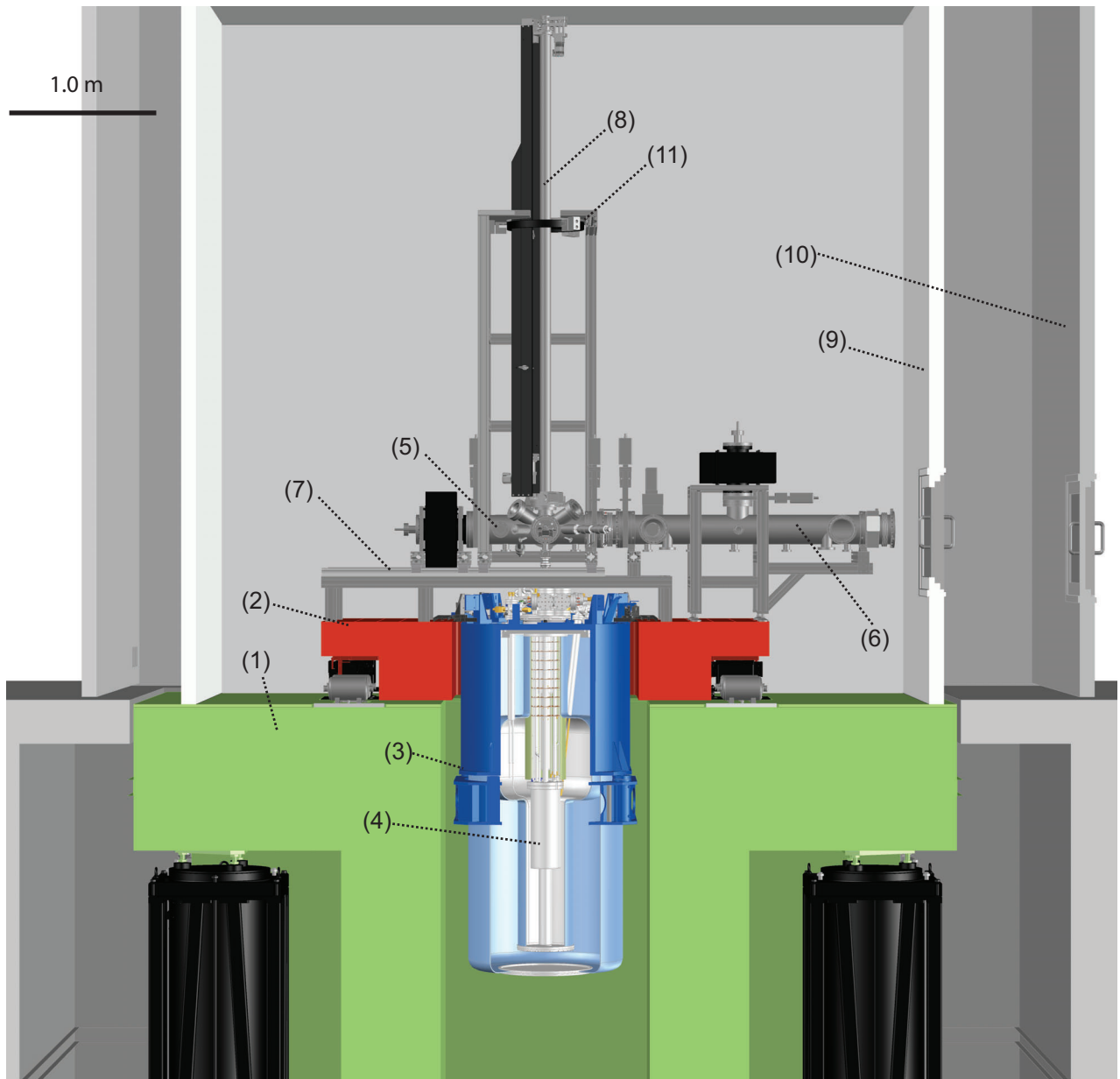


FIG. 4. 3D CAD model cross section of the double shielded ULTSPM lab. The inner room is built upon a separate  $\approx 110$  t concrete slab (1) supported by six actively controlled pneumatic isolators. A  $\approx 6$  t granite table (2), also with active pneumatic isolators, supports the measurement equipment. The  $\approx 1$  t cryostat (3), passively isolated, is mounted in a hole in the granite table and in the concrete slab. Inside the cryostat the dilution refrigerator insert (4) hangs directly immersed in the liquid helium bath. Above the cryostat the UHV chamber (5) links to the central interlab vacuum line (6) that provides access to the processing lab, which is located to the right of this image. The UHV chamber, if disconnected from the central interlab vacuum line, can be moved sideways to the left on a pair of rails (7) to allow the DR insert to be removed. A long vertical welded bellows translator (8) rotates inside a centering ring (11) and is used to move the SPM module into and out of the cryostat. The entire lab is shielded by an inner (9) and an outer (10) acoustic enclosure, the inner enclosure also acting as an RF shield. Two hatches in the walls (on the right) can be opened to connect the system to the processing lab.

of the vacuum tube. On the outside, a handheld magnet ((8) in Fig. 3) is used to translate the sled along the rail. The length of the sled is chosen to span the areas where there is no supporting rail, such as in the gate valve sections between the interlab linear system and the portable section ((9) in Fig. 2), and SPM chamber. The distance

between the two vertical posts is chosen such that at least one is always accessible to the handheld magnet, unobstructed by any flange, viewport or other feature. Tip or sample holders are moved between different carousels using wobble-stick manipulators. The manipulators are also used to manually rotate the 4-slot carousels to bring

the desired sample or probe tip into play.

The portable section of the interlab central vacuum line ((9) in Fig. 2) provides a means to transfer samples and tips from the processing lab to the ULTSPM lab, without compromising the integrity of the vibration isolation or acoustic/RF shielding of the ULTSPM lab. This portable section connects to the central vacuum line in the processing lab and the ULTSPM lab. The portable section extends into the double shielded room through hatches which can be closed when the portable section is removed for measurements. It is mounted on casters and has its own  $600 \text{ L s}^{-1}$  ion pump so that it can remain under UHV conditions even after being removed from the stationary part of the interlab central vacuum line. The portable section is re-connected to the interlab central line and ULTSPM vacuum system prior to (one day before) transferring tips/samples into the ULTSPM system. When reattaching the portable section, only two short bellows sections (one on either side of the part, each between two gate valves) need to be pumped and baked out, typically for 24 hours. Pumping of the bellows sections is done through a DN 40 port on the side of a gate valve's body. In both the interlab central vacuum line and the portable section, the rail holding the transfer sled is mounted on *X-Z*-positioners that can be adjusted vertically and perpendicularly to the rail in order to realign the different rail sections.

#### D. Cryostat Assembly and transfer of Tip, Sample, and SPM Module

A particularly difficult point in designing a low-temperature SPM system is to provide easy and reliable access to the scanner for tip and sample exchange. In our system we chose to make the cryostat accessible from the top (i.e. 'top loading'), such that the vacuum chamber is positioned above it. A cross section of the cryostat and the vacuum chamber, both located in the ULTSPM lab, is shown in Fig. 4. The cryostat ((3) in Fig. 4), which has a useable liquid helium volume of 250 l, is suspended in a hole of the granite table ((2) in Fig. 4) standing on the vibration-isolated ('floating') concrete slab ((1) in Fig. 4). The cryostat, granite table and concrete slab are each part of the 3-stage vibration isolation system described in Section V.

The dilution refrigerator is part of a 1.6 m long top loading insert ((4) in Fig. 4) mounted inside the cryostat. As drawn, the vacuum chamber ((5) in Fig. 4), which is the extension of the interlab central vacuum line ((6) in Fig. 4), blocks the opening at the top of the cryostat, preventing the insert from coming out of the cryostat. Therefore, the vacuum chamber needs to be decoupled from the interlab central vacuum line (through a bellows section identical to those used for the portable part of the vacuum line) and shifted to the side on a pair of linear rails ((7) in Fig. 4). A crane can then be positioned over the cryostat to lift the insert up or down.

The insert is only taken out very infrequently to perform repairs or add new functionality, for example, adding the cryogenic preamplifier (see Section VI). The top port of the insert can be closed by a 70 mm (2.75 inch) UHV gate valve. It can be pumped and baked as a separate UHV chamber in a specially designed frame (which is an assembly stand and also bakeout furnace) before immersing it into the liquid helium cryostat. For this purpose a separate turbomolecular pump is connected temporarily to the top valve of the insert. Baking of the insert is limited to  $50 \text{ }^\circ\text{C}$  on the still plate and mixing chamber due to the sensitivity of the thermometers and silver-sintered heat exchangers in the DR. After the insert is baked and placed inside the cryostat, the vacuum chamber is connected to the interlab central vacuum line by a short flexible welded bellows section and to the insert with a second 70 mm gate valve. These two valves allow the DR and top vacuum chamber to be sealed and isolated as the DR insert is removed or installed. A small welded bellows section is placed between these two valves to decouple the cryostat from the vacuum chamber, creating separate isolation stages (see Section V). The small bellows section separating the vacuum chamber and the DR insert needs to be pumped (by a small side port) and baked before opening the two DN 40 valves to form a continuous vacuum system. Incorporated into this small bellows section is a ceramic break to isolate the cryostat ground from the vacuum chamber and building grounds.

A 3.3 m tall linear translator<sup>75</sup> ((8) in Fig. 4) is positioned on top of the vacuum chamber and used to transfer the SPM module (described in Section III) into the DR when a new sample and tip are loaded into the SPM. Typically, a study may last from one to several months on a given sample. The translator used to transfer the SPM module consists of tall welded bellows to translate a 25 mm OD shaft the length of the DR,  $\approx 2.8 \text{ m}$ . On top of the translator is another welded bellows section with 50 mm travel and is used to translate a coaxial 9.5 mm OD pushrod to actuate shutter mechanisms described below. The entire linear translator is mounted on top of a two-stage differentially pumped rotary platform that can rotate the entire linear translator by  $360^\circ$ . A centering ring built into the structural frame and positioned about half way up the translator (11 in Fig. 4), is used to keep the translator on center with spring loaded rollers as it rotates the translator. The linear translator is used to translate the SPM module and to place up to two radiation shields (shutters) in the top UHV tube of the insert. Figure 5(a) shows a shutter as it is picked up by the bayonet fixture at the bottom end of the translator. An exploded 3D CAD model of the shutter is shown in Fig. 5(b). An almost identical assembly is mounted to the top of the SPM module (the only difference being a small hole in the bottom plate to allow low-temperature evaporation of atoms onto the sample), so we will use the term 'shutter' to refer to both radiation shields and the assembly at the top of the SPM module.

The top of the shutters are constructed to mate with

the bottom bayonet coupling of the translator (Fig. 5). On top of the shutter assembly there are two hook-shaped anchors, facing radially outward from one another. The bottom of the translator has two matching anchors, oriented tangentially. The translator can dock to the shutter much like a bayonet mount by engaging its anchors to the shutter's anchors through a  $\approx 70^\circ$  rotation ((using the rotary platform). Once engaged, the central pushrod inside the translator, which can be moved independently by the short bellows on top of the main translator, is extended. The end of the pushrod is shaped like an arrowhead and has a total stroke of 20 mm. When retracted, the wings of the shutter are extended ((c) in Fig. 5) and the shutter

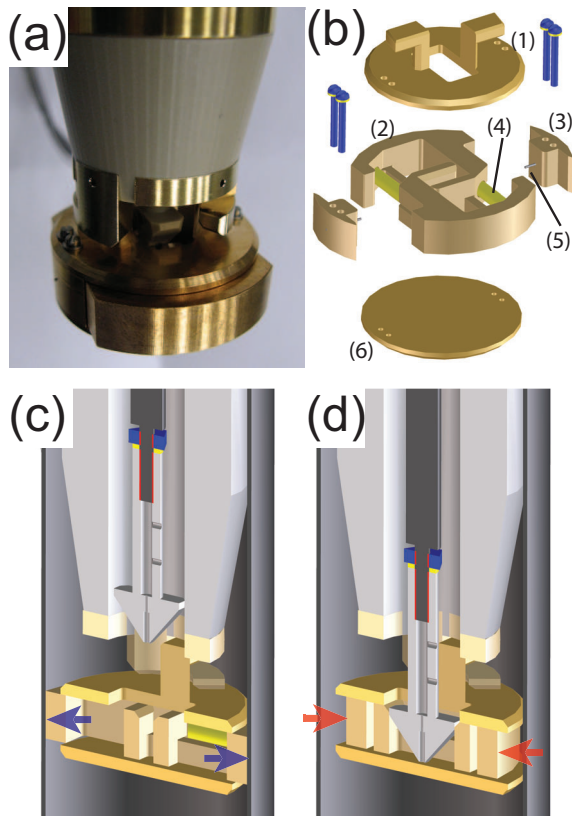


FIG. 5. Translator bayonet coupling mechanism and radiation-blocking tube shutter design. (a) A photograph of a tube shutter held by a translator. (b) 3D CAD model of the tube shutter assembly: (1) top cover, (2) side wings, (3) side post, (4) coil spring, (5) tungsten wire, and (6) bottom cover. (c)-(d) Cross sectional views of the shutter operation in a tube. (c) Retracting a push-pin (gray colored arrow), the side wings extend out by the force of the internal coil spring, and push against the tube wall, fixing the shutter solidly in the tube. (d) To release and pick up the shutter, a center push-rod pushes into the center of the shutter to retract the side wings with the tube shutter supported on the translator anchors. In this way the tube shutter can be positioned in the DR central tube at any desired height to block thermal radiation.

is held in the tube by frictional forces controlled by coil springs in the shutter assembly ((4) in Fig. 5(b)). At the same time, when extending the pushrod, the shutter assembly is fixed securely onto the anchors of the bayonet mount. In order to monitor translator operations without optical access, the translator is equipped with five metal electrodes that act as touch sensors: four on the bayonet and one on the pushrod. All three independent motions (translation, rotation and pushrod extension) are motorized and controlled by a computer.

Upon reaching the bottom of the insert, the SPM module is mounted into a receptacle. The SPM module is locked into place by extending the shutter wings below the ledge in the Ag tube. This process will be discussed in more detail in Section III. For room-temperature testing of the SPM and visual alignment of tips/samples, a second electrical receptacle for the SPM module is located on a sled inside the ULTSPM vacuum chamber. This is similar to the tip/sample sled described earlier. After lifting the SPM module above the sled translation rail (which has a hole above the insert for the translator to pass through), the sled with the second SPM electrical receptacle can be positioned to mount the SPM module into the receptacle. This receptacle, just like its low-temperature counterpart, has contacts for all the signals needed for SPM operation such as, tip signal, sample signal, and piezoelectric motors and scanner.

### III. SPM MODULE

#### A. Overview

One of the main technical challenges in scanning tunneling microscopy is to coarse-position a tip close to a sample so as to form a stable tunnel junction without causing the tip to crash into the sample. In order for this to work, an SPM module needs to meet two requirements. First, the coarse positioner should have a reliable step size smaller than the full  $Z$  travel range of the scan piezo. Second, in order to maintain a stable tunneling gap, the body of the module has to be very rigid. A number of clever designs have been developed to accomplish these tasks, and we review a few of them in use in cryogenic SPMs.

The first SPM,<sup>44,45</sup> which was invented at IBM Research in Zurich, Switzerland, adopted a ‘louse’ type stepper. A louse has a piezoelectric plate onto which a tip or sample is mounted. The plate can be elongated or contracted horizontally by applying a voltage across the plate. Three metal feet, insulated from three bottom metal plates by a high dielectric-strength material, support the piezoelectric plate. Each foot can be clamped or unclamped by applying voltages to the bottom plate below it, while elongations and contractions of the piezoelectric plate control its horizontal motion. The louse has both  $Z$  and  $X$  motions ( $Z$  is the direction in which the tip approaches the surface), and has been used, with re-

finements, quite successfully at low temperature (4 K).<sup>7</sup>

In 1987, a few years after the first successful demonstration of SPM, a new type of piezoelectric coarse positioner was reported: the so called Beetle type (or Besocke type) positioner.<sup>76,77</sup> In this design, three piezoelectric tubes support a circular plate above a fourth piezoelectric tube in the center. The tip is fixed to the central tube while the sample is mounted onto the bottom of the circular plate. This plate has three identical ramps, spaced by  $120^\circ$ , with each of the supporting tubes contacting one ramp through a polished metal or sapphire ball. By a tangential stick-slip shearing motion of the three piezoelectric tubes across the ramps, fine adjustments of the tip-sample distance can be made. In addition, the Beetle positioner can be used for lateral coarse motions by moving the supporting piezoelectric tubes in Cartesian directions, and can be made very small because of its simple structure. It is widely used in current low temperature SPM applications.<sup>14</sup>

Another coarse positioner common in SPM applications is the Pan-type walker.<sup>11,78</sup> This positioner is superior for cryogenic applications over the louse or Beetle type due to its rigid structural design. The structural design is important for cryogenic applications since it is not always possible to place vibrational isolation close to the microscope if good thermal contact is desired. This type of positioner consists of a triangular or hexagonal prism with polished sides - often made of sapphire - clamped inside a main body by six shear-piezoelectric legs: one pair on each side. Two of the pairs are mounted directly onto the body, while the remaining pair is mounted onto a beam that is pushed down by a plate spring with stiff tension. A scanning piezoelectric tube holding the tip or the sample is located inside the prism. The positioner can be operated either in stick-slip mode or in inertia mode. In stick-slip mode, all legs first move sequentially in one direction via a quick displacement that leave the prism in place (slip phase), and then all legs move simultaneously and slowly in the opposite direction, causing the prism to move (stick phase). Inertial mode is identical to stick-slip mode, except that in this case the legs move simultaneously in both the slip and stick phases. The Pan-type positioner inherently has a very rigid structure (high resonance frequencies) due to the stiff clamping of the prism by the piezoelectric motors, and has demonstrated stable performance in low temperature applications. It can also be adapted for lateral coarse motion by replacing the prism with a planar structure. In our instrument we adopted the Pan-type positioner both for  $Z$  coarse motion of the sample and for  $XY$  coarse motion of the SPM tip based on one of the authors' (JAS) 4 K SPM design.

## B. SPM Module for mK Applications

For applications at very low temperatures and in high magnetic fields (10 mK and 15 T in our work), material properties such as magnetism, superconductivity and

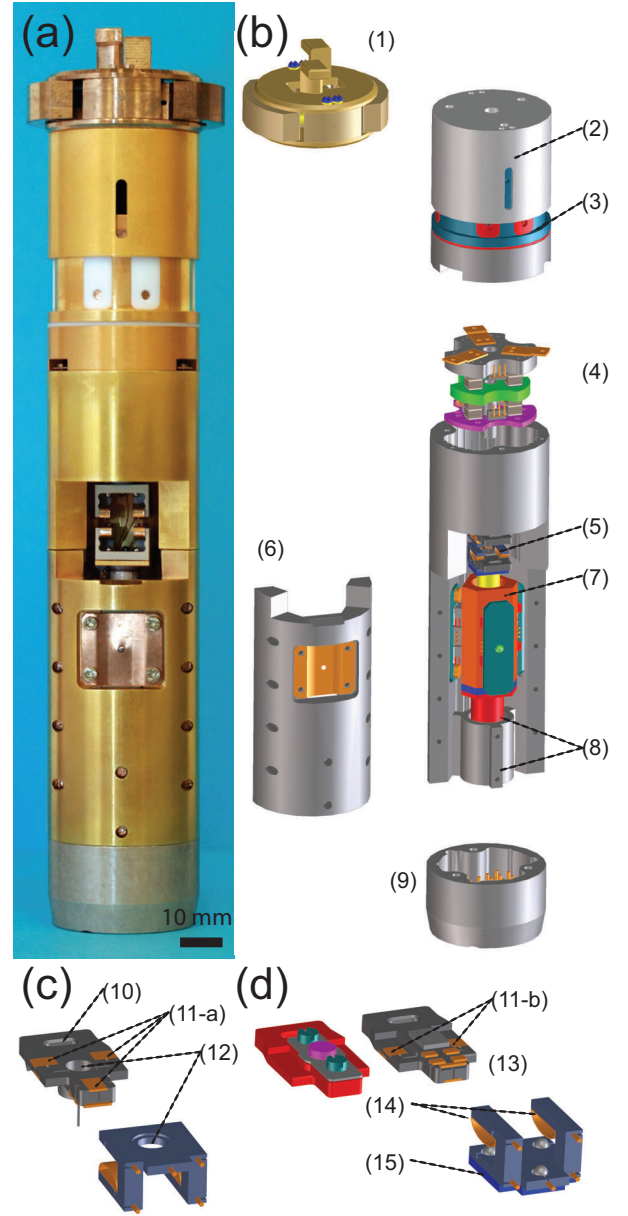


FIG. 6. Photograph and 3D CAD models of the SPM module and parts. (a) Front view photograph of the SPM module. (b) 3D CAD models showing parts of the SPM module unit. (c) 3D CAD model of the SPM tip holder and its receptacle. (d) 3D CAD model of the SPM sample holder and its receptacle. Label details: (1) a tube shutter module used to clamp the SPM module, (2) compression stage with inner compression spring, (3) rotation stage for pin alignment, (4) piezoelectric motors for  $XY$ -coarse motion, (5) receptacles for the SPM tip and a sample (details are shown in (c) and (d)), (6) front cover with a plate spring of the  $Z$ -motor, (7) piezoelectric motors for  $Z$ -coarse motion, (8) capacitance sensor to measure  $Z$ -coarse motion, (9) bottom cover including all signal pins, (10) slot for wobble stick operation, (11-a) and (11-b) three bottom and two top signal contacts for both the SPM tip holder and sample holder, (12) center hole for *in-situ* evaporation and optical access, (13) five contact points to be used between device leads and signal contacts (11), (14) spring clip for kinematic and electric contact, (15) ground plane.

thermal conductivity need be considered in depth. The main body of our SPM module and most small metal parts are made of coin silver,<sup>79</sup> which is an alloy of 10 % copper and 90 % silver. This material is rigid, easily machinable and still has a high thermal conductivity in the mK regime.<sup>80</sup> To prevent oxidation, coin silver parts used in the SPM module have been gold-coated. Clips, screws, and the plate spring for the  $Z$  and  $XY$  coarse positions are made from BeCu. Tungsten balls are used for kinematic and electrical contacts in tip and sample receptacles. The prism and the sliding plate for the  $Z$  and  $XY$  coarse motions are made of sapphire, and all other insulating materials are either alumina or polyether ether ketone (PEEK).

Figures 6,(a)and(b) show a photograph and a 3D CAD model of the SPM module. The SPM module is transferred from the room temperature UHV chamber above the cryostat into the silver receptacle in the DR after the tip and sample are prepared and inserted *in-situ* (see Section II). The module is connected to a shutter mechanism (1) identical to the tube shutter described previously (Fig. 5), which can couple to the vertical translator when transferring the SPM module into and out of the cryostat. A compression stage with a coil spring inside (2 in Fig. 6) and a rotation stage (3) allow the unit to be guided and locked into the receptacle. In the receptacle, three guide pins determine the orientation of the module to make the gold-plated signal contact pads at the bottom of the module (9) line up with matching contact pins in the receptacle. When lowered into the receptacle, the part of the module below the rotation stage can freely rotate to adjust to these guide pins. Upon reaching the bottom of the receptacle, the vertical translator continues to push down to compress the compression stage. A custom-made coil spring inside the compression stage ensures a sufficient force to make good kinematic and thermal contact between the module and the receptacle. Approximately 15 cm above the receptacle a ledge narrows in the Ag tube through which the module is lowered. Pressure from the compression stage locks the SPM module securely in place when the wings of the ‘shutter’ mechanism are extended below this ledge. After locking in the SPM module, the translator is withdrawn to the room temperature UHV chamber to pick up two tube shutters, which are then placed inside the DR neck.

The designs of the  $Z$  and  $XY$  coarse motions, (7) and (4) in Fig. 6(b), are based on the Pan type positioner. In the  $Z$  positioner, each leg consists of four stacked shear-piezoelectric plates (5mm x 5mm x 0.5 mm thick with Cu electrodes),<sup>81</sup> separated by 12  $\mu\text{m}$  thick BeCu foil electrodes. The top and bottom of the stacks are covered with a 0.5 mm thick alumina plate for planar contact to the sapphire prism, and for securing the motor to the module body. The plate spring for the  $Z$  positioner is located in the front cover (6) and secured with Allen cap screws that can be adjusted in vacuum using a wobble stick fitted with an Allen drive screwdriver.<sup>82</sup> An optimal walking step size can be determined by adjusting

the  $Z$  tension plate in vacuum. The difference in friction between atmospheric and UHV environments can be compensated by adjusting the tension in vacuum. As seen in Fig. 7(a), at small tension the backward motion (in the direction of gravity) is larger than the forward motion, because the prism falls slightly during the fast slip motion. As the tension is increased, the backward step size decreases and forward step size increases toward a common value. The dependence of the step size on the voltage amplitude is shown in Fig. 7(b). The forward motion slope yields a motor gain of  $1.31 \text{ nm V}^{-1}$ , which is in agreement with the expectations for the gain from four shear piezoceramic plates:<sup>81</sup>  $4 \times d_{15} = 1.32 \text{ nm V}^{-1}$ , where  $d_{15}$  is the relevant shear component of the piezoelectric tensor.

A coaxial capacitance sensor (8 in Fig. 6(b)) enables detection of the  $Z$  motion when there is no optical access to the SPM module. The inner electrode of this sensor is mounted to the bottom of the sapphire  $Z$ -prism while the outer electrode is fixed to the main body. The capacitance,  $C$ , per length,  $L$ , (neglecting edge effects) is given by,

$$C/L = \frac{2\pi\epsilon_0}{\ln(b/a)}, \quad (2)$$

where  $a = 9.1 \text{ mm}$  and  $b = 10.7 \text{ mm}$ , are the inner and outer electrode diameters respectively, and  $\epsilon_0$  is the permittivity of free space. Equation 2 yields a change in capacitance per unit length of  $0.36 \text{ aF nm}^{-1}$ , which agrees well with the capacitance bridge<sup>83</sup> measurements shown in Fig. 7(c) that determine  $C/L = 0.37 \text{ aF nm}^{-1}$ . Figure 7(d) shows the capacitance sensor signal as a function of drive-voltage amplitude applied to the  $Z$ -piezo motors. A forward/reverse per step average value of  $0.47 \text{ aF V}^{-1}$  is observed in agreement with the above capacitance sensor and piezo motor values, (*i.e.*  $1.3 \text{ nm V}^{-1} \times 0.37 \text{ aF nm}^{-1} = 0.48 \text{ aF V}^{-1}$ ), which demonstrates that single steps can be sensed with sufficient averaging time.

In the  $XY$  positioner there are three compound motors on top and three on the bottom of a sapphire plate, each consisting of eight shear-piezoelectric plates ( $4 \text{ mm} \times 4 \text{ mm} \times 0.5 \text{ mm}$  thick with Cu electrodes),<sup>81</sup> four plates for  $X$  and four plates for  $Y$ . The bottom motors are fixed to the body while the top motors are attached to a coin-silver plate that is clamped by three BeCu plate springs. The  $XY$  positioner is initially used at room temperature to position the tip over the chosen sample area within a range of  $\pm 1.5 \text{ mm}$ . At low temperature the  $XY$  positioner allows different areas of the sample to be surveyed. Measurements of the  $XY$  motion at low temperature were made by comparing the displacement of features in STM topographs. At 10 mK measurements indicate a lateral step size of  $\approx 20 \text{ nm}$  with a drive-voltage amplitude of 500 V.

The tip and sample stages (5) are displayed in more detail in Figs. 6, (c) and (d), respectively. In a tip or

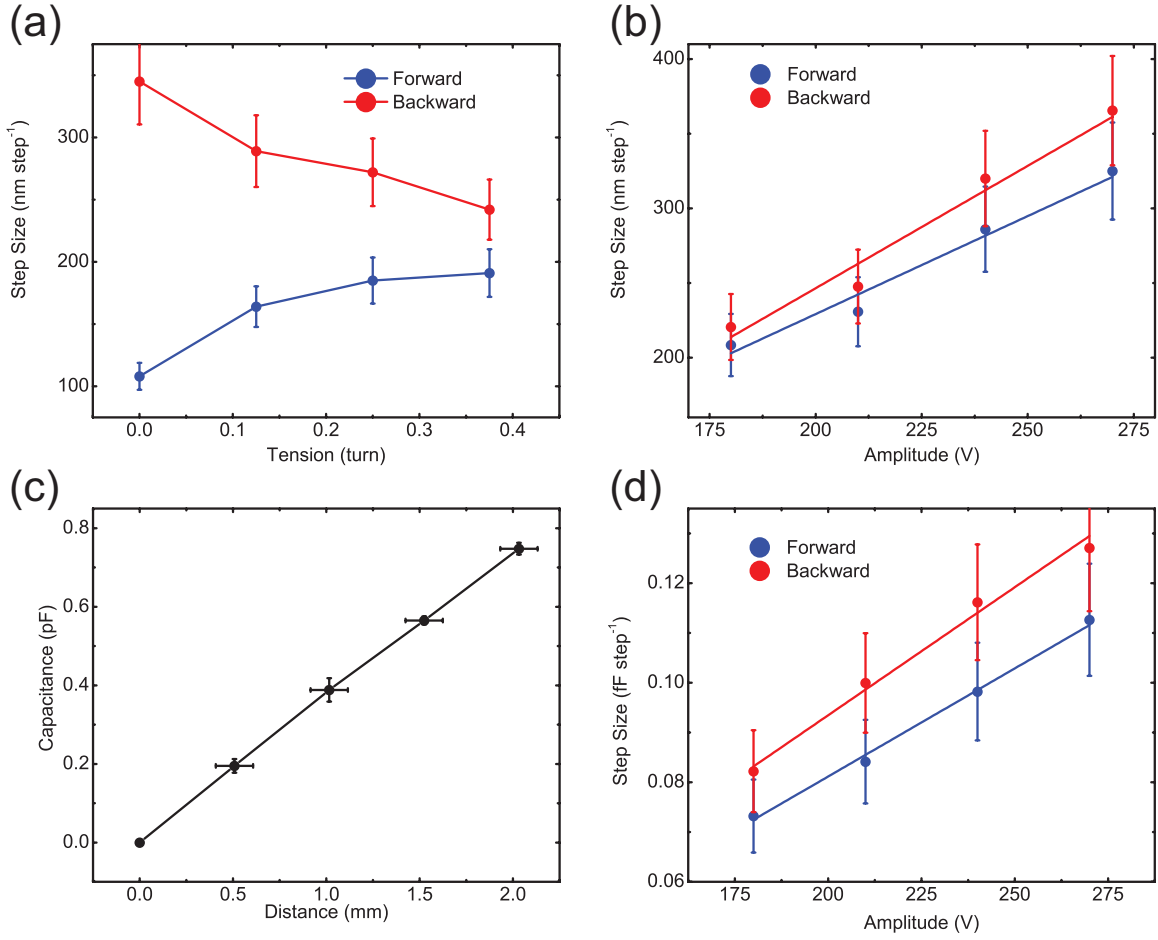


FIG. 7. Characteristics of the Z-piezo motor driven by the NIST piezo motor controller. (a) Step size vs. spring tension using a 210 V drive-voltage amplitude. The spring tension for the Z-motor was adjusted *in-situ* by rotating one of the four screws holding the clamping plate using a UHV wobble stick. (b) Step size vs. signal amplitude after optimizing the motor tension. The solid lines are linear fits with slopes,  $1.31 \text{ nm V}^{-1}$  and  $1.64 \text{ nm V}^{-1}$ , for the forward (blue) and backward motion (red), respectively. (c) Calibration data for the capacitance sensor inside of the SPM module. The capacitance change scales linearly with piezo motor motion with a slope of  $0.37 \text{ aF nm}^{-1}$ . (d) Capacitance sensor measurements of the motor step size vs. drive-voltage amplitude. The solid lines are linear fits with slopes,  $0.43 \text{ aF V}^{-1}$  and  $0.51 \text{ aF V}^{-1}$ , for the forward (blue) and backward motion (red), respectively. All measurements in (a) to (d) were made in UHV at room temperature. The step sizes and distances were measured using using an optical telescope on a theodolite. The step sizes were determined by measuring the number of steps to move the motor 1 mm. Errors bars in distance measurements represent one standard deviation in uncertainty in the determination of the distance traveled using the optical theodolite.

sample holder receptacle, three tungsten balls on the bottom and two BeCu clips on the top are used for kinematic and electrical contacts to the holder. All of the tip and sample holders have the same overall shape, but detailed features and material choice vary for different applications. Tip holders are made from machinable ceramics or plastics (PEEK), and can have up to five independent electrodes: three contact pads on the bottom face (see 11-a in Fig. 6(c)) and 2 more contact pads on the top face (see 11-b in Fig. 6(c)). These contacts can be used, for example, for electrical device geometries, or tuning-fork AFM applications. The electrical contacts are connected to five anchor pins on the back side of the tip and sample holder receptacle for wire connections. Both tip

holder and tip receptacle have a hole through the center (see 12 in Fig. 6(c)) for *in-situ* low temperature adatom evaporation onto the sample surface.

Sample holders for metal or semiconductor samples (left in Fig. 6(d)) are made from either pure Ag or pure Cu. Single crystal samples can be mounted onto the holder with a Mo plate spring and two M1 Mo or Ta screws. An alternative version of the sample holder (right in Fig. 6(d)) can be used for multi-contact device measurements. These sample holders are made from machinable ceramics or PEEK and have up to five independent contact pads, similar to the tip holders. Because the sample receptacle is located on top of the piezoelectric tube scanner, an electrical ground plane (see 15 in Fig. 6(d))

directly underneath the receptacle prevents interference from the piezo signals. In addition, a ruthenium oxide bare chip thermometer sensor is glued onto the ground plane. The dimensions of the piezoelectric tube scanner are 5 mm diameter, 0.8 mm wall, and 32 mm long,<sup>81</sup> with four silver electrodes on the outer wall and a single silver electrode on the inner wall, which gives a scan range of approximately  $3 \mu\text{m} \times 3 \mu\text{m}$  at mK temperatures. All the electrical connections for tip signal, sample signal, tube scanner, coarse motion, capacitance sensor and temperature sensor are connected through 40 electrodes on the bottom pin-pad of the SPM module (see 9 in Fig. 6(b)).

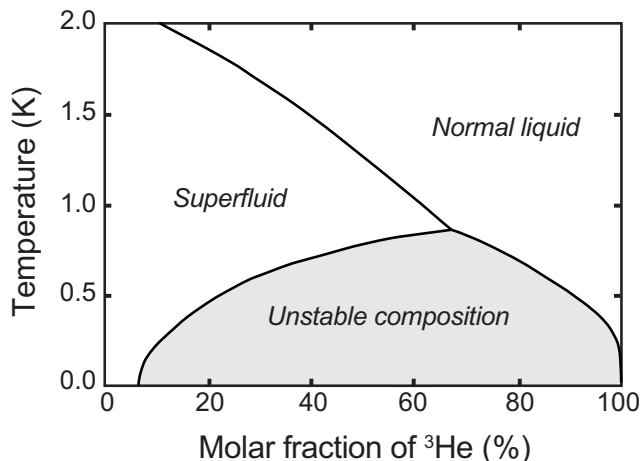


FIG. 8. Phase diagram of the  ${}^3\text{He}$ - ${}^4\text{He}$  mixture. Below 870 mK (the triple point) the mixture undergoes a spontaneous phase separation into a  ${}^3\text{He}$ -rich phase and a  ${}^3\text{He}$ -dilute phase. At  $T = 0$  K, the  ${}^3\text{He}$ -rich phase approaches 100 %  ${}^3\text{He}$ , but the  ${}^3\text{He}$ -dilute phase maintains a finite  ${}^3\text{He}$  concentration of 6.4 %. Adapted from reference 85.

#### IV. A DILUTION REFRIGERATOR FOR SPM

##### A. Cryogenic Techniques for $T < 4$ K

Currently the main methods to cool massive objects below 4 K are evaporative cooling of liquid  ${}^4\text{He}$  to temperatures of  $\approx 1.5$  K and of liquid  ${}^3\text{He}$  to 300 mK, Joule-Thomson cooling, and  ${}^3\text{He}$ - ${}^4\text{He}$  dilution refrigerators.<sup>84-86</sup> In the  ${}^4\text{He}$  evaporative refrigerator, the so-called ‘1 K refrigerator’ or ‘1 K pot’, low temperature is usually achieved by pumping on a small reservoir of  ${}^4\text{He}$ , that is replenished from the main  ${}^4\text{He}$  bath through a permanent flow restriction ‘impedance’ or an adjustable needle valve.

In a  ${}^3\text{He}$  refrigerator,  ${}^3\text{He}$  gas is condensed to the liquid state through thermal contact with a 1 K pot, and then the liquid  ${}^3\text{He}$  is pumped on by an internal charcoal sorption pump or external mechanical pump, cooling the liquid further down to somewhat below 300 mK.<sup>20-22,25</sup>

Most of the charcoal-pumped  ${}^3\text{He}$  refrigerators employ a single pump in a single-shot regime, limiting its lowest achievable, or ‘base’ temperature holding time available for measurements. This time depends on the total amount of  ${}^3\text{He}$  in the system, charcoal pump efficiency and heat loads to the microscope, and could make obtaining high density SPM spectroscopic maps rather challenging. Continuous cycle systems yield a constant but higher base temperature due to the incoming  ${}^3\text{He}$  heat load.

Alternatively,  ${}^4\text{He}$  or  ${}^3\text{He}$  gas can be cooled in a Joule-Thomson (JT) cycle with continuous circulation by using an external pump. In the JT cycle the gas is first pressurized and pre-cooled using an external cooling mechanism like a pulse-tube refrigerator, or refrigerant, such as liquid  ${}^4\text{He}$  for example. Next the gas is allowed to expand adiabatically through a JT valve or flow impedance thus significantly reducing its temperature. After cooling the load (the SPM), the returning gas is thermally coupled to the incoming gas via a counter-flow heat exchanger, increasing process efficiency. This method has been used successfully in the operation of an SPM at 0.5 K.<sup>23</sup> This technique can also be used for mixture condensing in a dilution refrigerator and is explained below in more detail.

The option which gives by far the lowest temperature is the  ${}^3\text{He}$ - ${}^4\text{He}$  dilution refrigeration. In addition to conventional evaporative cooling, a dilution refrigerator relies on the thermodynamic properties of the liquid  ${}^3\text{He}$ - ${}^4\text{He}$  mixture at low temperatures (see Fig. 8). In the isotopic phase diagram of  ${}^3\text{He}$ - ${}^4\text{He}$  mixtures shown Fig. 8, one can see two unique features of these two stable helium isotopes which make this type of refrigeration possible - they separate into two phases with different concentrations below 1 K, and there is a finite solubility of 6.4 %  ${}^3\text{He}$  in dilute  ${}^4\text{He}$  even at  $T = 0$  K.

In a typical DR a mixture of about 25 %  ${}^3\text{He}$  in  ${}^4\text{He}$  is first liquefied, filling its chambers and heat-exchangers. The upper chamber called a still is then pumped by a dedicated set of hermetically sealed closed loop pumps to maintain a steady circulation of  ${}^3\text{He}$ . After phase separation, liquid phases distribute in such a way that a phase separation boundary settles in a lower chamber called the mixing chamber (MC). Here a  ${}^3\text{He}$ -rich (concentrated and thus lighter) phase floats atop the  ${}^3\text{He}$ -poor (diluted) phase. Driven by osmotic pressure  ${}^3\text{He}$  is transferred through the dilute phase to the still located above the MC. Since the still contains the liquid-to-gas interface and there is significant amount of  ${}^3\text{He}$  in the vapor even below 1 K, it is cooled through conventional evaporative cooling. Tubular and sintered powder (typically ultra-fine silver) heat exchangers are used to improve the cooling efficiency, resulting in base temperature in the MC below 10 mK and a rather large cooling power as compared to any other methods in this temperature range.

For most of the applications where such refrigeration techniques are used the internal sources of vibrations

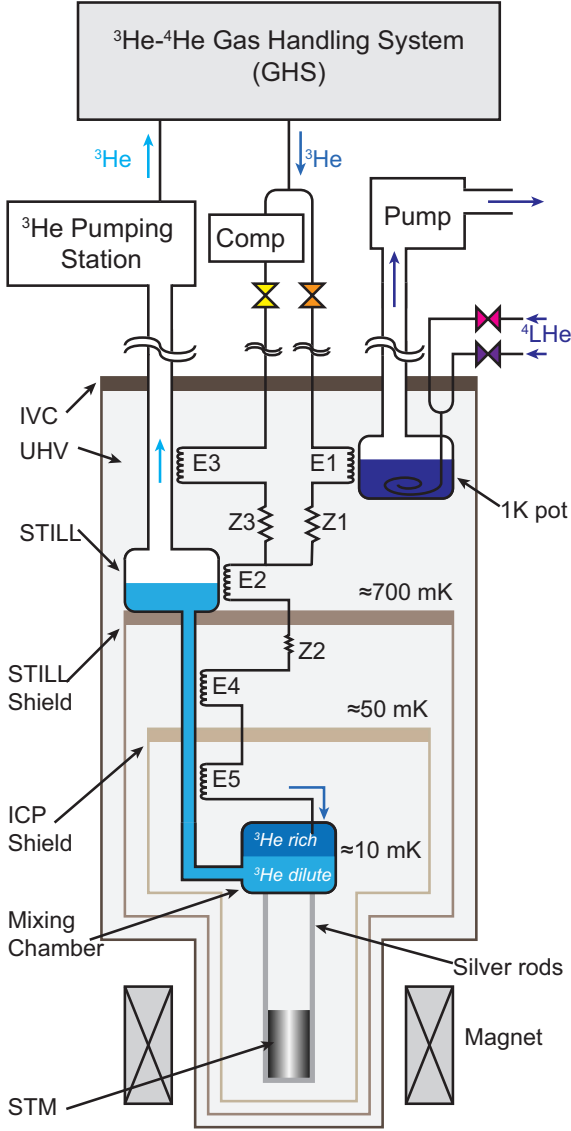


FIG. 9. Schematic drawing of the NIST dilution refrigerator system. There are five heat exchangers: E1 for the 1K pot, E2 for the still, E3 for the JT condenser, E4 a continuous heat exchanger, and E5 a sintered silver heat exchanger. Z1 is the main impedance for the 1K pot condensing mode and Z3 is the impedance for the JT condensing mode. These two condensing modes can be switched by two independent valves (colored yellow and orange). Z2 is a secondary impedance to prevent a backdraft of  $^3\text{He}$ . Two needle valves for the 1K are shown, which can be controlled manually (pink colored) or automatically (purple colored). The JT return line includes a compressor (labeled Comp) for high flow operation.

caused by condensation, evaporation (boiling) or high-speed gas or liquid flow are negligible and do not interfere with measurements. But the very first attempts to perform cryogenic SPM microscopy in the sub-Kelvin temperature range showed that the process of constantly

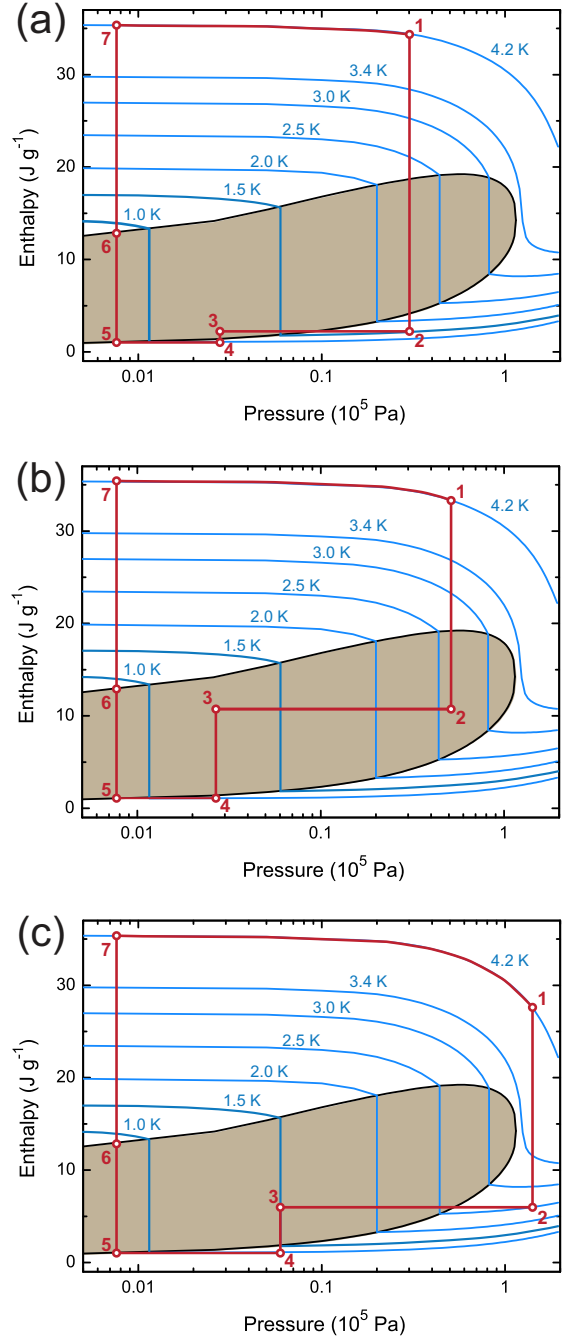


FIG. 10. Enthalpy vs. pressure diagram for  $^3\text{He}$  with simplified closed cycle paths for the three different condensing modes used in the DR (see text). (a) Cycle for the 1 K pot condensing mode. (b) Cycle for the JT condensing mode with a low return pressure and flow rate. (c) Cycle for the high pressure JT condensing mode using a compressor for high flow operation. Figure adapted from reference 90.

filling the 1 K pot reservoir caused significant intrinsic vibration problems.<sup>87-89</sup> Potentially, any liquid boiling or high speed flow turbulence caused by rapid expansion in a confined geometry can excite acoustic resonances and produce structural vibrations above the acceptable lim-

its of SPM applications. A few different design solutions have been provided to overcome noise problems caused by normal helium injection into super-fluid He in 1 K pots, resulting in significant acoustic noise reduction.<sup>87–89</sup> A careful design approach was needed in the current system to minimize or eliminate any possible intrinsic, as well as extrinsic noise sources in order to reach our measurement goals.

The DR described below has been designed with this goal in mind and its schematic is shown in Fig. 9. To optimize the condensation process, it was decided to incorporate a fully removable hybrid mixture condensing unit, comprised of both 1 K pot and JT condensers to be used in turns. Circulating  $^3\text{He}$  (which is always mixed with some  $^4\text{He}$ ) can be condensed in two different ways in this refrigerator through two dedicated return lines by operating corresponding shut-off valves. The mixture is initially condensed by a traditional 1 K pot condenser cooled to 1.5 K by a dedicated pump. In this case  $^3\text{He}$  is first pre-cooled to 4.2 K inside the main helium bath copper mesh heat-exchanger (point 1 on Fig. 10(a)). It fully liquefies and cools inside the heat-exchanger or condenser E1 using the 1 K pot cooling power (point 2 on Fig. 10(a)). At the next step it is allowed to expand through the flow impedance Z1 (primary impedance,  $3 \times 10^{10} \text{ cm}^{-3}$ ) (point 3 on Fig. 10(a)). The mixture warms somewhat during this adiabatic expansion process due to the positive slope of the isotherms in this region of the phase diagram. If it is allowed to expand to the very low pressure at which the DR normally operates (less than 100 Pa), point 3 will end up inside the two-phase part of the phase diagram resulting in partial evaporation and cooling of  $^3\text{He}$  inside the primary impedance. To avoid a non-desirable scenario when final condensation occurs inside the E4 heat-exchanger, there is a secondary flow impedance Z2 ( $7 \times 10^9 \text{ cm}^{-3}$ ) located between the still E2 and continuous E4 heat exchangers. This allows for constant pressure cooling and final condensation inside the still heat-exchanger E2 (point 4 on Fig. 10(a)). Adiabatic and almost isothermal expansion in Z2 delivers  $^3\text{He}$  into E4 fully liquefied at any of the circulation rates used.

Alternatively, in this system  $^3\text{He}$  can be condensed with the Joule-Thomson method<sup>90</sup> as explained in Figs. 10(b) and 10(c). For the JT mode another return line is used equipped with a small bellows compressor<sup>91</sup> right after the main pumps. At low circulation rates below  $\approx 200 \mu\text{mol s}^{-1}$  the  $^3\text{He}$  is pressurized to about 50 kPa to 100 kPa (0.5 bar to 1 bar) absolute pressure by the main pumps while being cooled to 4.2 K inside the liquid helium bath by another copper mesh heat-exchanger (point 1 on Fig. 10(b)). Then this gas is cooled and partially liquefied inside E3, a spiral-in-tube heat-exchanger of the JT condensing loop, using the enthalpy of the  $^3\text{He}$  gas pumped from the still chamber of the dilution stage by the pumps (point 2 on Fig. 10(b)). After that it is allowed to adiabatically expand via JT impedance Z3 ( $1 \times 10^{12} \text{ cm}^{-3}$ ) cooling further and

undergoing some further evaporation before entering E2 (point 3 on Fig. 10(b)).

At circulation rates above  $200 \mu\text{mol s}^{-1}$  a compressor is needed when using the JT mode to increase the return pressure of the  $^3\text{He}$  gas. This regime provides for maximum cooling power, and thus quick cooling to base temperature. The dynamic equilibrium pressure is above the critical pressure of  $^3\text{He}$  and no condensation occurs (point 1 and 2 on Fig. 10(c)) during pre-cooling inside E3 and partial condensation occurs only during the expansion through Z3 into E2. At Z2 both condensing paths merge. As described above final condensation and cooling takes place inside the still heat-exchanger E2 at typically 0.6 K to 0.9 K due to the presence of the secondary flow impedance Z2 (points 3 and 4 in Figs. 10, (b) and (c)) and the excessive still cooling power. At point 4 concentrated liquid  $^3\text{He}$  takes final expansion and enters the heat-exchangers E4 and E5 and the mixing chamber, where it undergoes mixing with  $^4\text{He}$  (point (5)).

The total cooling power at the interface between the concentrated and dilute phases inside the MC results from the heat of mixing as  $^3\text{He}$  is extracted from the  $^3\text{He}$  rich phase to the dilute phase,<sup>84</sup>

$$\dot{Q}(T) = \dot{n}_3[H_{3d}(T) - H_{3c}(T)], \quad (3)$$

where  $\dot{n}_3$  is the  $^3\text{He}$  molar flow rate, and  $H_{3d}$ ,  $H_{3c}$  are the enthalpy of  $^3\text{He}$  in the dilute and concentrated phases at temperature  $T$ . The enthalpy of the dilute phase is larger than the concentrated phase giving cooling as  $^3\text{He}$  is transferred across the phase boundary. Accounting for the differences in the specific heat temperature dependence for the dilute and concentrated phases, the maximum cooling power in watts at the circulation rate of  $\dot{n}_3 \text{ mol s}^{-1}$  of  $^3\text{He}$  at the temperature  $T$  is given by,<sup>84</sup>

$$\dot{Q}(T) = 84\dot{n}_3T^2. \quad (4)$$

In a real system, the cooling power outside the MC available for cooling the load (SPM) is less than the maximum due to ‘losses’  $\dot{Q}_0$

$$\dot{Q}(T) = 84\dot{n}_3T^2 - \dot{Q}_0. \quad (5)$$

The losses can be represented as the sum of circulation dependent and independent terms. The former is caused by DR design features such as heat-exchanger internal surface area and super-fluid helium film suppressor efficiency. The latter is associated with the thermal resistance between the thermometer outside the MC and the liquid mixture inside of it, as well as the number of shielded wires used for thermometry, for experiments, and their proper heat anchoring, infra-red shielding and shuttering efficiency and so on. It is assumed that time-dependent losses, or heat-leaks, are already much smaller than other sources since the measurements are performed for many weeks after initial cool-down to 4 K.

## B. DR System Overview

Although dilution refrigerators have progressed to be routine operational instruments, a typical ‘standard’ DR system used ‘as is’ for SPM may result in an undesirable situation with problems caused by vacuum needs, initial cooling methods, external and intrinsic vibration noise sources during operation, as well as induced magnetism of materials near the sample space if a magnetic field is used. Early attempts to marry a basic SPM to a conventional DR typically encountered a host of insurmountable problems. To overcome these past problems we have designed a highly-specialized top-loading UHV-compatible  $^3\text{He}$ - $^4\text{He}$  dilution refrigerator,<sup>92</sup> incorporating a large-bore 15 Tesla superconducting magnet,<sup>93</sup> inside the all-metal liquid helium dewar.<sup>94</sup>

The DR itself contains an insert and a Gas Handling System (GHS). The UHV compatible insert has an Internal Vacuum Can (IVC) with a highly customized hybrid mixture condensing unit and a dilution stage inside, as well as a system of shutters, a silver SPM receptacle, wiring, and thermometry.

The GHS contains two vessels (called dumps) with  $^3\text{He}$ - $^4\text{He}$  mixture and a hermetically sealed pumping station.<sup>95</sup> As described in the previous sections, all the plumbing lines leading to pumping station are decoupled from the cryostat, as is the pipe to the 1 K pot pump. All of the pumps as well as the compressor<sup>91</sup> are placed in a service corridor outside the ULTSPM laboratory. All measuring electronics, the manual gas handling system and the control computer are located inside of a control room outside the shielded enclosures of the ULTSPM lab. All digital and analog signals enter the ULTSPM lab through filter boxes as described in Section VI.

Special attention during the design stage of the insert was paid to UHV compatibility at room and low temperature in terms of properties of materials used, ensuring a large central bore access to the magnet center, pre-cooling to 4 K method,  $^3\text{He}$ - $^4\text{He}$  condensation methods, as well as reducing overall vibrational noise during DR operation. The first demand is met by using UHV compatible materials and metal sealed flanges (CF and vacuum coupling for radiation (VCR) type) instead of indium seals commonly used in conventional DRs. Tungsten inert gas (TIG) welded or silver-brazed fittings and joints replace connections typically made with soft-solder in both the DR stage and insert. This approach results in both UHV compatibility and a more robust and sturdy DR Insert and stage, which is less prone to leaks or even bursts by accidental overpressure. 316LN, 316L and 304L austenitic stainless steels and special annealing techniques for weld seams are used near the mixing chamber (MC), magnet bore, and experimental area. Silicon bronze and beryllium copper are used for fasteners, while PEEK and polytetrafluoroethylene (PTFE) are used where plastics are needed. UHV compatible ceramic feedthroughs (D-subminiature and subminiature A (SMA)) are installed in a wiring chamber on top of the

Insert. Custom made shielded superconducting twisted pair and coaxial wires are used for both thermometry and SPM.<sup>96</sup> In the following we describe the details of the design and performance of the DR.

## C. Helium Cryostat

The cryostat belongs to the class called ‘helium vapor shielded Dewars’ where all the heat load to the cryogen is intercepted by vapor cooled radiation shields. The present design is equipped with three solid aluminum radiation shields coated with super-insulation, as well as three floating shields (Fig. 11(a)). The cryostat is supported by the 3rd stage of the three-stage vibration isolation system (Figs. 4 and 19) and is electrically isolated to form a Faraday cage with a single connection to the inner shielded experimental room (which is grounded through the instrument ground of the AML building). Despite its large stainless steel neck of 290 mm in diameter, it has a static liquid He evaporation rate of  $\approx 0.6 \text{ L hr}^{-1}$  with magnet current leads permanently installed, which increases to  $\approx 0.75 \text{ L hr}^{-1}$  when the DR operates in either of its two condensing modes. Using installed ball valves, proper vapor flow distribution is maintained among the main neck, sliding seal tube, current leads and fill-port in order to minimize the losses. The cryostat belly has a capacity of 250 L which allows for 11 days of uninterrupted SPM data taking.

The cryostat is equipped with an 89 mm (3.5 inch) bore 15 T vertical solenoid and a cancelation coil around the mixing chamber. The large bore size is dictated by the necessity to accommodate the microscope module via a top-loading port to its silver receptacle near the magnet center, as well as to accommodate a vacuum can and two infra-red radiation shields around the DR (Fig. 11). The solenoid is bottom-loaded and indium-sealed to the helium reservoir, so that it can be serviced. A stack of brass vapor-cooled magnet leads are permanently attached to the magnet and accessible on a 70 mm (2.75 inch) CF port on the top cryostat flange. Another 70 mm (2.75 inch) CF flange contains two liquid helium siphon compression fittings: one connected to a tube going to the bottom of the cryostat for nitrogen purge and initial helium filling, the other one ending inside the belly which is used for re-fills. Both of these ports include separate helium gas exhaust quick-connections that can be controlled via dedicated ball-valves.

A sliding seal on top of the cryostat allows the insert to be loaded with liquid helium inside. It contains a special PTFE-coated spring-loaded O-ring inside of an aluminum collar, forming a seal against a fiberglass tube, which is part of the DR insert. Both, collar and insert have separate helium exhaust quick-disconnects and ball valves for exhaust vapor flow regulation.

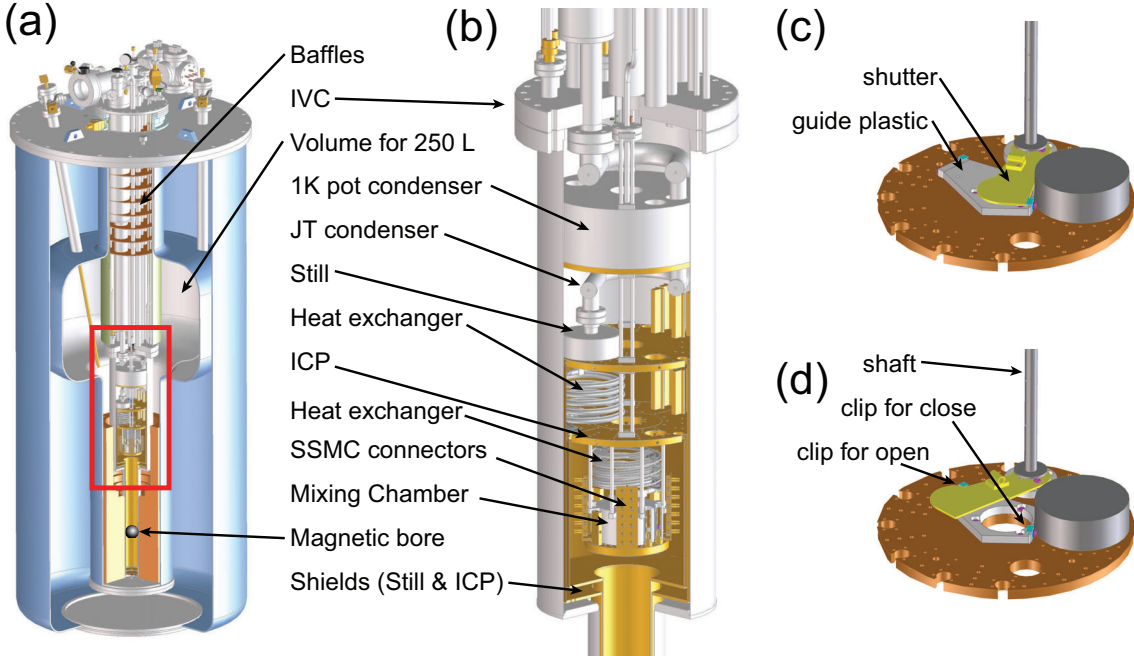


FIG. 11. 3D CAD model of the cryostat and DR insert. (a) 3D CAD model of the LHe cryostat and UHV compatible dilution refrigerator with the 15 T superconducting magnet system. (b) Magnified view of the dilution refrigerator showing the main components (red box in (a)). (c) and (d) show the closed and open position of the plate shutter on the still plate used to block thermal radiation. Similar plate shutters are located on the IVC main flange and ICP plate.

**D. UHV Compatible DR Insert**

A conceptual design of the DR is shown in Fig. 9. The insert contains a mixture condensing unit and a customized dilution refrigerator stage, surrounded by a UHV compatible internal vacuum can (IVC), as well as different pipes, baffles and wiring manifolds. All the incoming and outgoing pipes have isolation valves, so that the insert can be completely separated from the system for service or baking. The IVC is topped by a 254 mm (10 inch) copper sealed CF flange made of 316LN stainless steel. Its main body is made of 316L stainless steel, while the tail (which enters the magnet bore) is made of 321 stainless steel. The body of the IVC was annealed after welding and electro-polishing to remove stresses and magnetic-phase precipitates in the lower weld seams, while the CF flange was welded after annealing.

The condenser contains a large volume 1 K pot in parallel with a Joule-Thomson stage described further below (see Fig. 9 and Fig. 11). The pot has two filling siphons equipped with separate needle valves, one of which is under computer control via the IEEE-488 port of a stepper-motor motion controller.<sup>97</sup> Attached right below the 1 K pot (all removable, via 3.2 mm (1/8 inch) VCR fittings) are the main and JT flow impedances, the still, a spiral-in-tube continuous heat exchanger, the intermediate cold plate (ICP), four more heat exchangers, and finally the mixing chamber. The still and the first set of heat exchangers are mounted off center, while the 1 K pot, ICP,

silver heat-exchanger stack and mixing chamber have a large central bore of 38 mm inside diameter (ID) for transferring the SPM module. The still is equipped with only a passive super-fluid film flow suppressor - a sharp edge diaphragm. Although this may contribute to somewhat higher total heat loss seen by the mixing chamber in the form of incoming diluted <sup>3</sup>He-<sup>4</sup>He mixture, it eliminates acoustic noise that could be introduced by active film burners.

In order to operate the system under UHV conditions at low temperatures, the standard practice of pre-cooling the DR stage by introducing some ‘exchange gas’ into the IVC was replaced with a dedicated pre-cooling loop. If exchange gas is used in the IVC space, a multilayer He film will coat all cold surfaces due to van der Waals forces, even after pumping by external pumps to UHV pressures. The He film produces pressure bursts when running the piezo-motors used for positioning the tip and the sample in the SPM module. The combination of high voltage and the pressure burst result in arcing at the piezo motors electrodes, which burn them out. This phenomenon caused endless frustration in early cryogenic SPM instruments operating below 4 K. Therefore, a pre-cooling loop with an inlet and exhaust valves on the top of the DR insert flange was added to cool the DR. The loop starts as a standard helium transfer line receptacle in the Cryostat neck, but can be isolated with a ball-valve. It reduces to a 6.35 mm (0.25 inch) OD tube above the IVC flange, and continues as a 3.2 mm (0.125 inch) OD stainless steel

tube inside the IVC. Using Cu blocks as heat exchangers, the pre-cooling loop attaches to various stages inside the IVC: the 1 K pot, the still, the ICP, and the MC.

Pre-cooling starts first with a flow of liquid nitrogen (LN2) (if cooling from room temperature), and then with liquid helium flow for final cooling to 4 K. After cooling to 4 K the pre-cooling line is evacuated by a turbomolecular pump for a few hours, and then kept under good vacuum with a small  $40 \text{ L s}^{-1}$  ion pump situated on top of the cryostat, which runs continuously and is electrically isolated from the cryostat.

To achieve UHV conditions prior to cooling, the whole insert can be baked inside a specially designed ‘furnace’ while pumped by a turbomolecular pump placed directly on top of the insert. During bakeout the heaters are regulated to keep the MC at  $50 \text{ }^\circ\text{C}$ , and the still at  $60 \text{ }^\circ\text{C}$ , while the upper part of the insert is allowed to go up to  $125 \text{ }^\circ\text{C}$ . While the insert is baking, the mixture pumping and return lines are evacuated by a second small turbomolecular pump station, which aids in keeping the impedances and charcoal traps in the return line clean, prior to cooling.

Reducing acoustic noise is one of the most difficult problems in SPM applications, and DRs have some challenges to meet in this regard. Most DRs are very long structures with many tubes and connections that can have mechanical resonances easily excited by intrinsic or extrinsic vibrations. A known source of acoustic noise is the 1 K pot itself, where liquid helium flowing continuously through an impedance or needle valve causes resonances at audio frequencies. This has been seen in previous vibration measurements involving DRs for SPM and other applications. Although the exact mechanism of noise generation is not quite understood, there are few solutions to the problem.

The straightforward approach is to use single-shot cooling where the pot is filled and the needle valve is then closed. To accomplish this we designed our 1 K pot with a volume of  $\approx 1.5 \text{ L}$ , which results in a hold time of approximately six days while the mixture is condensed and circulated at a rate of  $100 \mu\text{mol s}^{-1}$  through the main primary impedance Z1 (Fig. 9).

In order to achieve longer measurement times, it is still desirable to have a viable continuous-cooling mode of operation. Several schemes have been tried to overcome noise problems<sup>87–89</sup> in continuously filling mode. To maximize the chances of success, our system incorporates a hybrid mixture-condensing unit with both a 1 K pot with noise reduction (using a long copper filling capillary - about 1 m - spiraled and clamped to the copper bottom of the 1 K pot) and a separate Joule-Thomson condenser. A comparison of *in-situ* vibration measurements in these two condensing modes will be described in Section VII.

## E. SPM Module Transfer and Radiation Shielding

The DR has four large access ports on the top flange: one central port with a 70 mm (2.75 inch) CF mounting flange in the center for the SPM module transfer, and three auxiliary ports with 54 mm (2.12 inch) CF flanges located symmetrically around the main center port (see Fig. 11). The central port can be closed with a UHV gate valve. Using a technique developed by one of the authors (JAS) in a custom made 4 K SPM, we transfer the whole SPM module from the (room temperature) UHV chamber above the DR to the SPM mount in the field center position, which is attached to the MC. The central 38 mm ID port, with line-of-sight through the DR, passes from the top of the DR through the IVC flange, 1 K pot, still plate, ICP, MC, and finally to the magnet region through the SPM mount, which is a support structure made from four 9.5 mm OD pure silver rods connected to the MC, as described below. Through the IVC region, the central bore has a series of plastic (PEEK) guide tubes between the 1 K pot and still, and between the still and the ICP, to guide the SPM module. After initial vibration measurements were made, (described below), a series of PEEK tubes were added to the four silver rods to stiffen the SPM mount structure (see Fig. 12). Surrounding the central port on top of the DR are three symmetrically located 25 mm ID ports which have access through to the MC. One of these ports is used for wiring, and another is used for a shutter rotation shaft with one empty auxiliary port (Figs. 11, (a) and (b)). A number of other small ports are available from the top flange into the IVC for other applications.

To reduce He consumption and to reach the lowest base temperatures, the DR incorporates three types of radiation shielding in the different regions of the insert. The three auxiliary ports around the center limit the radiation reaching the DR via shields placed in one auxiliary port, and with the material used in the other two ports (wires, and rotation shaft). Two kinds of shutter systems are incorporated to block the thermal radiation entering the central bore. First, a set of movable shutters are translated into the top section of the central port after the SPM module is locked into the DR (Fig. 5). As previously described, the tube shutters have spring-loaded side pieces which hold them inside the central tube. Typically, two shutters are used, with one placed just above the belly region of the cryostat, and the other placed in the neck region at the midpoint of the top tube. A second shutter system is used to open and close three swinging plate shutters placed at the IVC flange (4 K), the still (700 mK) and the ICP (50 mK) (Figs. 11, (c) and (d)). The swinging plate shutters are made from 3mm (0.125 inch) thick copper (gold plated) and are thermally anchored to the IVC, still, and ICP plates with copper braid and copper anchors screwed into their respective plates. The shutters are supported with a plastic (PEEK) spacer. The PEEK spacers have electrical contact sensors that detect the shutter open or closed position for computer

monitoring. The shutters are controlled by a rotating shaft that is activated using a UHV rotary feedthrough on the top flange of the DR. The series of shutters are mechanically coupled and thermally decoupled from each other using a simple mechanical design with two pins engaging two loose fitting holes of each plate.

The central DR bore continues straight through to the SPM mount, which consists of the receptacle and the locking stop ring made from pure silver (Fig. 12). The SPM mount has four pure silver rods (9.5 mm OD) connecting it to the MC. The pure silver receptacle contains 40 probe pins that make electrical connection to the removable SPM module. Just above the SPM receptacle is a pure silver cylinder that contains a stop for locking-in the SPM module. After initial vibration measurements (see Section V), the whole SPM mount structure was stiffened with PEEK tubes along the entire length. The PEEK tubes not only stiffen the structure, but also provide a convenient structure for anchoring wires and for guiding the SPM module during insertion and removal.

## F. Temperature Measurement

Temperature measurement in the DR is accomplished with three types of temperature sensors: a UHV-compatible superconducting fixed point device (FPD), a sealed UHV-compatible Cerium Magnesium Nitrate (CMN) paramagnetic susceptibility sensor, and several custom-packaged UHV compatible ruthenium oxide (RX) thin film resistors.<sup>98</sup> An absolute temperature scale is determined by the FPD and transferred to the CMN susceptibility thermometer. The CMN is then used to calibrate the RX sensors. Figure 13(a) shows the calibration data of the secondary CMN thermometer against the FPD, both attached to the MC in the field-compensated region and protected with individual Nb shields. As a first step, we calibrated the CMN thermometer by measuring the CMN mutual inductance magnetic susceptibility at each superconducting transition of the fixed point device consisting of Ir (96 mK), AuAl<sub>2</sub> (161 mK), AuIn<sub>2</sub> (208 mK), Cd (520 mK), Zn (840 mK), Al (1175 mK) and In (3300 mK). We used an LCR meter<sup>99</sup> to observe the mutual inductance of both sensors in turn, simply switching from FPD to CMN in the middle of the superconducting transition while warming very slowly. At the lowest temperatures we used 20 mV to 100 mV excitation at 100 Hz, while at higher temperatures we used 1 kHz modulation to get a better signal-to-noise ratio. These superconducting transition points are taken from the literature<sup>100,101</sup> (except Ir), and are well fit by a linear function of inverse temperature showing excellent Curie-Weiss behavior of the CMN mutual inductance, which is proportional to its paramagnetic susceptibility.

Temperatures are extracted from CMN readings using a linear fit to the CMN vs.  $T^{-1}$  data in Fig. 13(a). A linear fit to the 100 Hz, 100 mV data (the values typically used in the range of 10 mK to 100 mK) yields a

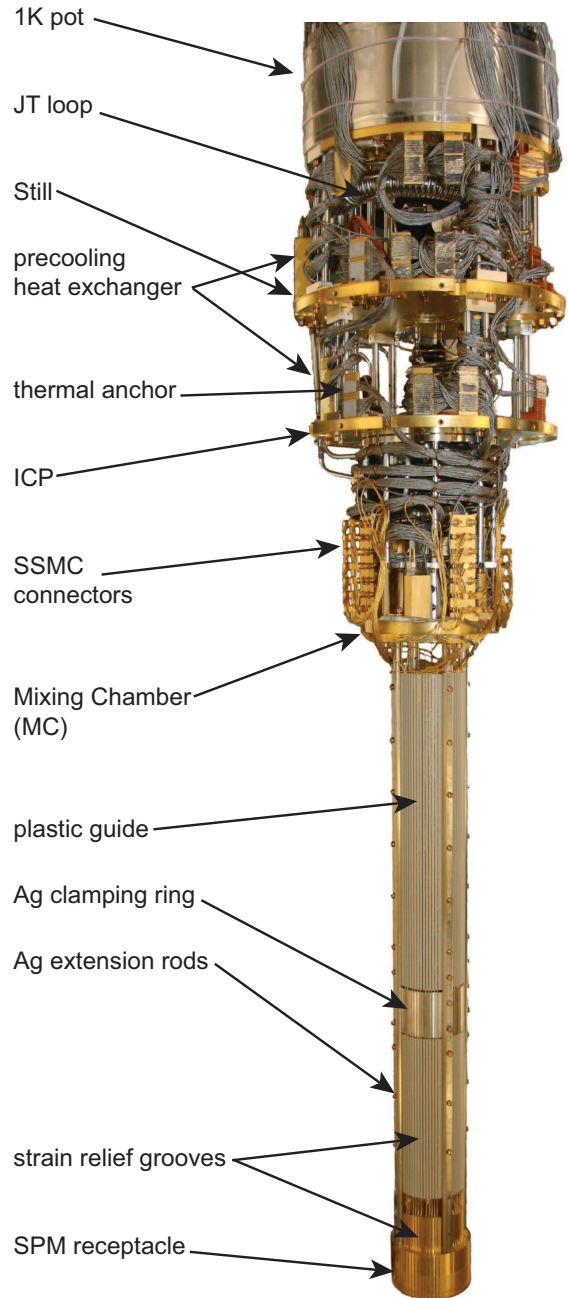


FIG. 12. A photograph of the bottom portion of the DR with the extension and receptacle for the SPM module.

slope and intercept of  $-5.1968 \pm 2.24 \times 10^{-2}$  mH mK and  $-3.4104 \pm 1.322 \times 10^{-4}$  mH, respectively (uncertainties, one standard deviation,  $1\sigma$ ). This leads to an uncertainty in temperature measurement of  $\Delta TT^{-1} = 5 \times 10^{-3}$  ( $1\sigma$ ). At  $T = 10$  mK the uncertainty is 0.05 mK and at  $T = 100$  mK the uncertainty is 0.5 mK ( $1\sigma$ ).

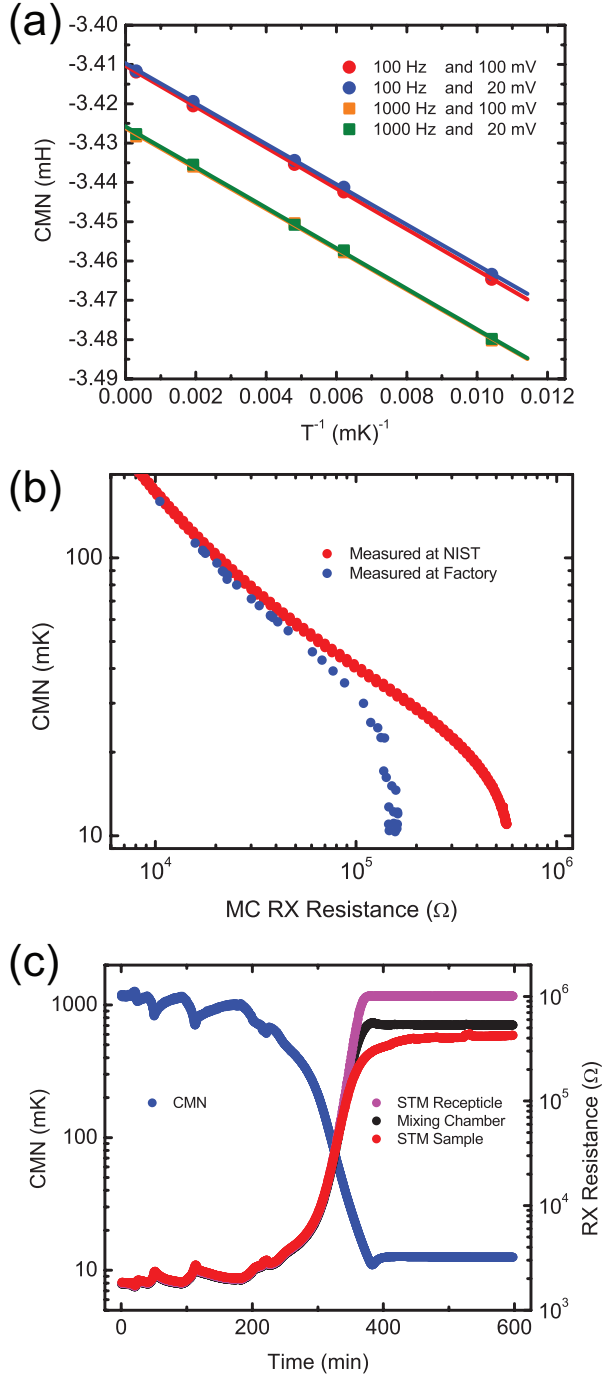


FIG. 13. Thermometry calibration and cooling measurements. (a) Susceptibility of the CMN thermometer measured at the superconducting fixed points: Ir (96 mK), AuAl<sub>2</sub> (161 mK), AuIn<sub>2</sub> (208 mK), Cd (502 mK), and In(3300 mK). The different symbols show the dependence on excitation amplitude and frequency. (b) Calibration of mixing chamber RX thermometer sensor against the CMN measured temperature. (c) CMN and RX sensor measurements during a JT condensing and cooling cycle from 4 K. The oscillations at high temperature are due to successive mixture additions and pumping cycles.

RX sensors were chosen for their relative insensitivity to magnetic fields and small variations within a manufactured batch, down to mK temperatures. Using a resistance bridge,<sup>102</sup> several custom-packaged RX sensors for UHV were calibrated against the CMN (Fig. 13(b)) and used to measure temperatures of the sample, the SPM mount, and the MC. Other, non-calibrated RX sensors were used to measure the still and ICP temperatures, using the obtained calibrations of the RX sensors on the MC as ‘generic’, which are very good for temperatures above 30 mK. The UHV RX sensors were made by attaching RX bare chips<sup>98</sup> to sapphire headers using UHV compatible non-conductive epoxy,<sup>103</sup> and attaching twisted pair leads using conductive epoxy.<sup>104</sup> The sapphire headers were then inserted into a Cu can, which was glued to a gold plated Cu bobbin. A long length of fine twisted-pair cable was wrapped around the bobbin and sealed with conductive epoxy.<sup>104</sup>

Due to the special technology used in the CMN sensor, relaxation times are rather short - about 1 min at 10 mK. It also does not show any saturation from either intrinsic (at 100 Hz) or external heat sources below 10 mK, and requires neither special electronics nor filtering techniques. This is why, at the lowest temperatures, CMN is preferred to RX or any other resistive sensors, which require hours to equilibrate and—in the absence of special filters—are very susceptible to heating from RF noise.

The effect of RF heating of the RX sensors can be seen in Fig. 13(b) in comparing measurements of the DR in unshielded space at the manufacturing factory, and then later in the shielded environment at NIST. Without sufficient RF shielding the RX sensor resistance saturates at about 150 k $\Omega$  (30 mK) due to its higher electron temperature compared to the mixing chamber temperature at 10 mK. In comparison, when measurements are made with sufficient RF shielding, we reach resistances in excess of 500 k $\Omega$ , without any signs of saturation down to 10 mK (Fig. 13(b)).

Figure 13(c) shows the CMN temperature and RX resistance during a cool down cycle from 4 K with mixture condensing using the JT mode. As shown in Fig. 13(c), measurements of the RX sensors mounted on the SPM receptacle and SPM sample platform show resistances similar to the sensor mounted on the MC (with the MC near 10 mK), attaining values in excess of 500 k $\Omega$  once equilibrium is reached. These large resistance values suggest that the temperature of the MC, SPM receptacle, and SPM sample platform all lie within a few mK of one another.

## G. DR Performance

### 1. Cooling Power Measurements

Figures 14 and 15 display the available cooling power measured as a function of temperature and mixture flow rate. These data were obtained using both condensing

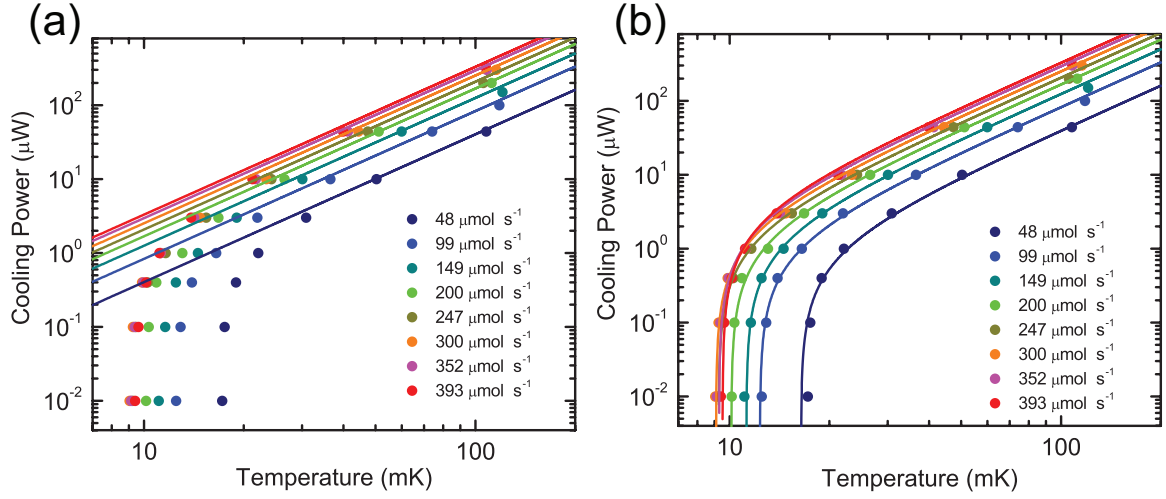


FIG. 14. DR cooling power as a function of mixing chamber temperature for different circulation flow rates using the 1K pot condenser. Cooling power is measured by applying a fixed heater power to the mixing chamber and recording the equilibrium temperature. (a) Symbols show the measured data and solid lines show the maximum cooling power predicted by Eq. 4. (b) Solid lines show the cooling power given by Eq. 5 with a  $\dot{Q}_0$  that varies as a function of circulation flow rate (see Fig. 16).

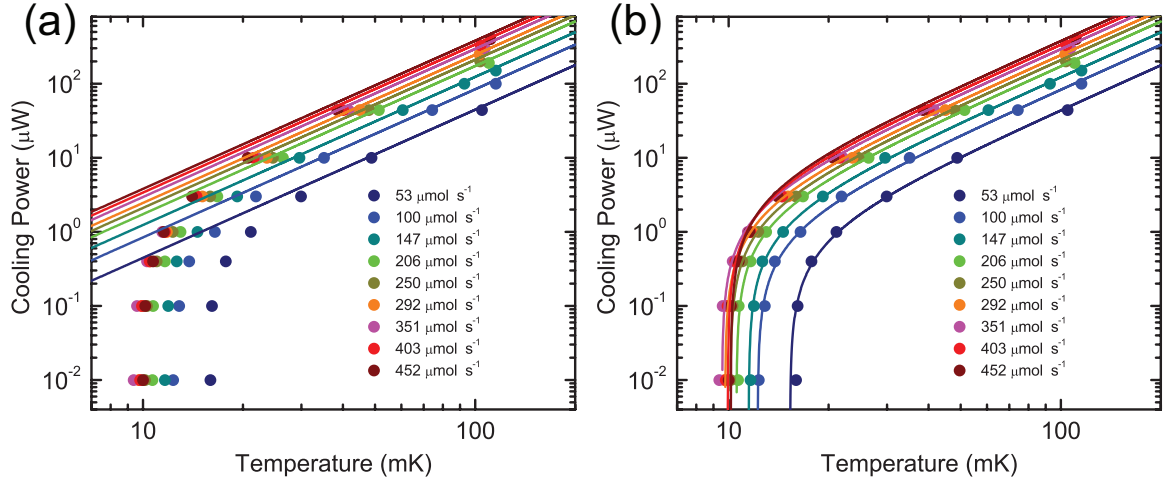


FIG. 15. DR cooling power as a function of mixing chamber temperature for different circulation flow rates using the Joule-Thomson condenser. Cooling power is measured by applying a fixed heater power to the mixing chamber and recording the equilibrium temperature. (a) Symbols show the measured data and solid lines show the maximum cooling power predicted by Eq. 4. (b) Solid lines show the cooling power given by Eq. 5 with a loss  $\dot{Q}_0$  that varies as a function of circulation flow rate (see Fig. 16).

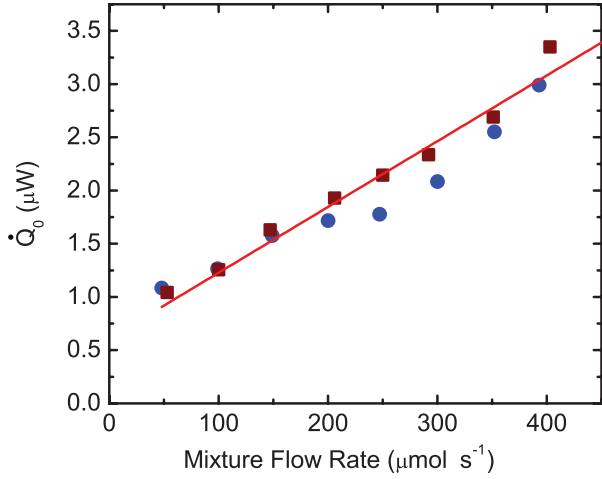


FIG. 16. The heat loss  $\dot{Q}_0$  as a function of mixture flow rate from fitting the 1K pot (blue circles) and JT (maroon squares) cooling power data in Figs. 14 and 15 to Eq. 5. The solid line is a fit to the combined data sets with a slope of  $6.2 \times 10^{-3} \mu\text{W}$  per  $\mu\text{mol s}^{-1}$  and an intercept of  $0.61 \mu\text{W}$ .

modes, 1 K pot (Fig. 14) and JT (Fig. 15), by applying DC heater power to the MC plate, while measuring its equilibrium temperature. It takes from 1 to 5 hours for the temperature to equilibrate, depending on temperature and circulation rate. As can be seen by comparing Figs. 14 and 15, both condensing modes give very similar cooling performance. A cooling power of  $\approx 350 \mu\text{W}$  at 100 mK is obtained at flow rates of  $400 \text{ mol s}^{-1}$  in either condensing mode. Below we give a simplified analysis of the data, with a few goals in mind:

1. Demonstrate that the cooling power follows a  $T^2$  asymptotic dependence at ‘high’ temperature, proving that the temperature scale devised from our calibration is correct;
2. Provide a facility user with the minimum circulation rate that should be used to attain a certain base temperature if the heat load from the SPM experiment is approximately known (minimizing the cooling power reduces potential vibrational noise from the DR);
3. Extract circulation independent losses and residual heat leaks to the MC from all sources, including manufacturer- and user- installed shielded wires, mechanical manipulators etc. in order to refine the system design.

Figures 14(a) and 15(a) show Eq. 4 overlaid with the real cooling power measurements, obtained by applying power to a  $100 \Omega$  wire-wound heater on the MC. We note that the DR, with more than 100 wires attached, three line-of-site access ports (with radiation shielding), reaches a base temperature of  $\approx 9 \text{ mK}$  at optimal circulation rate. Even at a very low flow rate of  $50 \mu\text{mol s}^{-1}$  the DR reaches a base temperature below 20 mK. Good

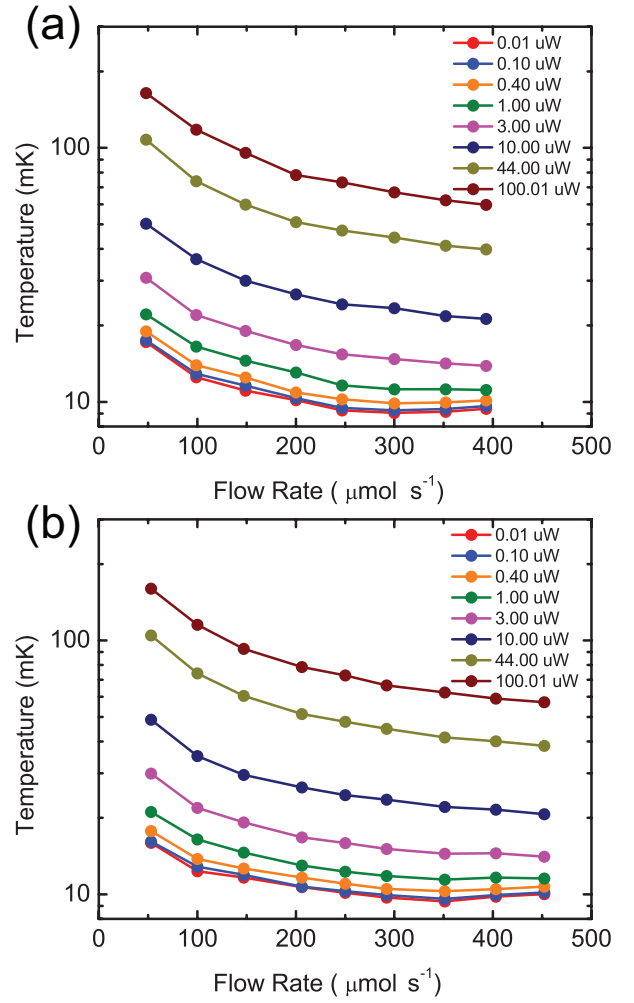


FIG. 17. Equilibrium mixing chamber temperature versus circulation flow rate for different heating powers applied to the mixing chamber for (a) the 1K pot condenser mode, and (b) the JT condenser mode. For the 1K pot mode a minimum temperature of 9.1 mK occurs at  $300 \mu\text{mol s}^{-1}$ , and for the JT mode the minimum temperature of 9.4 mK occurs at  $350 \mu\text{mol s}^{-1}$ .

agreement with Eq. 4 is observed at higher temperatures, indicating that in the region where losses are insignificant, the cooling power asymptotically approaches the maximum available by the dilution process. The measurements also show that our temperature scale, derived mostly from published data on superconducting transition temperatures, is correct.

We can fit the entire temperature dependence using Eq. 5 with a flow-rate-dependent loss term  $\dot{Q}_0$  (see Figs. 14(b) and 15(b)). The losses are less than  $1 \mu\text{W}$  at minimal flow rate, and show the expected flow dependence<sup>84</sup> (see Fig. 16). This fact gives rise to an optimal circulation rate at each heater power. Figure 17 shows the equilibrium MC temperature versus flow rate for various heater powers applied to the MC. A minimum MC temperature occurs when the sum of the heater power and

residual heat leak (constant heating) is equal to losses produced by liquid entering the MC. As the flow rate is increased to larger values, the incoming mixture heats the DR above this temperature, despite growing cooling power. At lower flow rate, constant heating overwhelms the decreasing cooling power. In the special case of zero heater power, the temperature at the minimum is called the DR ‘base’ temperature. As shown in Fig. 17 the approach to zero heater power determines the base temperature of the DR to be 9.1 mK in 1 K pot mode (at a flow rate of  $300 \mu\text{mol s}^{-1}$ ) and 9.4 mK in JT mode (at  $350 \mu\text{mol s}^{-1}$ ).

## 2. Vibration Measurements

As mentioned in the Introduction, vibrational noise issues from the DR can be the most severe detriment to SPM applications. To reduce external vibrational noise entering the DR system we used a stacked 3-stage vibration isolation system with decoupling of all the DR pump lines at each stage. This is described in detail in Section V. However, no matter how well external noise is controlled, it is the internal noise of the DR system itself that may limit the performance of the SPM. To measure the DR vibrational performance we placed two geophones<sup>105</sup> in horizontal and vertical configurations at the SPM position using the SPM mount described above (Fig. 12). All three stages of the external isolation were floated. Velocity measurements were made in both condensing modes and with mixture circulation both on and off. No corrections were made for change in geophone calibration with temperature. Initial measurements showed a large 16 Hz vibration coming from the liquid He in the cryostat. We determined that this was a pressure oscillation coming from the compartment inside the DR insert, which is isolated from the main He bath by the sliding seal surrounding the DR insert. We were able to remove this pressure oscillation by putting a large (25 mm ID) check valve on the exhaust port of the DR insert. With this check valve installed the 16 Hz oscillation is removed.

Figure 18(a) shows horizontal vibration measurements in both condensing modes with optimum flow rates and in a zero flow mode where the mixture gas is recovered in the dumps. At frequencies above 100 Hz the measurements reach the noise floor of the geophone which is  $\approx 1 \times 10^{-9} \text{ m s}^{-1} \text{ Hz}^{-1/2}$ . At lower frequency a number of horizontal modes were present, which caused some concern. We attribute the modes below 40 Hz to structural resonances in the four post SPM mount structure, which could be seen by simply tapping this structure by hand. To reduce these low frequency horizontal modes we stiffened the entire SPM mount structure with plastic PEEK tubes screwed along the four Ag posts (Fig. 12). Although velocity measurements were not made after this change, SPM measurements of the tunnel current and  $Z$ -height power spectra show no indication of these modes (see

Sections V and VII).

Resonances around 100 Hz were observed both in the horizontal (Fig. 18(a)) and vertical (Fig. 18(b)) velocity measurements. We believe these resonances may be related to possible contact between the radiation shields, which is known to be a problem in SPM applications. Measurements before and after this extensive measurement run have not shown these 100 Hz resonances again. The only changes made to the DR between measurement runs was the attachment and detachment of the still and ICP radiation shields, which leads us to believe the shields are the origin of these resonances. Significant precautions have been taken to remove any noise from the shields by using a number of guides and centering structures made from PEEK to keep the shields stationary inside the IVC.

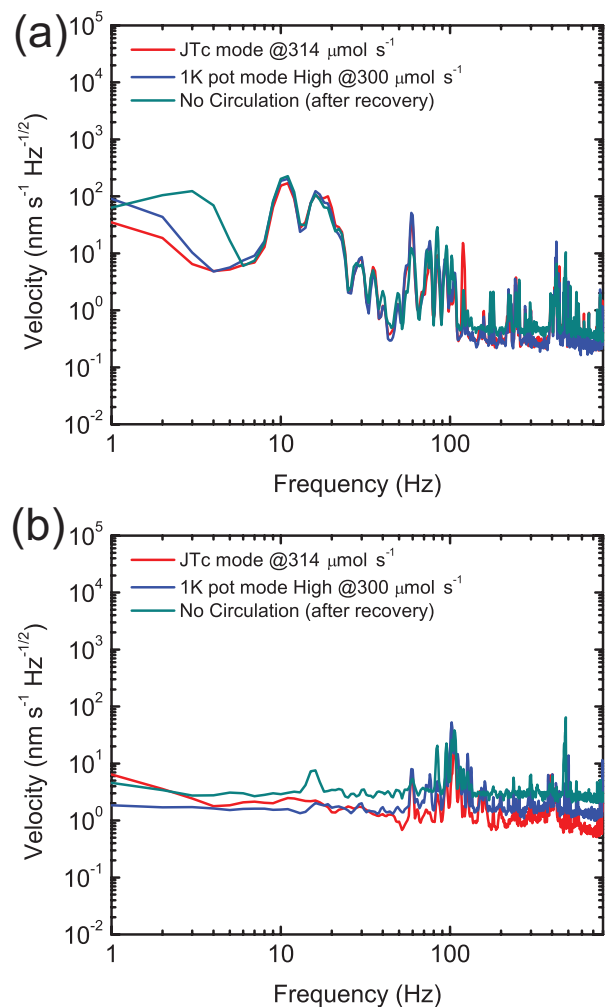


FIG. 18. Vibration spectra at the SPM stage obtained with both (a) horizontal and (b) vertical geophones. These results were measured while running the dilution refrigerator in either of two condensing modes, 1 K pot and JT, and various flow rates. A vibration spectrum without the DR mixture gas circulating (after recovering mixture into dumps) is also shown for comparison.

The most interesting observation of Fig. 18 is that the circulation of the DR even at high flow rates does not seem to alter the vibration spectra significantly. This is a significant milestone for SPM applications. In particular the vertical noise spectrum is almost at the geophone noise floor throughout the frequency measurement range except for the resonances near 100 Hz, which is not influenced much by high circulation rates in either the 1 K pot condensing mode or the JT mode. Further intensive characterization under tunneling conditions will be discussed in Section VII.

## V. VIBRATION ISOLATION

### A. Overview

A STM is extremely sensitive to vibrational noise. This is particularly true for scanning tunneling spectroscopy (STS). The tunneling current depends exponentially on the tip-sample separation, so fluctuations in tip-sample separation greatly change the tunneling current signal. With a typical vacuum tunnel barrier of 4 eV, a 0.1 nm displacement in tip-sample separation changes the tunnel current by a factor of approximately 10, and a change of even 1 pm induces a 10 % change in the tunnel current. For STS measurements, the feedback loop is open, so fluctuations in the tip-sample distance are entirely uncompensated. Therefore sub-pm stability in the tip-sample junction is required for high quality tunneling spectroscopy measurements.

In early experiments, magnetic levitation by a liquid helium-cooled superconducting structure was used for vibration isolation.<sup>45</sup> Shortly afterwards, two alternative methods emerged:<sup>106–108</sup> coil extension springs in combination with eddy current damping, and a stack of metal plates with Viton rings in-between. Both methods are effective and simple enough to be easily installed in UHV conditions in close proximity to the SPM module. However, these methods are difficult to use in combination with cryogenics and high magnetic fields. These methods of vibration isolation typically result in a dramatic loss of cooling power and base temperature, since they will also isolate the SPM system from the cryogenic system. In addition, forces induced by a magnetic field can disturb the isolation transfer function. To avoid these issues, vibration isolation stages for very low temperature SPMs are typically placed outside the active SPM module space, and the SPM module is made as rigid as possible to decrease the sensitivity to low frequency vibrations.

### B. Vibration Isolation in the NIST ULTSPM system

To achieve the very low vibrational noise levels needed for cryogenic STS measurements, multiple stages of vibration isolation are required. A single spring isolation

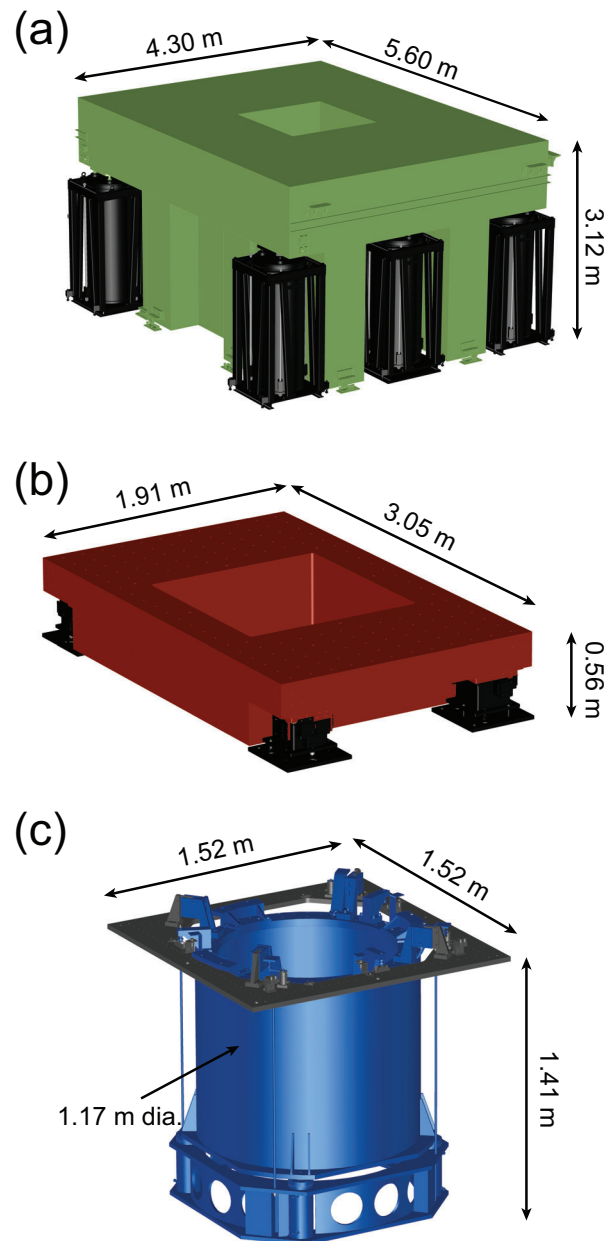


FIG. 19. 3D CAD model of the three vibration isolation stages. (a) Stage 1 (green) consists of a 110 t concrete mass with a double keel design, supported by six pneumatic air springs (black). The size of the inner hole is 1.42 m x 1.42 m. (b) Stage 2 (red) consists of a 6 t granite table supported by four pneumatic air springs (black). The size of the inner hole for the cryostat is 1.27 m x 1.27 m. (c) Stage 3 (blue) consists of an aluminum ring suspended by four stainless steel rods and containing four pneumatic air springs.

stage will isolate 40 dB per decade starting above the isolator resonance frequency.<sup>107</sup> From the author's (JAS) previous experience, an isolation level of  $\approx 100$  dB in the range of 25 Hz works well. For the ULTSPM system, a three stage design was chosen (Fig. 19) with a design isolation level of 100 dB at 25 Hz.

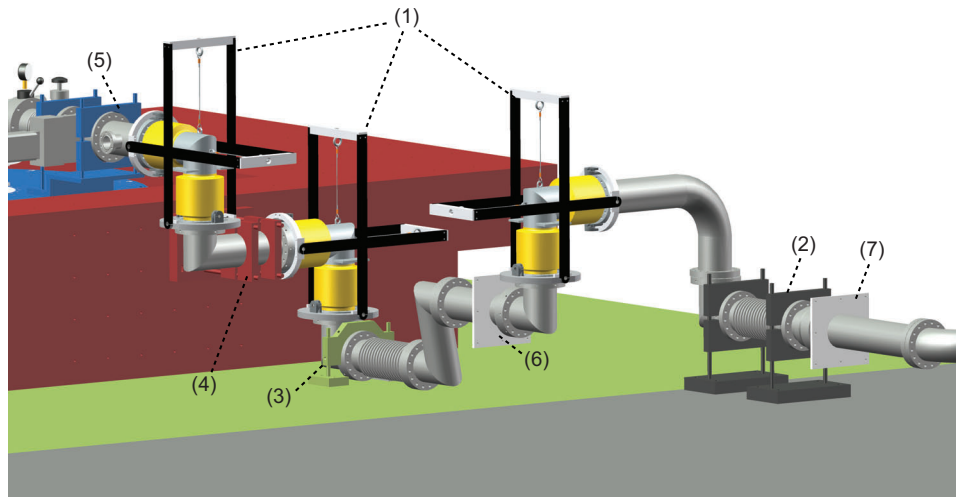


FIG. 20. 3D CAD model of the  $^3\text{He}$ - $^4\text{He}$  mixture recovery pumping line. Three gimbal systems<sup>86</sup> (1) decouple the recovery pumping line at each vibration isolation stage from the SPM system. In between the gimbal systems, the pumping line is rigidly anchored to the building ((2), grey), the first vibration isolation stage ((3), green), the second stage ((4), red) and the third stage ((5), blue). At (6) the line passes through (and anchors to) the wall of the inner shielded room, and at (7) it passes through (and anchors to) the outer shielded room.

The ULTSPM system is located in the NIST AML building, which was specially designed for low vibration levels.<sup>43</sup> The lab is located 13 m below ground level and special attention was given to isolating the building foundations, lab enclosures, and utilities from the experimental spaces. In particular, the AML incorporates specially designed floating floors using large inertial masses supported by pneumatic isolators. Such a system comprises the first stage of isolation of our instrument. The three different stages of the vibration isolation system are shown in Figs. 4 and 19: colored green (stage 1), red (stage 2) and blue (stage 3). Stage 1 (Fig. 19(a)) is the NIST AML  $\approx 110$  t inertial mass (floating floor), a stiff double keel design with a high resonance frequency of  $\approx 100$  Hz. The large mass is supported by six pneumatic isolators, each rated for 20 t. Stage 1 has a natural frequency of 0.75 Hz.<sup>109</sup> Stage 2 (Fig. 19(b)) consists of a  $\approx 6$  t granite table with four pneumatic isolators (natural resonance 2.5 Hz).<sup>110</sup> Active cancellation of vibrations is available for both Stage 1 and Stage 2 via two independent feedback loops, each controlling six degrees of freedom over a 20 Hz bandwidth. Stage 3 (Fig. 19(c)) consists of custom designed aluminum structure (dark blue in Fig. 4) incorporating four pneumatic isolators (natural resonance 1.5 Hz),<sup>111</sup> on a ring that is supported by 4 stainless-steel rods hanging from a steel plate (gray in Fig. 19(c)) fixed to the top of the granite table. The cryostat bolts to the top of the aluminum cylinder which floats on the isolators in the lower structure containing the pneumatic isolators. The 3rd stage is damped by eddy current dampers. To minimize vibration coupling between the stages, the mass of each con-

secutive stage is an order of magnitude lower than the previous stage. All three stages are electronically controlled through control units, electro-pneumatic valves, and a software system.<sup>111</sup>

Even though the 3-stage isolation system isolates the SPM from floor vibrations, vibrational noise can still affect the system through acoustic vibrations. To minimize acoustic noise an inner acoustic room ((9) in Fig. 4) is built on top of the stage 1 floating mass. This room also comprises an RF shield around the SPM system (see Section VI, Electronics). A second acoustic enclosure surrounds stage 1 and the inner shielded room ((10) in Fig. 4) to reduce acoustic noise still further. A control system allows air flow to the inner shielded room to be shut off during SPM measurements to reduce air fluctuations inside the acoustic enclosure. As described earlier, both shielded rooms have small hatches to allow the UHV coupling of the ULTSPM lab to the adjoining processing lab (Fig. 4).

In isolating the system from external disturbances, care must be taken to eliminate hard connections to the system that would ‘short out’ the isolation measures. A DR uses a closed loop gas circulation system, and a careful design must be made for decoupling the large mechanical pump lines that connect the circulation pumps to the DR. In our system, all pumps are located outside the shielded rooms in an adjoining service corridor. All pumping lines pass through a concrete block located in the service corridor, and are attached rigidly to the walls of the shielded rooms. To alleviate the shorting of the vibration isolation system by the pump lines, there are three sets of custom-made bellows incorporating gimbals

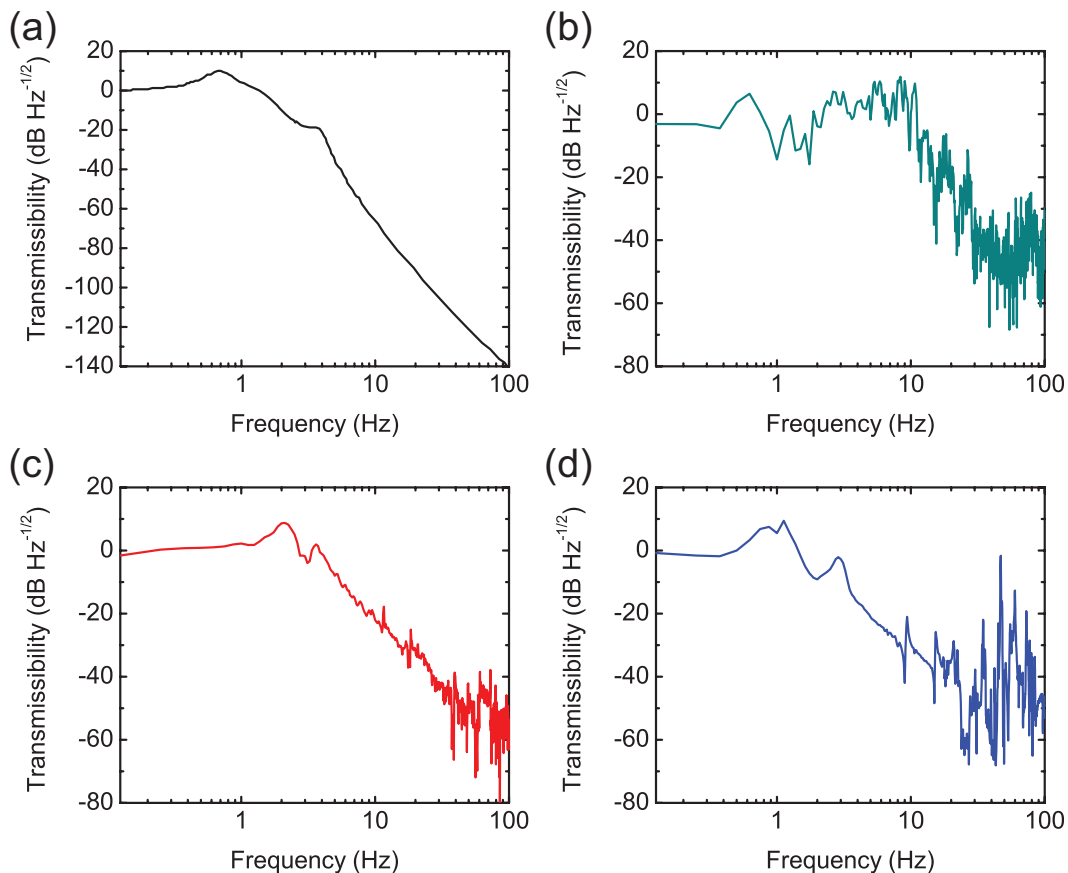


FIG. 21. Vibration transmission spectra of the 3-stage isolation system in Figs. 4 and 19. (a) Theoretical transmission spectrum for the combined 3-stage isolation system. (b-d) Transmission spectra measured between (b) floor and stage 1, (c) stage 1 and stage 2, and (d) stage 2 and stage 3.

to isolate the large mixture recovery pumping line between each of the vibration stages (Fig. 20).<sup>75</sup> A similar system, but smaller, is used for the pumping line to the 1 K pot. With these decoupling systems, we detect no effect from the DR pumping units in the SPM measurements.

### C. Vibration Isolation System Performance

The performance of the various vibration isolation stages was characterized by measuring the vertical vibration levels of the various stages using accelerometers<sup>112</sup> placed on each stage. The resulting vibration levels are sufficiently low that measuring them can be difficult. The overall design transfer function (Fig. 21(a)) of the whole system across the three stages is impossible to measure because of the low amplitude levels. Therefore, the transfer function of each stage was measured separately. To obtain better coherence in the measurements, stage 1 and 2 were excited under software control to measure the transfer functions of stage 1 to 2, and 2 to 3 respectively. Figures 21, (b)-(d) summarize these measurements. In the stage 1 transfer function (Fig. 21(b)), the isolator res-

onance is observed at 0.6 Hz. However, in contrast to initial design goals the effective isolation does not start until  $\approx 10$  Hz. We attribute this lack of performance in stage 1 to acoustic coupling of air fluctuations to the shielded room mounted on stage 1, which has a large cross section for air pressure fluctuations. This was verified with correlation measurements between pressure fluctuations and vibration levels on the shielded room.

The transfer function for stage 2 (Fig. 21(c)) shows the isolator resonance at 2.1 Hz, with an isolation of 40 dB per decade. A second resonance at 3.6 Hz is also observed due to the excitation of the stage 3 isolators. Finally, the transfer function for stage 3 is shown in Fig. 21(d). Stage 3 shows an isolator resonance at 3 Hz. About 40 dB of isolation is observed at 20 Hz. However, structural resonances of the stage 3 ring (Fig. 21(c)) are observed above 20 Hz, which were confirmed by a finite element analysis (FEA) of the stage 3 structure. To see how these resonances affect the SPM measurements we examine the residual vibration levels and the noise spectrum of the SPM signals.

The overall attenuation of the three stages from the transfer function measurements indicate vibration attenuation greater than 100 dB at 25 Hz, which was the de-

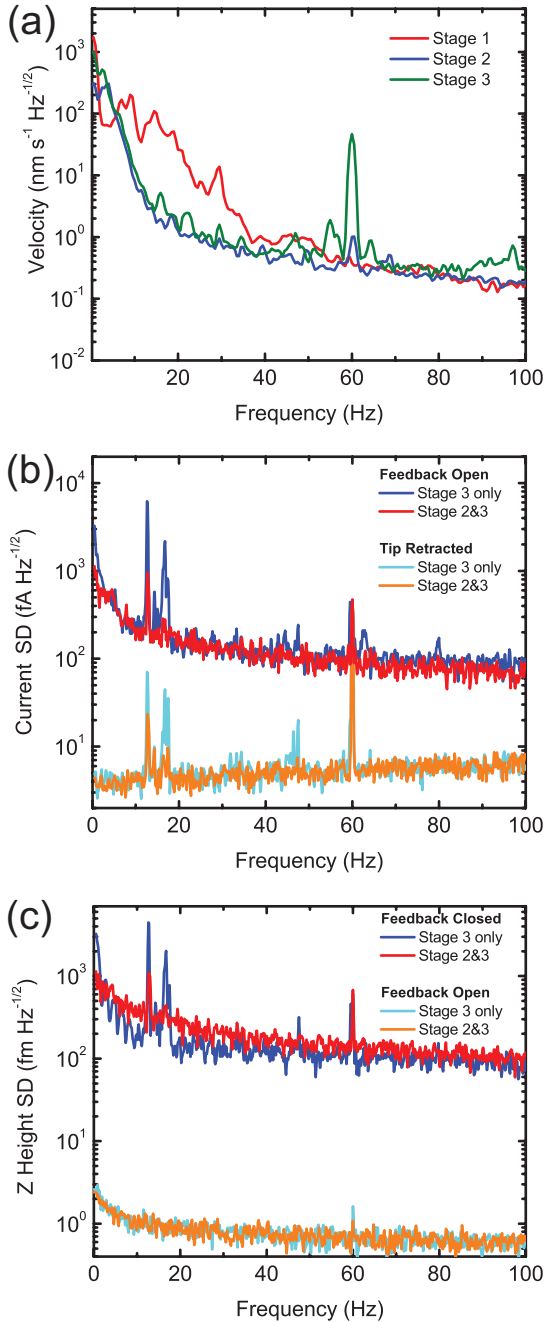


FIG. 22. Characteristics of the 3-stage vibration isolation system. (a) Spectral density (SD) measurements of the velocity vs. frequency of stage 1 (red), 2 (blue), and 3 (green) with all stages floating. Velocity spectra were measured with an accelerometer<sup>112</sup> in velocity mode. SD measurements of (b) the tunneling current and (c) the Z-height signal vs. frequency with stage 3 only or stage 2 and stage 3 floating. These measurement was performed on a Ag(111) sample with a W tip by using the external preamplifier<sup>113</sup> and a spectrum analyzer<sup>114</sup>. Tunneling parameters: tunneling current set-point 100 pA, sample bias 2.0 V. DR parameters: 100  $\mu\text{mol s}^{-1}$  in JT mode,  $T=13$  mK.

sign goal. The residual vibration levels of the three stages

for the frequency up to 100 Hz are shown in Fig. 22(a). The vibration levels are the largest for stage 1, as expected. For stage 2 and stage 3, the vibration levels are similar and very low, below  $1 \text{ nm s}^{-1} \text{ Hz}^{-1/2}$  above 20 Hz, as they approach the noise limit of the sensor used. Stage 3 exhibits some peaks near 60 Hz, which are due to the structural resonances observed in the transfer function measurements, and corresponds to the lowest frequency mode seen in the FEA.

The final determination of the isolation performance is obtained by measuring directly the spectral density (SD) of the tunneling current and Z-height signals. In Fig. 22(b) the ‘feedback open’ curves show the tunnel current fluctuations with the SPM tip-sample separation held constant, as for STS; in this mode the tunnel current is sensitive to any tip-sample relative motion. The measurements without tunneling (tip retracted from the sample) show the background noise of the external current preamplifier (see Section VII). The current signals are relatively small - below  $100 \text{ fA Hz}^{-1/2}$  - indicating a very good performance of the system. Measurements are shown for two different configurations of the vibration system, with stage 3 alone floating, and stages 2 and 3 both floating together. As seen in Fig. 22(b), low frequency noise features are significantly enhanced between 10 Hz and 20 Hz if only stage 3 isolation is used. Figure 22(c) confirms these findings in the Z-height SD. With the SPM feedback closed, tip-sample fluctuations are seen in the Z-channel, as feedback moves the tip to keep the tunnel current constant. The feedback open curves in Fig. 22(c) show the noise level of the electronics controlling the Z-height. Similar to observations of the current SD an increase in Z-height SD is observed in the low frequency region with only stage 3 floating. With the two stages both floating, the largest feature observed in the Z-height SD occurs at 60 Hz. The 60 Hz peak is due to pickup of electrical power line noise in the electrical cables. With both stages floating, the spectral density of the Z-height signal (Fig. 22(c)) is below  $1 \text{ pm Hz}^{-1/2}$  for all measured frequencies, and approaches  $100 \text{ fm Hz}^{-1/2}$  at 100 Hz, which allows a good signal to noise ratio in STS measurements (Section VII).

## VI. ELECTRONICS

### A. Overview

The two main operating modes of STM are topographic imaging and spectroscopy. Both of these measurements require sourcing signals over large voltage ranges with little noise, while measuring small signals. To obtain good results, careful attention to electrical noise and signal acquisition are needed. After vibrational noise issues have been dealt with, electrical noise quickly becomes the primary performance-limiting factor of the instrument. For topographic imaging there are two modes of measurement, constant current and constant height,

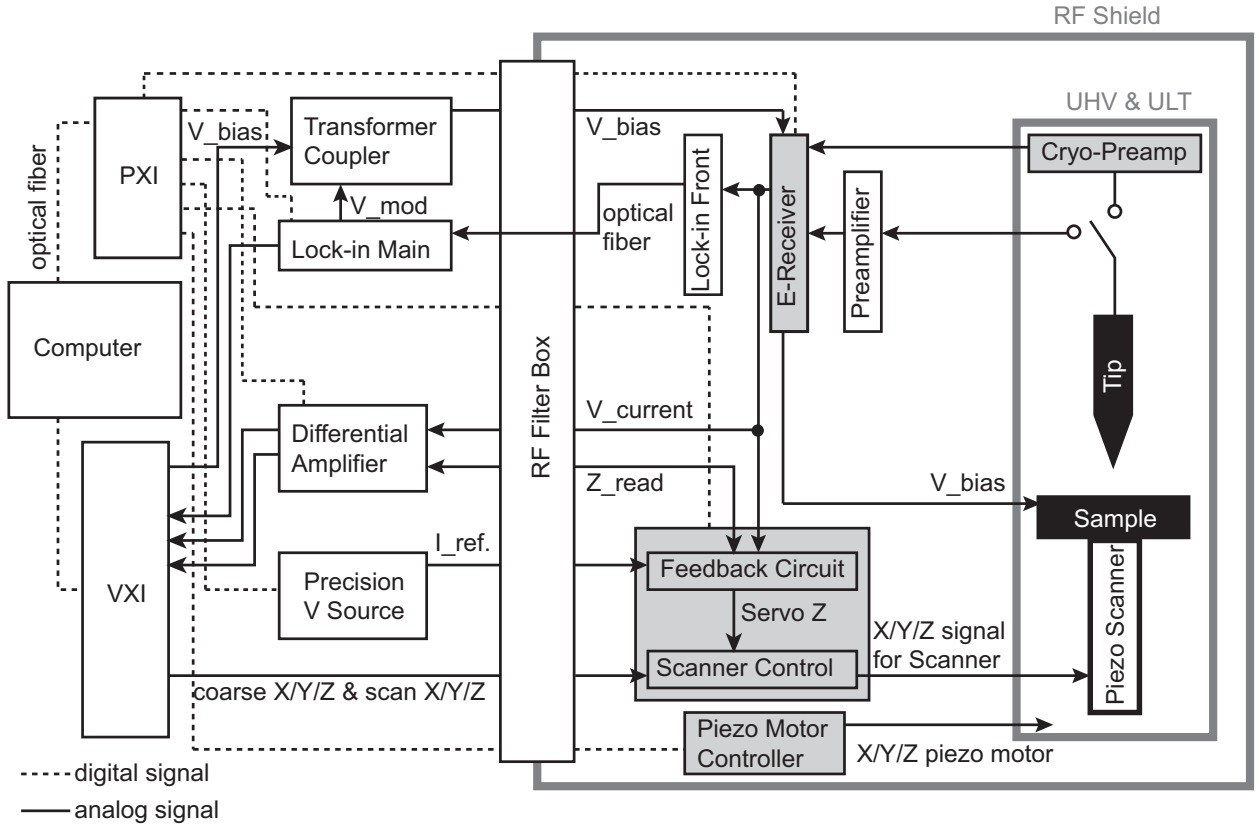


FIG. 23. Block diagram showing the analog (solid line) and digital (dotted line) signal connections and the electronics for the ULTSPM system. The light gray colored boxes are NIST-built electronics. A feedback circuit and a scan controller are integrated into a single servo box. Thick gray outlines indicate the RF shielded room and the UHV part of the dilution refrigerator (SPM module inside). All of the signal cables (except for an optical fiber connected to a precision lock-in amplifier) pass through RF filters, which are fixed to the wall of the RF shielded room.

which are distinguished by whether the feedback loop is active or not. In constant height mode, there is no active feedback loop and the variations in the tunneling current are recorded as the tip is raster scanned. The bandwidth of this mode can be very high since there are no feedback loop stability limitations. This mode, however, can only be used on extremely flat surfaces, since there is no feedback to pull the tip away from obstacles.

Constant current imaging is the more traditional topographic mode, where a feedback loop is used to keep the tunneling current constant as the tip is raster scanned over the sample surface. In this mode, the  $Z$ -error signal is applied to the  $Z$ -scanning piezo to keep the tunnel current constant. The  $Z$ -error signal is recorded as the topographic image. This method can be used to image surfaces with substantial height variations limited only by the range of the  $Z$ -axis piezoelectric scanner. Very critical is the design of the feedback loop controller, which must have good stability and noise characteristics. Since the beginning of STM, a number of feedback circuits have been developed for this reason.<sup>19,107,115</sup>

At cryogenic temperatures, spectroscopy measurements are the more sought-after measurements for elucidating physics of interest. In spectroscopy mode, the

feedback loop is opened at each point of interest. The tunneling current or its derivative (via a lock-in amplifier) is measured while the sample bias voltage is varied. Since the tunneling current depends exponentially on the tip-sample separation, tunneling spectroscopy requires that a well defined and stable gap distance between the two electrodes is maintained. As in topographic mode, the feedback loop electronics will affect the performance in spectroscopic modes. For example, when the feedback loop is switched open, care must be taken to avoid any disturbance to the  $Z$ -piezo voltage, which would change the tip-sample distance. Spectroscopy measurements are also very dependent on the overall performance of the current preamplifier. A wide variety of current gains and bandwidths are used depending on the particular application. For atom manipulation, a gain of  $10^7 \text{ V A}^{-1}$  may be used, while tunneling on thin insulators may require a gain of  $10^{10} \text{ V A}^{-1}$  to obtain very low tunneling currents. In this section we describe the electronics used in our ULTSPM system (Fig. 23).

## B. Control Electronics

The ULTSPM controlling electronics utilizes Versa Module Eurocard (VME), VME eXtension for Instrumentation (VXI) and the newer Peripheral Component Interconnect (PCI) eXtension for Instrumentation (PXI) mainframes which contain a variety of source and measurement instruments and digital communication. These mainframes are controlled by a Linux computer operating custom developed SPM software. Following these mainframes, a variety of custom designed and fabricated low-noise electronics serve to control the SPM. As shown in Fig. 23, a coupling transformer<sup>116</sup> is used to add a small modulation voltage from the lock-in,<sup>117</sup> to the DC sample bias voltage. This passive coupling is preferred to a summing amplifier, in order to minimize electronic noise and to avoid any grounding problems. The sample bias voltage then goes to a custom E-receiver module located close to the cryostat that has a differential receiver with software selectable attenuation and low pass filters. A number of 20 bit VXI arbitrary waveform generators<sup>118</sup> are used to generate the XYZ raster signals, which go to the scanner control unit located near the cryostat. These signals are received differentially and amplified using precision high voltage op-amps.<sup>119</sup> The feedback loop circuit is located on the same circuit board as the scanner electronics and includes a precision rectifier, logarithmic amplifier, and proportional gain control. We call the combination of feedback and scanner electronics the ‘SPM servo’. A number of novel features are included in the servo design, including a sample and hold input to avoid any fluctuations in the output during spectroscopy, software adjustable gains on the XYZ raster signals, which depend on scanning size, as well as other details. Careful attention is paid to grounding, and all signals are received with differential amplifiers to further reduce grounding issues. All metal connections to the cryostat system are broken with ceramic breaks, and only one ground connection is made to the building instrument-ground system. We use a commercial current preamp<sup>113</sup> that is closely coupled to the E-receiver module. All signals (including the high current magnetic leads) pass through RF filters located on the back wall of the shielded room (Fig. 23).

Another central piece of electronics is the piezo-motor controller which generates the high voltage waveforms that drive the coarse motion of  $Z$ -piezo motor, and  $XY$  piezo motors. A typical problem in cryogenic SPM is that the coarse piezo motors work at room temperature but fail to work at cryogenic temperatures. This is due to the piezo gain coefficient dropping by a factor of 4 to 5 in cooling from 300 K to 4 K or lower. To overcome the drop in gain, we use a stack of 4 shear piezos, and use high voltage amplitudes up to 600 V with a very fast slew rate. The latter is especially important to induce the shear piezo to slip against the sapphire prism or plate without moving it. Figure 24 shows a simplified circuit diagram of the piezo motor controller. A 12-bit waveform generated by a PXI analog output module<sup>120</sup> is amplified

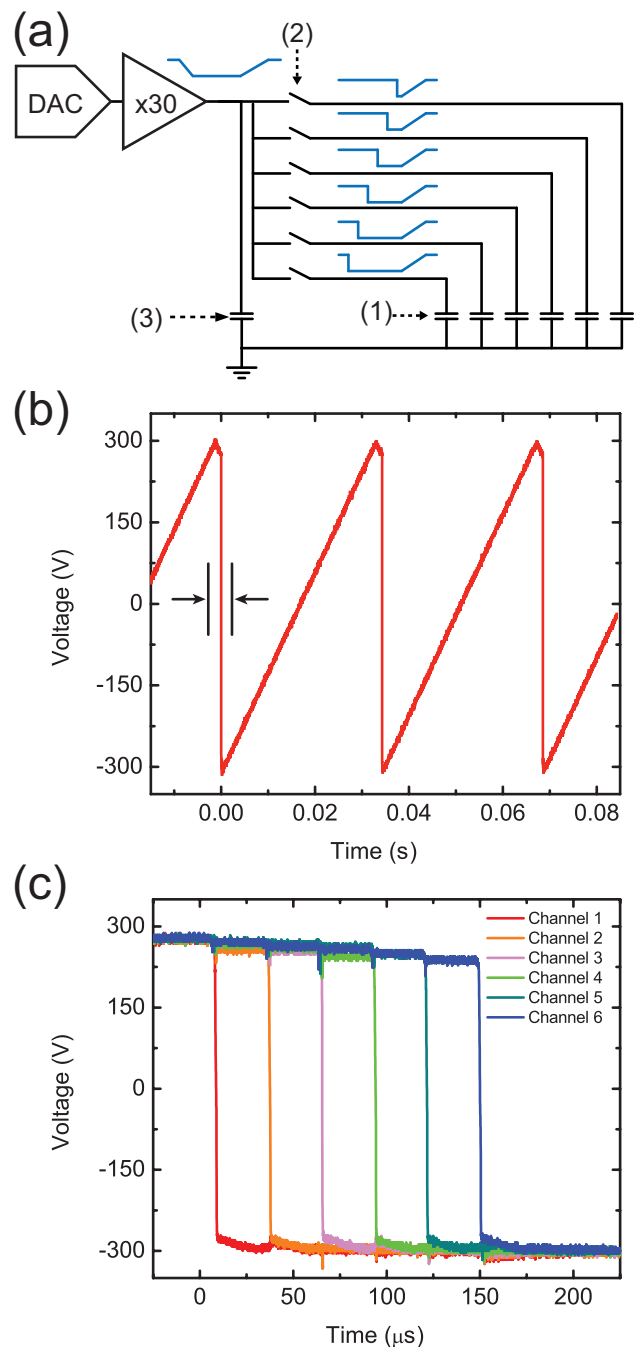


FIG. 24. Piezo-motor drive circuitry and performance measurements. (a) Drive signals originating from the DAC are amplified  $\times 30$  and sent to the six 2.5 nF piezo stacks in the SPM module (1), via six independently fired Triac switches (2). The switches are timed by a digital clock, and sequentially-fired. An additional 100 nF capacitance (3) acts as a charge reservoir to allow quick piezo charging. (b) Full amplitude output signal driving a piezo capacitance load. (c) Expanded time scale for all six transition signals (slip mode) driving a piezo capacitance load. The time delay between each signal is  $\approx 28 \mu\text{s}$ , and the transition time from 90 % to 10 % of the signal height is  $\approx 872 \text{ ns}$ .

to high voltage.<sup>121</sup> The fast slip transients are generated by using a series of Triac switches. Each *XYZ* piezomotor has a separate amplifier stage and six associated Triac switches. The six Triac switches are fired in succession with  $\approx 28 \mu\text{s}$  delay between transitions. The Triacs, and associated good design, deliver a voltage step of 600 V in a transition time of less than 1  $\mu\text{s}$  (Figs. 24, (b) and (c)). The resulting motion of the piezo motors was discussed and shown previously in Fig. 7.

### C. Cabling and Cryogenic Preamplifier

One of the difficulties in cryogenic SPM instruments is dealing with the long cable distances between the SPM unit and the outside electronics. In particular, this can be deleterious to low current measurements, as the cable capacitance will add noise to the measurement. In our system we used cables made from superconducting CuNi clad NbTi cores,<sup>96</sup> surrounded by Teflon and stainless steel braided shielding. We use these cables both in a shielded twisted pair configuration, and in single coax geometries. Approximately 100 cables are used for the SPM and thermometry signals. The overall length of these cables from the top of the DR to the SSMC connectors on the MC is 6.7 m. From the MC another length (about 1 m) of coaxial cables (miniature coax consisting of Cu cores, Teflon insulation, gold plated Cu shield) connect to the SPM receptacle (Fig. 12), yielding a total

cable length close to 10 m. At room temperature, typical cable resistance and capacitance values are  $\approx 300 \Omega$  and  $\approx 500 \text{ pF}$ , respectively. This much cable capacitance is expected to limit the frequency response and noise characteristics of a low current measurement with a preamplifier located outside of the cryostat, as indicated in Figs. 25, (a) and (b). On the other hand, the combined resistance and capacitance aids in providing additional distributed RF filtering to the cryogenic section. To overcome the limitation of added capacitance in the tunnel current measurements, we designed a cryogenic current preamplifier.

In a scanning tunneling microscope, one typically measures tunneling currents in the range of 1 pA to 100 nA. The most widely used scanning (line) speeds are 1 Hz to 20 Hz in topographic mode. Some groups use a homemade current amplifier but most groups use commercial preamplifiers with a gain of  $10^8$  or  $10^9$ , as shown in Fig. 25(a). With these gains, these amplifiers have a dynamic range of  $\approx 10^3$  Hz determined by the corner frequency  $(2\pi R_f C_p)^{-1}$  in a simplified equivalent circuit (Fig. 25(b)), and they perform nicely in a topographic mode as long as the feedback loop gain is large enough. For scanning tunneling spectroscopy, a dither signal of 500 Hz to 2 kHz is added to the DC tunneling bias and the first derivative of the tunneling signal,  $dI/dV$ , is measured by a lock-in amplifier. The total spectral noise density in a current preamplifier with large stray capacitance can be written as,<sup>124</sup>

$$e_{TSN} \simeq \sqrt{i_n^2 R_f^2 + 4k_B T R_f + \left[1 + \left(\frac{C_D}{C_P}\right)\right]^2} e_n^2 \quad \omega \gg \frac{1}{R_f C_P}, \quad C_D \gg C_P \quad (6)$$

where  $e_n$  is the input voltage noise,  $i_n$  the input current noise,  $R_f$  the feedback resistance, and  $C_D$  the parasitic capacitance from the connection wiring. The term  $\sqrt{4k_B T R_f}$  is the temperature-dependent Johnson noise density, and can be reduced to a negligible value when the feedback resistor is kept at cryogenic temperature. The frequency dependence of the preamplifier gain and noise sources are shown schematically in Fig. 25(b). When the preamplifier is close to the sample-tip junction,  $C_D$  is smaller than 1 pF. However, for long cables, the capacitance may grow to several hundreds pF, which substantially increases the noise contribution from  $C_D$ . The noise gain is higher in the frequency range between  $(2\pi R_f C_p)^{-1}$  and  $(C_p/C_D)f_c$ , where  $f_c$  is the corner frequency of the open loop preamplifier gain. As  $C_D$  increases, the range exactly overlaps with the typical dither frequencies used in STS operation.

In order to reduce the noise due to cable capacitance, one can devise a circuit in which the feedback resistor<sup>34</sup> and the front mirror-stage amplifier can be kept at a

cryogenic temperature.

Figures 25, (c) and (d) show circuit diagrams of cryogenic preamplifiers that utilize this concept. In Fig 25(c), a *p*-channel enhanced metal oxide semiconductor field effect transistor (MOSFET)<sup>125</sup> is used since a minority carrier device does not operate at cryogenic temperature. This circuit operates well at room temperature, but when it is cooled down below liquid helium temperature, the threshold voltages in transistor 1 and transistor 2 can be quite different, which affects the tunneling bias voltage. An external bias of typically 0 V to 1 V has to be added to the sample bias to compensate for the tip voltage developed from the transistor mismatch, and this causes an unwanted shift of the zero-voltage point in the STS measurement. A III-V MOSFET<sup>126</sup> would be preferable, but it is not commercially available at present. Instead, one can use GaAs junction field-effect transistors (JFETs)<sup>127</sup> or GaAs metal semiconductor field-effect transistors (MESFETs).<sup>128</sup>

Figure 25(d) shows a similar circuit diagram using a

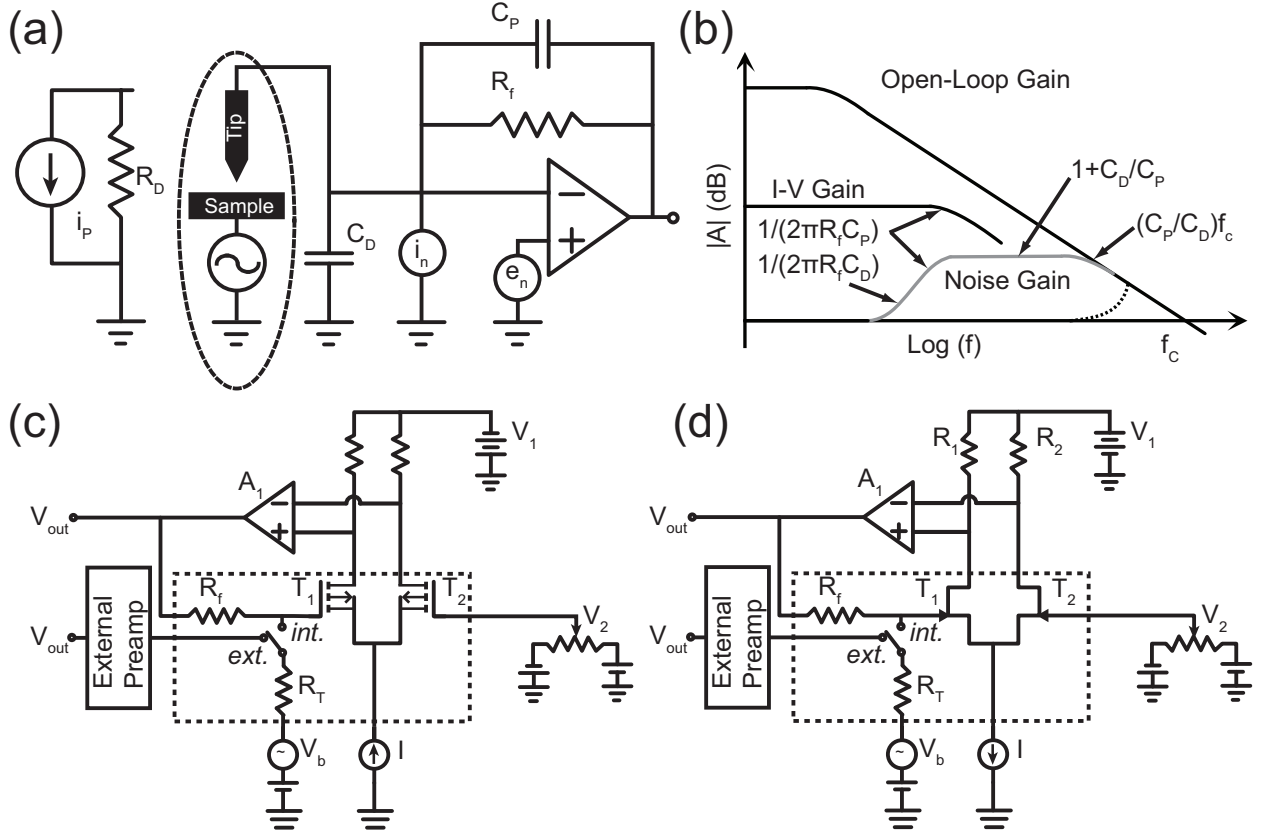


FIG. 25. Cryogenic current preamplifier concepts and schematics. (a) Schematic diagram of an STM tunneling unit and preamplifier.  $C_D$  stands for a stray capacitance coming from signal wiring inside the STM chamber to the external preamplifier. Symbols  $i_n$  and  $e_n$  are the input current and voltage noise of the preamplifier. The tunneling junction (a dotted oval) can be expressed with an equivalent circuit diagram (left-most diagram). (b) The frequency response of the preamplifier and noise. (c) A preamplifier circuit diagram using a pair of silicon  $p$ -channel MOSFETs, where parts inside the dotted region are at cryogenic temperature. As indicated in the text the  $p$ -channel silicon MOS devices were replaced by GaAs devices shown in (d). (d) A preamplifier circuit diagram using a pair GaAs MESFETs, where parts inside the dotted region are attached to the still plate in the DR ( $\approx 700$  mK).  $R_1$  and  $R_2$  are ordinarily  $10^5 \Omega$  to  $10^6 \Omega$ .  $T_1$  and  $T_2$  are  $n$ -channel dual gate transistors<sup>122</sup> and  $A_1$  is an operational amplifier<sup>123</sup>. The symbol  $I$  stands for a constant-current source, whose value can be determined by the operating point of the transistor ( $-5 \mu\text{A}$  to  $-200 \mu\text{A}$ ) in the present circuit.  $R_f$  and  $V_2$  are the feedback resistor ( $10^7$ ,  $10^8$ , or  $10^9$ ) and the bias voltage, respectively. A relay is used to switch between an external preamplifier and this internal preamplifier.

MESFET, which we implemented for our system. A MESFET often reveals a large leakage current ( $10^{-13}$  A) and random telegraph noise if the transistor is not cooled down properly. One has to match the MESFETs through trial and error, requiring testing many samples (and rapid cool down is not recommended). The payoff is that bias adjustment between two MESFETs is no longer required. We mounted the circuit outlined by the dotted line in Fig. 25(d) onto the still plate, with the rest of the circuit at room temperature inside the E-receiver (Fig. 23). The cryogenic circuit includes relays to switch between the internal preamp and the external preamp, as well as switching between three different gain values of ( $10^7$ ,  $10^8$ , and  $10^9$ )  $\text{V A}^{-1}$ . A 2nd identical internal preamp is located on the still for use in AFM measurements using quartz tuning fork sensors. No change in DR operation was observed when operating the internal preamps, and the tip voltage offset due to transistor mis-

match was less than 5 mV at 10 mK, which can be easily compensated by a constant offset to the sample bias voltage (done in the software). In the following section we describe the performance of this cryogenic amplifier and the overall system.

## VII. PERFORMANCE

### A. Overview

In this section we detail a number of measurements that describe the performance of the NIST ULTSPM system. These include measurements examining the effects of piezo walker motion on sample temperature, determining the influence of magnetic field ramping on the tunnel junction, comparing the cryogenic preamplifier to an ex-

ternal preamplifier, and comparing current and  $Z$ -height power spectra for different condensing modes of the DR. Finally, we present initial STM and STS measurements of  $\text{Cu}_2\text{N}$  and graphene grown on SiC.

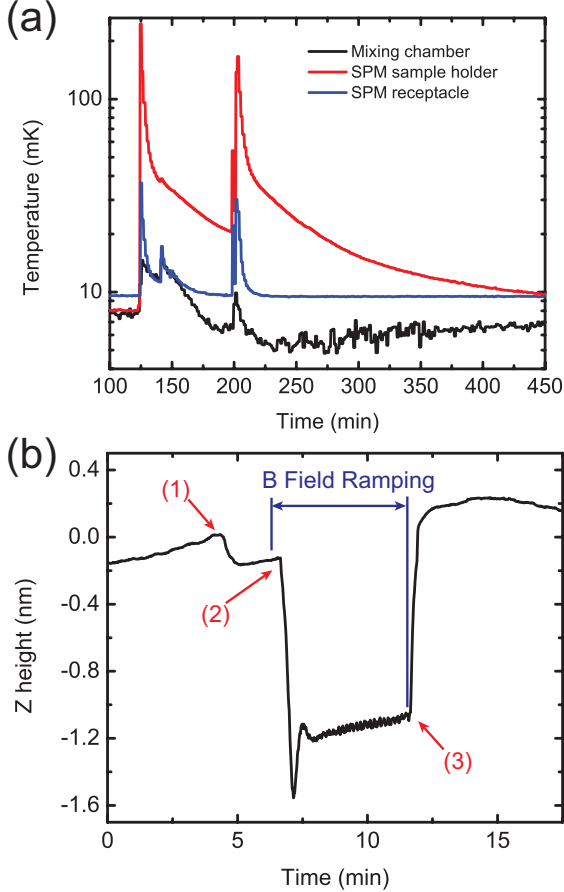


FIG. 26. Effects of the piezo motor operation and magnetic field ramping on the SPM measurements. (a) Temperature of the mixing chamber, sample holder, and SPM receptacle from RX sensors vs. time during the operation of the  $Z$ -piezo motor. The first rise in temperature comes from walking backward by 20 steps with 230V, and the second while approaching forward by 6 coarse and 4 fine steps with 280V and 240V, respectively. (b) SPM servo  $Z$ -height signal vs. time while the magnetic field was changed from 13.5 T to 13.25 T with a ramping speed of  $0.1 \text{ T min}^{-1}$ . The feedback loop was closed during the measurement. Point (1) corresponds to the opening of the superconducting switch from persistent mode, (2) the beginning of the field ramp, (3) the end of the field ramp. The fine oscillations during the ramp correspond to atomic corrugation due to raster scanning an image while the field was ramping.

### B. Effects of Piezo Walker Motion and Magnetic Field Ramps

When operating at low temperature, any activity is a potential heat source that could generate unwanted tem-

perature changes. During tunneling and scanning we find no detectable change in sample temperature in our system. However, temperature increases are observed when the  $XYZ$  coarse positioners are activated. Figure 26(a) shows the change in temperature of the mixing chamber, SPM module receptacle, and SPM sample receptacle during the motion of the  $Z$ -positioner. This is expected because the coarse positioners are activated with relatively high voltages ( $\approx 600 \text{ V}$ ) and high currents due to the fast transient into the  $\approx 2 \text{ nF}$  capacitance of the piezo motors. The highest temperature increase occurs in the sample, since this is the closest object to the  $Z$ -piezo motors. After operating the  $Z$ -positioner the temperature decays back to its equilibrium values.

Another operation that can disturb the SPM operation is the ramping of the magnetic field. Careful attention was paid in the design and construction of the SPM module to avoid any magnetic materials. The result of this effort is that the SPM scanner is rather insensitive to ramping the magnetic field (Fig. 26(b)). A change of only 1 nm in  $Z$ -error signal is observed when the magnetic field is changed at a rate of  $0.1 \text{ T min}^{-1}$ , with transients at the beginning and end of the ramp, and a stable position during the ramp. The SPM system can easily remain tunneling during the field ramps. This can save a great deal of time by eliminating  $Z$ -drift due to the piezo creep that results from retraction of the tip. The small undulations in the  $Z$ -error signal during the field ramp in Fig. 26(b) come from scanning over a graphene lattice during the ramp; atomic imaging was still achieved during this field ramp.

### C. Amplifier Noise Measurements

As described in Section VI, the home-made cryogenic preamplifiers for STM/STS and AFM operations are installed on the still plate of the dilution refrigerator (at an operating temperature of 700 mK) in order to reduce noise in the current measurements. To compare measurements of the cryogenic preamplifier with an external preamplifier,<sup>113</sup> we measured power spectral densities of the tunneling current in open and closed loop modes, and with the tip retracted (Fig. 27). With the tip retracted (zero tunneling current) the measurements show the base line noise of the amplifiers, including all noise sources (cables, amplifiers, interference, ground loops, microphonics, etc.). With the feedback open the measurements are sensitive to anything that causes tip-sample displacement. With the feedback closed the measurements will include additional noise due to the tunneling current and feedback loop. The external amplifier, connected by long cables, shows an increase in spectral noise at 1.3 kHz in addition to pickup of 60 Hz power line frequency and harmonics (Fig. 27(a)). These features remain when tunneling in both open and closed loop modes. The broad peak at 1.3 kHz is due to the cable capacitance, as described in the previous section. In contrast, the internal

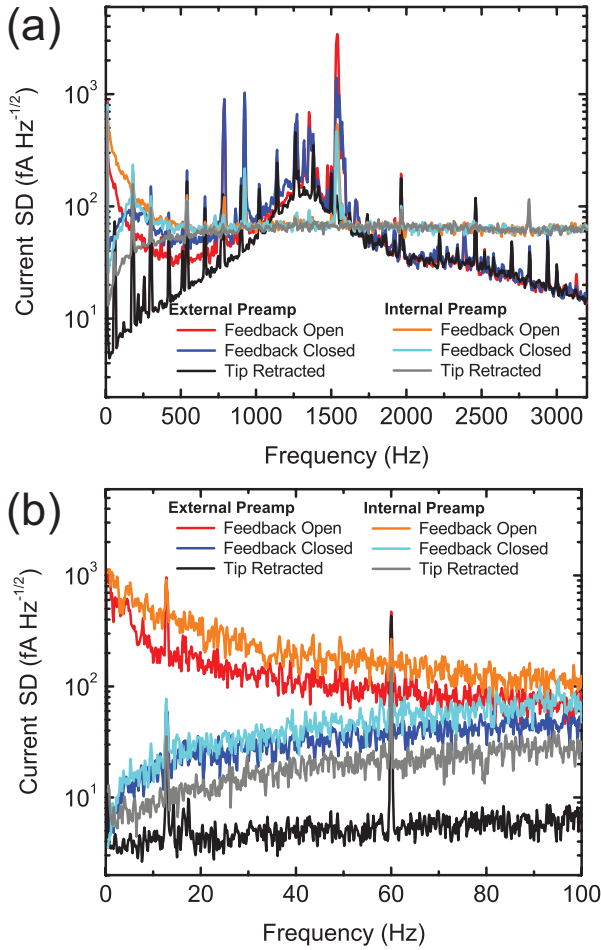


FIG. 27. Spectral density (SD) measurements of the current vs. frequency measured on Ag (111) with a W tip using an external preamplifier<sup>113</sup> and a NIST-built internal preamplifier (Fig. 25(d)). Data is shown for cases of an open feedback loop (red and orange), a closed feedback loop (blue and light blue), and for the tip retracted out of tunnel range (black and gray). (a) Frequency band DC to 3.2 kHz and (b) Frequency band DC to 100 Hz. Tunneling parameters: tunneling current setpoint 100 pA, sample bias 2.0 V. DR parameters: JT mode flow rate  $100 \mu\text{mol s}^{-1}$ ,  $T=13$  mK.

amplifier shows a flat frequency response with a spectral density of  $100 \text{ fA Hz}^{-1/2}$  beyond a few hundred Hz, and reduced sensitivity to the pick-up of power line noise. Comparing the two preamps, the base line noise of the external preamp is lower for frequencies below 1 kHz. At frequencies below 100 Hz (Fig. 27(b)) both preamps show comparable noise properties, in particular when tunneling with the feedback open.

The internal preamp shows a number of improvements compared to the external preamp. The frequency response is relatively flat, and is more immune to power-line noise pickup. The only drawback is the larger baseline noise level which we believe is due to the intrinsic noise of the GaAs  $n$ -MESFET. We plan in the future to replace the MESFET with a GaAs MOSFET, which we

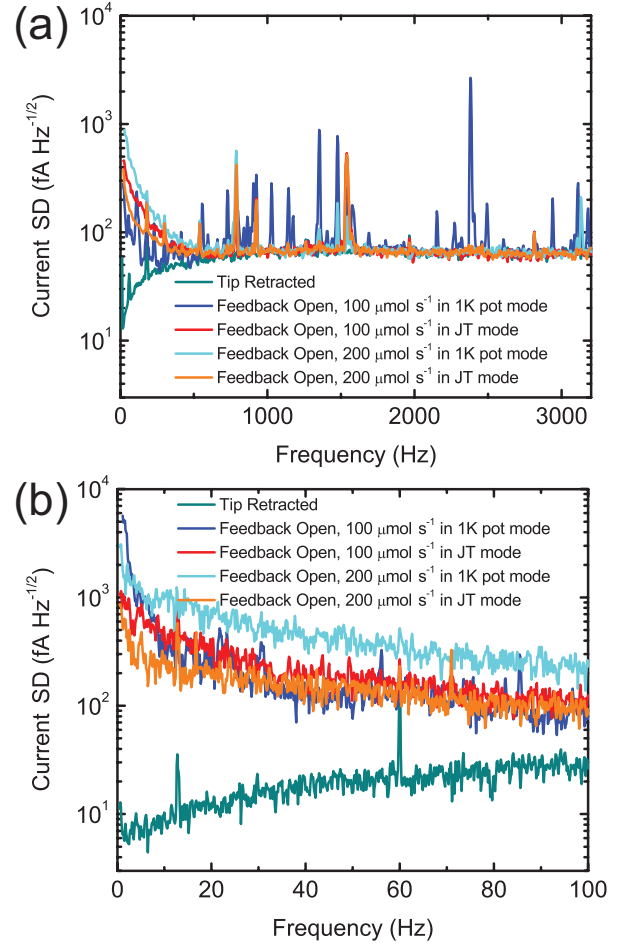


FIG. 28. Spectral density (SD) of the current noise vs. frequency, in both 1 K pot and JT condensing modes, with different mixture flow rates of  $100 \mu\text{mol s}^{-1}$  and  $200 \mu\text{mol s}^{-1}$ . (a) Frequencies from DC to 3.2 kHz and (b) Frequencies from DC to 100 Hz. All the measurements were done with an open servo feedback loop to be more sensitive to external mechanical noise. Green curves indicate the same measurements with the tip retracted, which determines the baseline (zero tunnel current) electronic noise. Data were measured on Ag (111) surface with a W tip using the NIST-built internal preamplifier (Fig. 25(d)) and a spectrum analyzer<sup>114</sup>. Tunneling parameters: tunneling current setpoint 100 pA, sample bias 2.0 V,  $T=13$  mK.

expect to give a lower background noise level.

#### D. Tunneling Noise Measurements: Comparing the Joule-Thomson and 1 K pot Condensing Modes

Figure 28 shows a comparison of the current spectral density (SD) noise measurements when the JT and 1 K pot condensing modes are used, for frequencies up to 3 kHz (Fig. 28(a)) and low frequencies below 100 Hz (Fig. 28(b)). The measurements are performed with the feedback open, which is very sensitive to any tip-sample

relative displacement. Focusing on the higher frequencies first, we observe a large number of peaks that are excited by the operation of the 1 K pot (dark blue and light blue traces in Fig. 28(a)). These are probably related to the liquid helium flow through the needle valve exciting mechanical vibrations in the DR. At low frequencies, however, the SD measurements are very similar between the JT and 1 K pot modes, except that the current noise is independent of mixture flow rate in the JT mode, whereas in the 1 K pot mode, the current noise increases by a factor of three when the flow rate is doubled. For this reason, we perform all of our SPM measurements in JT

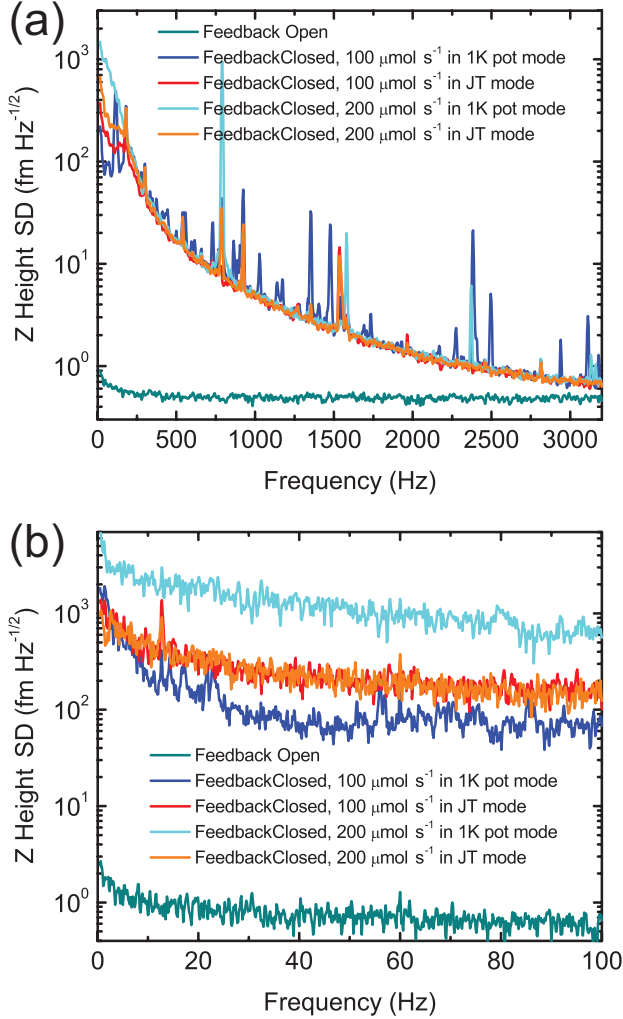


FIG. 29. Spectral density (SD) of the  $Z$ -height signal in both the 1 K pot and JT condensing modes with different mixture flow rates of  $100 \mu\text{mol s}^{-1}$  and  $200 \mu\text{mol s}^{-1}$ . (a) DC to 3.2 kHz frequency band and (b) DC to 100 Hz frequency band. Green curves are the measurement with an open feedback loop, which determines the base noise limit of the electronics at fixed  $Z$ . Data were measured on a Ag (111) surface with a W tip using the NIST-built internal preamplifier (Fig. 25(d)) and a spectrum analyzer<sup>114</sup>. Tunneling parameters: tunneling current setpoint 100 pA, sample bias 2.0 V,  $T=13$  mK.

mode, and use the 1 K pot only when cooling the DR from much higher temperatures, (*e.g.* when the SPM module is loaded into the DR after a sample and tip exchange).

In JT mode, the current SD in Figure 28 shows good noise performance with the feedback open, approaching  $100 \text{ fA Hz}^{-1/2}$  at 100 Hz. This corresponds to very small displacement amplitudes, which can be observed directly by measuring the  $Z$ -height SD (Fig. 29). With the feedback loop closed, the SPM servo compensates these current fluctuations by moving the tip. The tip-sample distance will then show up in the  $Z$ -error signal, as shown in Fig. 29. Similar to the feedback-open current measurements in Fig. 28, the  $Z$ -height SD measurements show that the operation of the 1 K pot can produce tip-sample fluctuations that are one to two orders of magnitude larger than the JT mode at isolated frequencies (Fig. 29(a)). Again the JT mode is insensitive to flow rate, while the 1 K pot operation increases the tip-sample fluctuations by at least a factor of ten when the flow rate is doubled from  $100 \mu\text{mol s}^{-1}$  to  $200 \mu\text{mol s}^{-1}$ . The overall noise performance in JT mode is very good with tip-sample fluctuations lower than  $100 \text{ fm Hz}^{-1/2}$  for frequencies above 100 Hz. These values allow high signal-to-noise ratios in STS measurements, as shown below.

## E. STM and STS Measurements

The facility began operating in November of 2009, and a number of experimental projects are underway at the time of this writing including: spin-excitation spectroscopy of single magnetic atoms on  $\text{Cu}_2\text{N}$ , the 2-dimensional graphene electron system in the quantum Hall regime, and topological insulators. Here we briefly describe a few results from these experiments.

### 1. $\text{Cu}_2\text{N}$ on $\text{Cu}(100)$

Spin-excitation spectroscopy is a form of inelastic tunneling spectroscopy involving the flipping of the spin state of single magnetic atoms absorbed on thin insulating films on a metal substrate.<sup>65</sup> For this experiment we prepared an insulating layer of  $\text{Cu}_2\text{N}$  on a  $\text{Cu}(100)$  surface in the metal MBE chamber ((1) in Fig. 2)<sup>129</sup>. Nitrogen ions were sputtered into the  $\text{Cu}(100)$  surface at 500 eV at room temperature. The Cu crystal was subsequently annealed at  $350 \text{ }^\circ\text{C}$  to form the  $c(2\times 2)$   $\text{Cu}_2\text{N}$  surface, which was verified by RHEED measurements. A dilute concentration of Er atoms was deposited on the  $\text{Cu}_2\text{N}$  surface while the sample was held at 1.5 K in the DR. As described in Section III, the SPM module was designed with line of sight access through the DR and SPM module to the sample surface (with the radiation shields open) to facilitate the deposition of single atoms onto a cold substrate. An evaporator system is installed in the

UHV chamber above the DR to evaporate atoms onto the cold sample surface while the SPM module is in the DR. The evaporator contains three separate e-beam evaporators, which can be positioned over the central tube of the DR. We deposited a dilute concentration of Er atoms using one of these custom made e-beam evaporators. After deposition, the DR  $^3\text{He}$ - $^4\text{He}$  mixture was condensed and the sample cooled to 10 mK. Figure 30 demonstrates the atomic imaging capability of the instrument at 13 mK. Shown is an 8 nm  $\times$  8 nm rendered STM image of the  $\text{Cu}_2\text{N}$  surface which has a small concentration of Er adatoms (blue arrow). The  $\text{Cu}_2\text{N}$  appears in small patches (corrugated areas) separated by regions of bare Cu(100) surface (smooth regions). This pattern is characteristic of  $\text{Cu}_2\text{N}$  on Cu(100) due to the strain that is developed in the  $\text{Cu}_2\text{N}/\text{Cu}(100)$  interface.

## 2. Epitaxial Graphene

We studied a sample of epitaxial graphene grown from the carbon terminated face (C-face) of a SiC crystal<sup>69</sup> to examine the 2-dimensional graphene electron system in the quantum Hall regime. Graphene has many fascinating electronic properties arising from the truly two-dimensional nature of its electron system which is directly accessible to surface probes. Graphene's carriers develop a unique Landau level quantization in the density of states in an applied magnetic field. As reported in our earlier studies at 4 K,<sup>68</sup> C-face grown epitaxial graphene is largely defect-free. As a result its  $N = 0$  Landau level peak in the density of states was observed to be only 1.5 meV wide (almost thermally limited) in tunneling spectroscopy measurements at 4 K and  $B = 5$  T, giving an estimated scattering time of  $\approx 0.4$  ps. For low magnetic fields, the Landau levels in graphene are four-fold degenerate. By going to lower temperatures below 4 K, we expect to resolve the individual degenerate levels for the first time.<sup>69</sup> Therefore epitaxial graphene is a good system for testing and demonstrating the high energy resolution enabled by ultra-low temperatures. In addition, the hexagonal atomic lattice of graphene, with a spacing of 0.25 nm, is ideal for testing and calibrating the topographic performance of the STM.

The epitaxial graphene measured in this work was grown *ex-situ* in an induction furnace,<sup>130</sup> and then annealed up to 200 °C for 15 minutes in our preparation chamber. A 0.5 mm diameter Ag tip was electrochemically etched in a solution of 25 % of ammonium hydroxide, 10 % to 15 % hydrogen peroxide, and ethanol mixed in a volume ratio of 1:1:1. The tip was cleaned by annealing in the FIM through repeated cycles of e-beam heating and imaging with field ion microscopy.

Figure 31(a) is a topographic STM image of an epitaxial graphene sample measured at 13 mK with a tunneling current of 0.1 nA and a sample bias voltage of  $-250$  mV. This image shows the hexagonal structure of graphene with unprocessed and unfiltered data. The initial  $X$  and

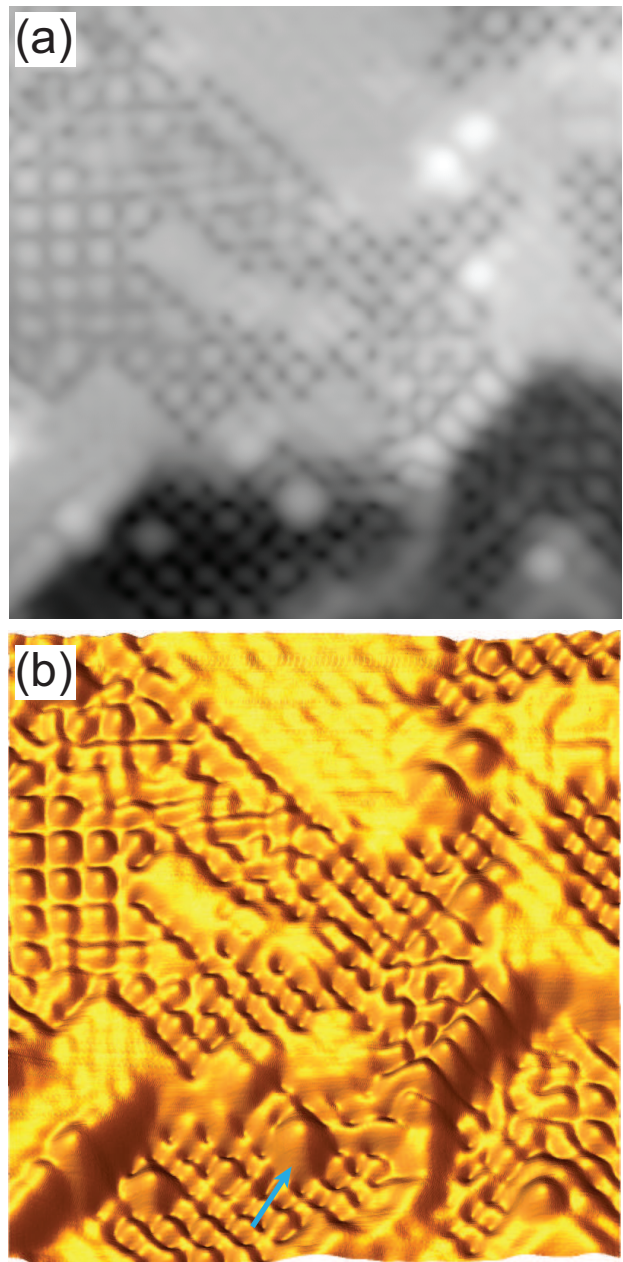


FIG. 30. STM images of single Er atoms deposited onto a  $\text{Cu}_2\text{N}$  surface grown on a Cu(100) single crystal. (a) Topographic STM image with the  $Z$ -height shown in a gray scale. Image size is 8 nm  $\times$  8 nm. (b) 3D rendered color version of the image in (a) which highlights the surface corrugation. The blue arrow points to a single adatom. The  $\text{Cu}_2\text{N}$  regions (corrugated areas) are separated by regions of the bare Cu(100) surface regions (smooth areas). Tunneling parameters: tunneling current setpoint 200 pA, sample bias 10 mV.  $T = 13$  mK

$Y$  calibration of the SPM scanner are based on this well-known carbon lattice (the  $Z$  calibration was obtained from step heights on a Ag (111) sample). Figure 31(b) shows a height profile along the white line (3 nm) in Fig. 31(a). The excellent  $Z$  signal-to-noise ratio on these small 40 pm height variations confirms our expectations from the noise measurements presented in the previous sections.

As mentioned previously, tunneling spectroscopy is a more demanding test of SPM performance because the measurements are made with the feedback loop open. The exponential dependence of tunnel current on the width of the tunnel junction makes STS tremendously sensitive to fluctuations of the tip-sample separation (on top of electronic noise). Figure 32(a) shows an STS mea-

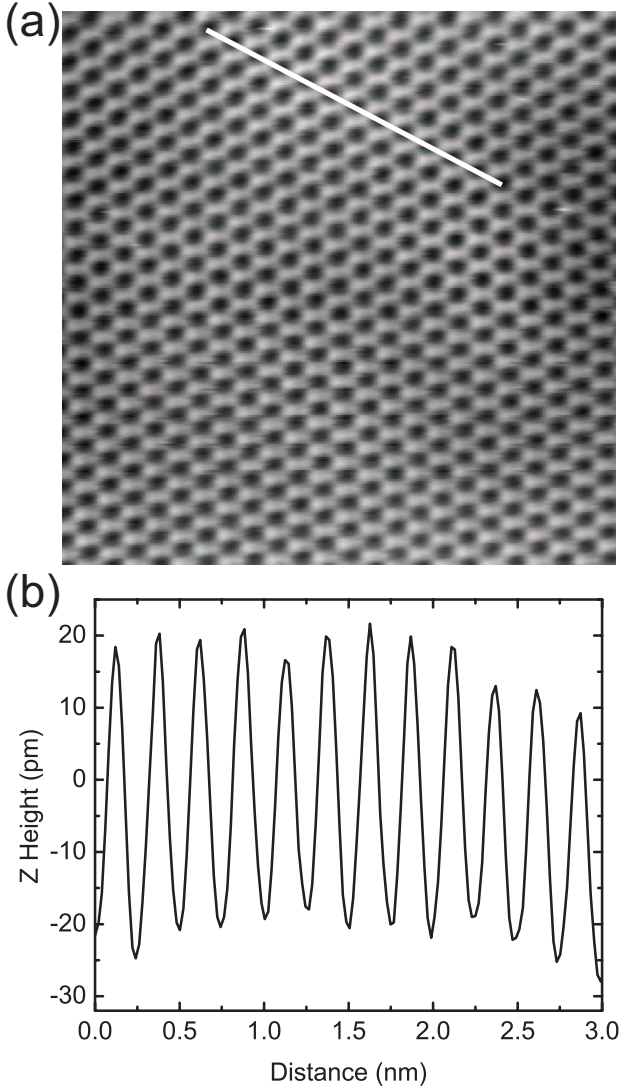


FIG. 31. STM measurements of epitaxial graphene grown on the C-face SiC. (a) High resolution STM image of the epitaxial graphene sample measured at 13 mK. Image size 5 nm  $\times$  5 nm. Tunneling parameters: tunneling current setpoint 100 pA, sample bias  $-250$  mV. (b)  $Z$ -height profile cross-section taken along the white line in (a).

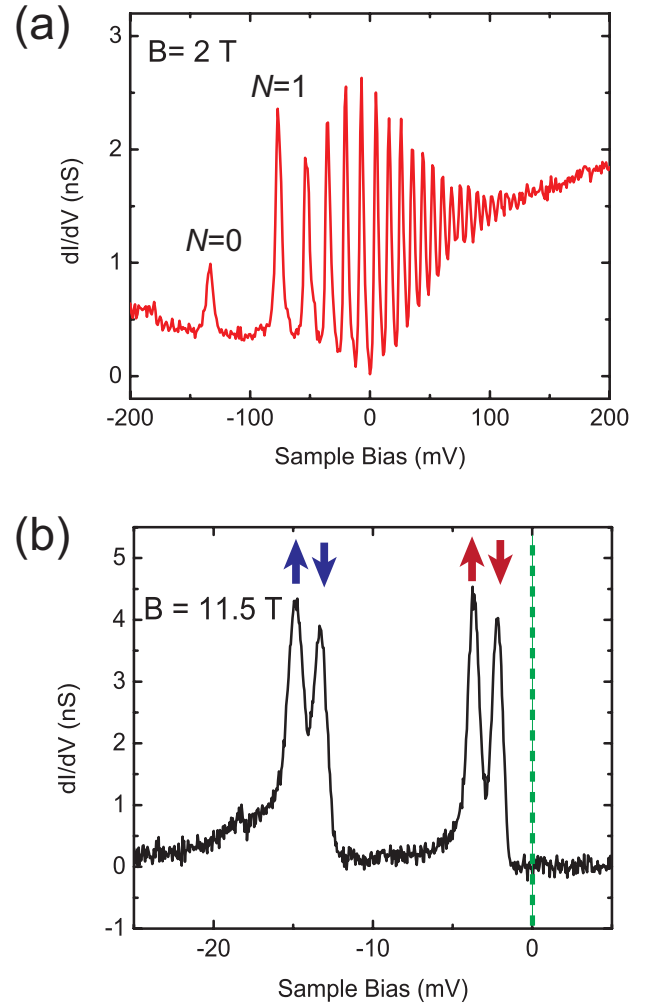


FIG. 32. Spectroscopic STS measurements of epitaxial graphene. (a)  $dI/dV$  spectrum showing Landau levels at  $B=2$  T. The  $N=0$  Landau level is observed at  $-134$  mV with over 20 other Landau levels clearly resolved. Tunneling parameters: tunneling current setpoint 300 pA, sample bias  $-300$  mV, modulation voltage 1 mV. (b) High resolution  $dI/dV$  spectrum of the  $N=1$  Landau level at  $B=11.5$  T showing the lifting of the four-fold degeneracy due to electron spin (up and down arrows) and valley (blue and red) degeneracies. Tunneling parameters: tunneling current setpoint 400 pA, sample bias  $-250$  mV, modulation voltage  $50 \mu\text{V}$ .

surement on graphene in a magnetic field of 2 T with a junction impedance of 1 G $\Omega$ . Over 20 sharp Landau levels are observed with good signal to noise. The linewidths in Fig. 32(a) are limited by the 1 mV modulation amplitude used in the measurement. By lowering the modulation voltage, we are able to go to higher resolution measurements, as shown in Fig. 32(b). Here at much higher field, the  $N=1$  Landau level lies just below the Fermi energy (located at 0 V sample bias). The full four-fold degeneracy of the Landau level is now lifted and resolved. By comparing the energy gaps between the peaks, we can assign the electron spin up and spin down

levels (up and down arrows) with the smaller Zeeman energy splitting, which was confirmed with field dependent measurements.<sup>69</sup> The larger gap (red vs blue) is due to the lifting of the valley degeneracy in graphene.<sup>69</sup> The linewidths of the peaks, in the range of 0.5 mV, represent the intrinsic lifetime of the Landau levels due to scattering. While these measurements do not show the ultimate resolution of the instrument, they do show high signal-to-noise ratio, and the lowest temperature SPM measurements to date. Future measurements on superconducting samples are planned to fully test the resolution of the system.

## VIII. SUMMARY

In this article we have described the design, construction, and performance of a novel SPM facility that operates at temperatures as low as 10 mK and high magnetic fields up to 15 T. We have documented our experience with new low noise cryogenic techniques adapted to a dilution refrigeration technology, such as the use of a Joule-Thomson condenser which gives lower noise performance in operating an SPM with a dilution refrigerator. Detailed descriptions of the designs and resulting performance will help future investigators adopt cryogenic techniques to SPM instruments, which is the goal of this article. Our measurements indicate that measurements are now limited by electrical noise, and further improvements in cryogenic amplifiers and signal handling will likely play an important role in future instruments.

As SPMs move into the new phase space of ultra-low temperatures and high magnetic fields, we feel new scientific frontiers will be opened with stunning discoveries. Our recent measurements on the epitaxial graphene system have already shown the discovery of new many body states corresponding to fractionally filled Landau levels.<sup>69</sup> Further discoveries are expected just around the corner. We look forward to a continued bright future in scanned probe microscopy.

## IX. REFERENCES

- <sup>1</sup>H. Kamerlingh-Onnes, Comm. Phys. Lab. Univ. Leiden. No. B, **120**, 3 (1911).
- <sup>2</sup>K. v. Klitzing, G. Dorda, and M. Pepper, Physical Review Letters, **45**, 494 (1980).
- <sup>3</sup>D. C. Tsui, H. L. Stormer, and A. C. Gossard, Physical Review Letters, **48**, 1559 (1982).
- <sup>4</sup>S. A. Elrod, A. L. de Lozanne, and C. F. Quate, Applied Physics Letters, **45**, 1240 (1984).
- <sup>5</sup>O. Marti, G. Binnig, H. Rohrer, and H. Salemk, Surface Science, **181**, 230 (1987).
- <sup>6</sup>H. F. Hess, R. B. Robinson, R. C. Dynes, J. M. Valles, and J. V. Waszczak, Physical Review Letters, **62**, 214 (1989).
- <sup>7</sup>D. M. Eigler and E. K. Schweizer, Nature, **344**, 524 (1990).
- <sup>8</sup>S. H. Tessmer, D. J. V. Harlingen, and J. W. Lyding, Review of Scientific Instruments, **65**, 2855 (1994).
- <sup>9</sup>J. W. G. Wildöer, A. J. A. van Roy, H. van Kempen, and C. J. P. M. Harmans, Review of Scientific Instruments, **65**, 2849 (1994).
- <sup>10</sup>G. Meyer, Review of Scientific Instruments, **67**, 2960 (1996).
- <sup>11</sup>C. Wittneven, R. Dombrowski, S. H. Pan, and R. Wiesendanger, Review of Scientific Instruments, **68**, 3806 (1997).
- <sup>12</sup>J. H. Ferris, J. G. Kushmerick, J. A. Johnson, M. G. Y. Youngquist, R. B. Kessinger, H. F. Kingsbury, and P. S. Weiss, Review of Scientific Instruments, **69**, 2691 (1998).
- <sup>13</sup>H. J. Hug, B. Stiefel, P. J. A. van Schendel, A. Moser, S. Martin, and H. Güntherodt, Review of Scientific Instruments, **70**, 3625 (1999).
- <sup>14</sup>B. C. Stipe, M. A. Rezaei, and W. Ho, Review of Scientific Instruments, **70**, 137 (1999).
- <sup>15</sup>O. Pietzsch, A. Kubetzka, D. Haude, M. Bode, and R. Wiesendanger, Review of Scientific Instruments, **71**, 424 (2000).
- <sup>16</sup>E. T. Foley, A. F. Kam, and J. W. Lyding, Review of Scientific Instruments, **71**, 3428 (2000).
- <sup>17</sup>C. E. Sosolik, J. A. Stroscio, M. D. Stiles, E. W. Hudson, S. R. Blankenship, A. P. Fein, and R. J. Celotta, Physical Review B, **68**, 140503 (2003).
- <sup>18</sup>M. Dreyer, J. Lee, H. Wang, and B. Barker, Review of Scientific Instruments, **81**, 053703 (2010).
- <sup>19</sup>A. P. Fein, J. R. Kirtley, and R. M. Feenstra, Review of Scientific Instruments, **58**, 1806 (1987).
- <sup>20</sup>H. F. Hess, R. B. Robinson, and J. V. Waszczak, Physical Review Letters, **64**, 2711 (1990).
- <sup>21</sup>S. H. Pan, E. W. Hudson, and J. C. Davis, Review of Scientific Instruments, **70**, 1459 (1999).
- <sup>22</sup>M. Kugler, C. Renner, O. Fischer, V. Mikheev, and G. Batey, Review of Scientific Instruments, **71**, 1475 (2000).
- <sup>23</sup>A. J. Heinrich, C. P. Lutz, J. A. Gupta, and D. M. Eigler, Science, **298**, 1381 (2002).
- <sup>24</sup>H. Suderow, M. Crespo, P. Martinez-Samper, J. G. Rodrigo, G. Rubio-Bollinger, S. Vieira, N. Luchier, J. P. Brison, and P. C. Canfield, Physica C: Superconductivity, **369**, 106 (2002).
- <sup>25</sup>J. Wiebe, A. Wachowiak, F. Meier, D. Haude, T. Foster, M. Morgenstern, and R. Wiesendanger, Review of Scientific Instruments, **75**, 4871 (2004).
- <sup>26</sup>S. Ilani, J. Martin, E. Teitelbaum, J. H. Smet, D. Mahalu, V. Umansky, and A. Yacoby, Nature, **427**, 328 (2004).
- <sup>27</sup>T. Hanaguri, Journal of Physics: Conference Series, **51**, 514 (2006), ISSN 1742-6588.
- <sup>28</sup>Y. Fu, S. Ji, X. Chen, X. Ma, R. Wu, C. Wang, W. Duan, X. Qiu, B. Sun, P. Zhang, J. Jia, and Q. Xue, Physical Review Letters, **99**, 256601 (2007).
- <sup>29</sup>X. Chen, Y. Fu, S. Ji, T. Zhang, P. Cheng, X. Ma, X. Zou, W. Duan, J. Jia, and Q. Xue, Physical Review Letters, **101**, 197208 (2008).
- <sup>30</sup>A. F. Otte, *Magnetism of a single atom*, Ph.D. thesis, Leiden University (2008).
- <sup>31</sup>N. Tsukahara, K. ichi Noto, M. Ohara, S. Shiraki, N. Takagi, Y. Takata, J. Miyawaki, M. Taguchi, A. Chainani, S. Shin, and M. Kawai, Physical Review Letters, **102**, 167203 (2009).
- <sup>32</sup>P. Davidsson, H. Olin, M. Persson, and S. Pehrson, Ultramicroscopy, **42-44**, 1470 (1992).
- <sup>33</sup>D. V. Pelekhov, J. B. Becker, and J. Nunes, Review of Scientific Instruments, **70**, 114 (1999).
- <sup>34</sup>N. Moussy, H. Courtois, and B. Pannetier, Review of Scientific Instruments, **72**, 128 (2001).
- <sup>35</sup>M. Upward, J. Janssen, L. Gurevich, A. Morpurgo, and L. Kouwenhoven, Applied Physics A Materials Science & Processing, **72**, S253 (2001).
- <sup>36</sup>H. J. Mamin and D. Rugar, Applied Physics Letters, **79**, 3358 (2001).
- <sup>37</sup>P. G. Björnsson, B. W. Gardner, J. R. Kirtley, and K. A. Moler, Review of Scientific Instruments, **72**, 4153 (2001).
- <sup>38</sup>K. R. Brown, L. Sun, and B. E. Kane, Review of Scientific Instruments, **75**, 2029 (2004).
- <sup>39</sup>A. E. Gildemeister, T. Ihn, C. Barento, P. Studerus, and K. En-

- sslin, Review of Scientific Instruments, **78**, 013704 (2007).
- <sup>40</sup>H. Kambara, T. Matsui, Y. Niimi, and H. Fukuyama, Review of Scientific Instruments, **78**, 073703 (2007).
- <sup>41</sup>Peter Grutter, McGill University, private communication.
- <sup>42</sup>Hermann Suderow, Universidad Autónoma de Madrid, private communication.
- <sup>43</sup>H. Amick, M. Gendreau, T. Busch, and C. Gordon, Proceedings of SPIE Conference 5933: Buildings for Nanoscale Research and Beyond (2005).
- <sup>44</sup>G. Binnig, H. Rohrer, C. Gerber, and E. Weibel, Physical Review Letters, **49**, 57 (1982).
- <sup>45</sup>G. Binnig, Applied Physics Letters, **40**, 178 (1982).
- <sup>46</sup>G. Binnig and H. Rohrer, Reviews of Modern Physics, **59**, 615 (1987).
- <sup>47</sup>G. Binnig, H. Rohrer, C. Gerber, and E. Weibel, Physical Review Letters, **50**, 120 (1983).
- <sup>48</sup>E. W. Müller and T. T. Tsong, *Field Ion Microscopy, Field Ionization, and Field Evaporation*, 1st ed., Progress in surface science No. v. 4, pt. 1 (Pergamon Press, Oxford, 1973) ISBN 0080177794, p. 139.
- <sup>49</sup>T. Sakurai, A. Sakai, and H. W. Pickering, *Atom-Probe Field Ion Microscopy and Its Applications*, Advances in electronics and electron physics No. 20 (Academic Press, Boston, 1989) ISBN 0120145820, p. 299.
- <sup>50</sup>T. T. Tsong, *Atom-Probe Field Ion Microscopy: Field Ion Emission, and Surfaces and Interfaces at Atomic Resolution* (Cambridge University Press, Cambridge, 2005) ISBN 0521019931, p. 387.
- <sup>51</sup>J. A. Stroscio and W. J. Kaiser, *Scanning Tunneling Microscopy*, Methods of experimental physics (Academic Press, Boston, 1993) ISBN 0124759726, p. 459.
- <sup>52</sup>D. A. Bonnell, *Scanning Tunneling Microscopy and Spectroscopy: Theory, Techniques, and Applications* (VCH, New York, N.Y., 1993) ISBN 089573768X, p. 436.
- <sup>53</sup>O. Marti and M. Amrein, *STM and SFM in Biology* (Academic Press, San Diego, 1993) ISBN 0124745008, p. 331.
- <sup>54</sup>H. J. Güntherodt and R. Wiesendanger, *Scanning Tunneling Microscopy I: General Principles and Applications to Clean and Adsorbate-Covered Surfaces*, 2nd ed., Springer series in surface sciences No. 20 (Springer-Verlag, Berlin, 1994) ISBN 3540584153, p. 280.
- <sup>55</sup>R. Wiesendanger, H. J. Güntherodt, and W. Baumeister, *Scanning Tunneling Microscopy II: Further Applications and Related Scanning Techniques*, 2nd ed., Springer series in surface sciences No. 28 (Springer, Berlin, 1995) ISBN 3540585893, p. 349.
- <sup>56</sup>R. Wiesendanger and H. J. Güntherodt, *Scanning Tunneling Microscopy III: Theory of STM and Related Scanning Probe Methods*, 2nd ed., Springer series in surface sciences No. 29 (Springer, Berlin, 1996) ISBN 3540608249, p. 402.
- <sup>57</sup>S. Morita, *Roadmap of Scanning Probe Microscopy*, Nanoscience and technology (Springer, Berlin, 2007) ISBN 9783540343141, p. 201.
- <sup>58</sup>C. J. Chen, *Introduction to Scanning Tunneling Microscopy*, 2nd ed. (Oxford University Press, Oxford, 2008) ISBN 9780199211500, p. 423.
- <sup>59</sup>R. Young, Review of Scientific Instruments, **43**, 999 (1972).
- <sup>60</sup>A. L. de Lozanne, S. A. Elrod, and C. F. Quate, Physical Review Letters, **54**, 2433 (1985).
- <sup>61</sup>Ø. Fischer, M. Kugler, I. Maggio-Aprile, C. Berthod, and C. Renner, Reviews of Modern Physics, **79**, 353 (2007).
- <sup>62</sup>H. J. Hug, T. Jung, and H. Güntherodt, Review of Scientific Instruments, **63**, 3900 (1992).
- <sup>63</sup>J. A. Stroscio and R. J. Celotta, Science, **306**, 242 (2004).
- <sup>64</sup>B. C. Stipe, M. A. Rezaei, and W. Ho, Science, **280**, 1732 (1998).
- <sup>65</sup>A. J. Heinrich, J. A. Gupta, C. P. Lutz, and D. M. Eigler, Science, **306**, 466 (2004).
- <sup>66</sup>R. Wiesendanger, Reviews of Modern Physics, **81**, 1495 (2009).
- <sup>67</sup>K. Hashimoto, C. Sohrmann, J. Wiebe, T. Inaoka, F. Meier, Y. Hirayama, R. A. Rmer, R. Wiesendanger, and M. Morgenstern, Physical Review Letters, **101**, 256802 (2008).
- <sup>68</sup>D. L. Miller, K. D. Kubista, G. M. Rutter, M. Ruan, W. A. de Heer, P. N. First, and J. A. Stroscio, Science (New York, N.Y.), **324**, 924 (2009).
- <sup>69</sup>Y. J. Song, A. F. Otte, Y. Kuk, Y. Hu, D. B. Torrance, P. N. First, W. A. de Heer, H. Min, S. Adam, M. D. Stiles, A. H. MacDonald, and J. A. Stroscio, Nature, **467**, 185 (2010), ISSN 0028-0836.
- <sup>70</sup>M. Morgenstern, D. Haude, C. Meyer, and R. Wiesendanger, Physical Review B, **64**, 205104 (2001).
- <sup>71</sup>Hemi Heating AB, SE-151 02 Södertälje, Sweden.
- <sup>72</sup>Model APD 3040PS 12/10/8 I 60:1 P20, BURLE Electro-Optics, Inc., Sturbridge, MA.
- <sup>73</sup>Model EMX-3.0-1-1-6/B-6/LM/MY-Z/LS-Z/CBF, Thermionics, Port Townsend, WA.
- <sup>74</sup>CryoVac Gesellschaft für Tieftemperaturtechnik mbH & Co KG Heuserweg 14 53842 Troisdorf Germany.
- <sup>75</sup>McAllister Technical Services West 280 Prairie Avenue Coeur d'Alene, ID.
- <sup>76</sup>K. Besocke, Surface Science, **181**, 145 (1987).
- <sup>77</sup>J. Frohn, J. F. Wolf, K. Besocke, and M. Teske, Review of Scientific Instruments, **60**, 1200 (1989).
- <sup>78</sup>S. H. Pan, "Pub. No.: (WO/1993/019494) International Application No.: PCT/GB1993/000539 PIEZOELECTRIC MOTOR."
- <sup>79</sup>N. Surepure Chemetals, Florham Park, Surepure Chemetals, Precious & Specialty Metals Supplier.
- <sup>80</sup>C. T. V. Degrift, Physica B+C, **107**, 605 (1981).
- <sup>81</sup>EBL #4, Staveley Sensors, Inc., EBL Product Line, E. Hartford, CT.
- <sup>82</sup>Model WMG40-340-95-EMS, Ferrovac GmbH, CH 8050 Zurich, Switzerland.
- <sup>83</sup>Model AH 2700A, Andeen-Hagerling, Inc., Cleveland, OH.
- <sup>84</sup>F. Pobell, *Matter and methods at low temperatures* (Springer, 1996) ISBN 3540585729, 9783540585725.
- <sup>85</sup>O. V. Lounasmaa, *Experimental Principles and Methods Below 1 K* (Academic Press, London, 1974) ISBN 0124559506, p. 316.
- <sup>86</sup>R. C. Richardson and E. N. Smith, *Experimental Techniques in Condensed Matter Physics at Low Temperatures*, Frontiers in physics No. 67 (Addison-Wesley Pub. Co, Redwood City, Calif, 1988) ISBN 0201150026, p. 338.
- <sup>87</sup>A. Raccanelli, L. A. Reichertz, and E. Kreysa, Cryogenics, **41**, 763 (2001).
- <sup>88</sup>G. Lawes, G. M. Zassenhaus, S. Koch, E. N. Smith, J. D. Reppy, and J. M. Parpia, Review of Scientific Instruments, **69**, 4176 (1998).
- <sup>89</sup>P. Gorla, C. Bucci, and S. Pirro, Nuclear Instruments and Methods in Physics Research Section A: Accelerators, Spectrometers, Detectors and Associated Equipment, **520**, 641 (2004).
- <sup>90</sup>K. Uhlig, Cryogenics, **27**, 454 (1987).
- <sup>91</sup>Model 302 bellows compressor, Senior Aerospace Metal Bellows, Sharon, MA.
- <sup>92</sup>Model JDR-500, Janis Research Company, Inc., Wilmington, MA.
- <sup>93</sup>Cryogenics Ltd., London W3 7QE, UK.
- <sup>94</sup>Precision Cryogenics, Indianapolis, IN.
- <sup>95</sup>Model 602BW single stage Roots pump, followed by model A100L 6 stage Roots pump, Alcatel-Adixen, USA.
- <sup>96</sup>New England Wire, Lisbon, NH.
- <sup>97</sup>Model ESP300, Newport Corporation, Irvine, CA.
- <sup>98</sup>Model RX-102A-BR, Lake Shore Cryotronics, Inc., Westerville OH.
- <sup>99</sup>Model 4263B, Agilent Technologies, Santa Clara CA.
- <sup>100</sup>R. S. Jr and R. B. Dove, NBS Special Publicaiton, **260-62** (1979).
- <sup>101</sup>R. S. Jr, Cryogenics, **14**, 250 (1974).
- <sup>102</sup>Model 370, LakeShore Cryotronics, Inc., Westerville OH.
- <sup>103</sup>Type 7110, Epoxy Technology, Inc., Bellerica, MA.

- <sup>104</sup>Type 4110, Epoxy Technology, Inc., Bellerica, MA,.
- <sup>105</sup>Model HS-1, Geospace Technologies, Houston, Texas,.
- <sup>106</sup>S. il Park and C. F. Quate, Review of Scientific Instruments, **58**, 2010 (1987).
- <sup>107</sup>Y. Kuk and P. J. Silverman, Review of Scientific Instruments, **60**, 165 (1989).
- <sup>108</sup>A. I. Oliva, V. Sosa, R. de Coss, R. Sosa, N. L. Salazar, and J. L. Peña, Review of Scientific Instruments, **63**, 3326 (1992).
- <sup>109</sup>Model PD 3001 H, Integrated Dynamics Engineering, 377 University Avenue, Westwood, MA,.
- <sup>110</sup>Model TCN 500, Integrated Dynamics Engineering, 377 University Avenue, Westwood, MA,.
- <sup>111</sup>Integrated Dynamics Engineering, 377 University Avenue, Westwood, MA,.
- <sup>112</sup>Model 731A/P31, Wilcoxon Research, Inc., Germantown, MD,.
- <sup>113</sup>Model 1211, DL Instruments, Ithaca, NY,.
- <sup>114</sup>SR785, Stanford Research Systems, Inc.,
- <sup>115</sup>S. il Park and C. F. Quate, Review of Scientific Instruments, **58**, 2004 (1987).
- <sup>116</sup>Model SR554, Stanford Research Systems, Inc., Sunnyvale, CA,.
- <sup>117</sup>Model 7124, Signal Recovery, AMETEK, Inc., Oak Ridge, TN,.
- <sup>118</sup>Model E6173, Agilent Technologies, Inc., Santa Clara, CA,.
- <sup>119</sup>Model PA88A, Apex Linear Amplifier, Cirrus Logic, Inc., Austin TX,.
- <sup>120</sup>Model NI PXI-6713, National Instruments, Austin, TX,.
- <sup>121</sup>Model PA89, Apex Linear Amplifier, Cirrus Logic, Inc., Austin TX,.
- <sup>122</sup>A dual channel SGM 2006M, SONY,.
- <sup>123</sup>OPA 627, Texas Instruments,.
- <sup>124</sup>Burr-Brown Application Bulletin: Photodiode Monitoring with OP Amps, SBOA035 (AB-075). Available from <http://focus.ti.com/lit/an/sboa035/sboa035.pdf> .
- <sup>125</sup>A dual channel TPS 1120, Texas Instruments,.
- <sup>126</sup>T. Lee, C. Chan, P. Tsai, S. S. Hsu, J. Kwo, and M. Hong, Journal of Crystal Growth, **301-302**, 1009 (2007).
- <sup>127</sup>M. Fujiwara and M. Sasaki, Electron Devices, IEEE Transactions on, **51**, 2042 (2004).
- <sup>128</sup>R. K. Kirschman, J. A. Lipa, and W. W. Hansen, SPIE, **1946**, 350 (1993).
- <sup>129</sup>M. Yamada, S. ya Ohno, Y. Iwasaki, K. Yagyu, K. Nakatsuji, and F. Komori, Surface Science, **604**, 1961 (2010), ISSN 0039-6028.
- <sup>130</sup>C. Berger, Z. Song, T. Li, X. Li, A. Y. Ogbazghi, R. Feng, Z. Dai, A. N. Marchenkov, E. H. Conrad, P. N. First, and W. A. de Heer, The Journal of Physical Chemistry B, **108**, 19912 (2004).

## ACKNOWLEDGMENTS

We thank P.N. First for a careful reading of the manuscript, B.Baker, H.Hug, D.M. Eigler, A.J. Heinrich, and E.W. Hudson for useful discussions on SPM and cryogenics, P.Heiland for insight into vibrational isolation solutions, N. Levy and T. Matsui for their help in the Cu<sub>2</sub>N experiments, J. Welker for his help with the quick-access STM/AFM, W.A.deHeer for supplying the epitaxial graphene samples, and G.Rutter, D.Rutter and G.Holland for their help in this project. This work was supported in part by: the Korea Research Foundation Grant funded by the Korean Government (MOEHRD) (KRF- 2006-214-C00022).